MAX-PLANCK-INSTITUT FÜR

FESTKÖRPERFORSCHUNG

STUTTGART – GRENOBLE

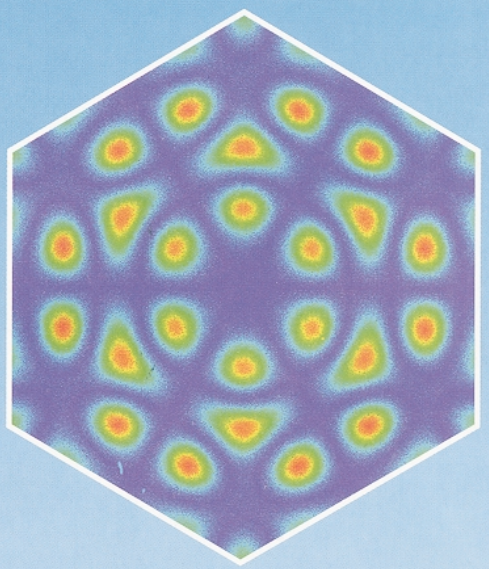

1997

Wissenschaftlicher Tätigkeitsbericht

Max–Planck–Institut für Festkörperforschung

Stuttgart – Grenoble

für den Zeitraum

1. Januar 1997 bis 31. Dezember 1997

Stuttgart: Max–Planck–Institut für Festkörperforschung
Heisenbergstrasse 1, D-70569 Stuttgart
Postfach: 80 06 65, D-70506 Stuttgart
Telefon: (0711) 6 89-0
Telefax: (0711) 6 89-10 10

Grenoble: C.N.R.S. – Max–Planck–Institut für Festkörperforschung
Avenue des Martyrs, B.P. 166
F-38042 Grenoble - Cedex 9 / France
Telefon: 33 / 476 85 56 00
Telefax: 33 / 476 85 56 10

Zum Sechseck im Titelbild

Spinfrustration ist vom triangularen Netz mit antiferromagnetischer Austauschwechselwirkung gut bekannt. Eine analoge strukturelle Frustration wurde für die hexagonal dichte Packung von Säulen mit oszillierendem Querschnitt gefunden, die in der Verbindung $Na_{22}Ba_{14}CaN_6$ auftreten. Diese Frustration führt zu diffuser Röntgenbeugung, deren berechnete Intensitätsverteilung $|M_{diff}|^2$ für die Schicht (hk2) gezeigt ist.

About the hexagon on the titlepage

Spinfrustration is well-known from a triangular net with antiferromagnetic exchange interaction. An analogous structural frustration was found for the hexagonal close packing of rods with oscillating diameter, which occur in the compound $Na_{22}Ba_{14}CaN_6$. This frustration leads to diffuse X-ray scattering whose calculated intensity distribution $|M_{diff}|^2$ is shown.

(U. Steinbrenner and A. Simon)

VORWORT

Dieser Bericht will Ihnen einen Einblick in die wissenschaftlichen Arbeiten des Instituts im Jahre 1997 vermitteln – vollständig kann er natürlich nicht sein. Die zahlreichen Publikationen lassen sich inhaltlich nicht auf wenige Seiten reduzieren. Die weißen Seiten sollen Ihnen dennoch einen Eindruck von den wissenschaftlichen Aktivitäten der einzelnen Abteilungen und Gruppen geben. Auf den ‘bunten Seiten’ finden Sie eine Liste der 1997 erschienenen Publikationen, allgemeine Informationen über das Institut, sowie ein Verzeichnis aller wissenschaftlichen Mitarbeiter am Institut.

Ende 1997 haben wir die beiden Kollegen Hans-Joachim Queisser und Hans Georg von Schnering in den Ruhestand verabschiedet. Lars Hedin, der kommissarisch die Abteilung Theorie II (ehemals Peter Fulde) leitet, wird das Institut im August 1998 verlassen. Die Emeritierung von Manuel Cardona steht bevor. Das Institut befindet sich in einer Phase des Umbruchs. Wir freuen uns, daß Martin Jansen das Angebot der Max–Planck–Gesellschaft angenommen hat und als Nachfolger von Hans Georg von Schnering seit Januar 1998 unserem Kollegium angehört. Hoffentlich gelingt es uns, noch in diesem Jahr weitere neue Kollegen im Institut begrüßen zu können.

Wir danken allen Mitarbeitern für die gezeigten Leistungen und die sehr gute Arbeit. Sie sind Grundlage für eine positive und wegweisende Gestaltung der Zukunft unseres Instituts.

Stuttgart – Grenoble DAS KOLLEGIUM

Im Februar 1998

CONTENTS

White Pages

Yellow Pages

Red Pages

Yellow Pages

Scientific work at the
Max–Planck–Institut für Festkörperforschung

Theoretical Physics

Electronic structure calculations are the main activity in the department headed by ANDERSEN. Density-functional calculations with the LMTO method are used as the first step towards a parameter-free description of physical and chemical properties of perfect and imperfect s-, p-, d-, and f-electron solids. The work is divided between methodical developments and applications. The methodical work in 1997 was focussed on the development of lattice quantum Monte Carlo methods for treating electron-electron and electron-phonon interactions, and the development of an automatic procedure for determining the parameters in model Hamiltonians directly from the LMTO Hamiltonian. Most applications in 1997 addressed alkali-doped C_{60} compounds and high-temperature superconductors. Using Monte Carlo methods, different factors (orbital degeneracy, lattice structure, number of electrons) determining the Mott metal-insulator transition were studied in the context of alkali-doped C_{60} compounds. The optical conductivity, the electron self-energy and the screening were calculated for A_3C_{60}. The implications of the screening on the superconductivity were studied. The new model Hamiltonian technique was used to obtain tight-binding parameters for a number of high-temperature superconductors. The lattice dynamics and electron-phonon interaction in $BaBiO_3$ were studied using a linear response LMTO method, and it was investigated whether the conventional mechanism for superconductivity applies to this compound.

The work in the group headed by PARRINELLO is focused on the numerical simulation from first principles of the properties of matter. The methods used allow the static and dynamical properties of solids, liquids and disordered systems to be determined accurately and without adjustable parameters. 1997 has seen several methodological developments. A new method for calculating infrared activity from the ab-initio molecular dynamics run has been applied successfully to a number of systems. A new code based on a Gaussian expansion of Kohn–Sham orbitals has been developed and tested. Also a new theory for the study of excited states has been proposed, opening the way for the study of photochemical processes. We have continued our traditional research on hydrogen bond systems, water and ice playing a prominent role together with solution chemistry. We have also simulated some of the crucial steps of the Ziegler–Natter heterogeneous catalytic processes, which is used in the industrial production of two of the most important plastics, polyethylene and polypropylene. Finally, research on large biological molecules has been continued, with the aim of understanding better the role of the environment on their chemical properties.

The THEORY II group (previously the Fulde group) is headed by HEDIN. Systems of current interest are high-T_c superconductors and compounds with orbital degrees of freedom like the manganites. The influence of electronic correlations and the electron-phonon interaction on superconductivity are important topics. The work often involves heavy numerical calculations. The correlation problem is attacked on many levels: Study of model Hamiltonians like the charge-transfer, Kondo-lattice, Hubbard, and the t-models, exact diagonalizations and l/N expansions, use of local correlation operators, expansions based on Baym–Kadanoff conserving approximations, and 'GW'-type approximations. One goal is to find connections between these approaches, and of course with experiment. The relations between the one-electron spectral function and experimental photo-emission spectra, which are influenced by loss processes, are investigated. In 1997 there has been important progress both on the manganite problem, and on high T_c superconductors. Manganites have both spin and orbital degrees of freedom, and therefore magnetic interactions are frustrated. This leads to new low-energy effective Hamiltonians, which depend on experimental parameters, and have been used to predict phase diagrams (Oleś and Feiner). Spin-correlations for the ferro-magnetic Kondo-lattice model have been studied employing the finite temperature diagonalization approach, and successfully correlated with neutron scattering measurements (Horsch *et al.*). In high-T_c superconductors the influence of strong correlations on the density response and the renormalization of phonons was studied (Horsch *et al.*). Effects of phonons on superconductivity also cannot be neglected. Predictions for the influence of different types of phonon couplings have been made (Fehrenbacher). Using local enforcements of constraints in the t-J model, a strong instability towards d-wave superconductivity was found (Zeyher).

Experimental Physics

CARDONA's group is mainly concerned with optical spectroscopy and scanning tunneling microscopy of semiconductors and high-T_c superconductors in the form of bulk samples, surface layers, and low-dimensional structures like quantum wells, quantum dots, and superlattices. Central to the interest of the group is electron-phonon interaction, a topic of particular relevance to both material classes. Experimental methods used at present are Raman, hyper-Raman, and Brillouin scattering off and in resonance, hot luminescence, spectroscopic ellipsometry (including synchrotron radiation as a source), optical measurements under high pressure and in high magnetic fields, photoelectron spectroscopy, scanning tunneling microscopy in ultrahigh vacuum, and X-ray techniques for surface and interface structure analysis. Close collaborations with the synchrotron laboratories in Hamburg (HASYLAB), Berlin (BESSY), Grenoble (ESRF), and Brookhaven (NSLS), the high-pressure, technology, molecular-beam epitaxy, and crystal-growth service groups at the MPI, the High-Magnetic-Field Laboratory and the Institut Laue-Langevin (ILL) in Grenoble have enabled the group to extend the variety of experimental techniques at its disposal. At HASYLAB, ESRF, and NSLS surface X-ray diffraction and X-ray standing wave measurements are carried out, while at BESSY a vacuum UV ellipsometer

(range 5–35 eV) is operated. At NSLS a Fourier ellipsometer for the far infrared spectral range has been built and optimized for measurements of extremely small samples. At ILL neutron scattering is used to study the lattice dynamics of isotopically pure and disordered single crystals. There is also a substantial theoretical effort in computing the electronic and vibronic band structure as well as electron-phonon coupling parameters of the materials under investigation. Topics of recent activities of the group are the vibrational and electronic properties of various compound semiconductors and superlattices, in many cases with controlled isotopic composition, the structure of semiconductor surfaces in the UHV and at the electrolyte interface, as well as electronic Raman scattering processes and crystal-field excitations in high-T_c superconductors. Considerable effort, partly in collaboration with the University of California at Berkeley and the Kurchatov Institute (Moscow), is spent in the growth and characterization of crystals with tailor-made stable isotope composition which are used to investigate isotope effects on a wide range of physical properties such as phonon dispersion, lattice constant, electronic band structure, or thermal conductivity.

Electronic properties of heterostructures, quantum wells, superlattices, and molecular systems, in particular the influence of quantum phenomena on the transport and optical response are the main topics of VON KLITZING's group. Optical and transport measurements in magnetic fields up to B = 20 Tesla and temperatures down to 20 mK are used to characterize the systems. The quantum Hall effect is studied by analyzing the electrical breakdown, the time-resolved transport, the edge channels and the behavior of composite fermions. Electron-phonon interactions in low-dimensional systems are investigated with ballistic phonon-techniques. Time-resolved photoconductivity and luminescence measurements in magnetic fields are methods of characterizing the electronic properties of optically excited carriers. A strong current interest is the preparation and investigation of coupled two-dimensional electronic systems and quantum dots. The cleanroom facility allows the realization of structures where a single electron dominates the optical and electronic behavior. The experiments are supported within the group by theoretical investigations of the transport and dynamic response of these low-dimensional electronic systems. In the research field of molecular electronics the properties of conductive polymers, fullerenes, nanotubes, Au-cluster, and switching molecules are investigated.

QUEISSER's group, specializing on extrinsic properties of semiconductors, is being systematically reduced, anticipating Queisser's retirement by the end of 1997. The appointments of J. Werner (Univ. Stuttgart) and W. Rühle (Univ. Marburg) to professorial chairs led to transfers of the research on photovoltaics and femtosecond spectroscopy. Work on defects and dopants in semiconductors continues; hydrogen and noble gases in silicon and compound semiconductors and 'silicon-backbone materials' are the main topics.

The Grenoble-HML-Außenstelle of our institute operates jointly with the French Centre National de la Recherche Scientifique (C.N.R.S.) the High Magnetic Field Laboratory in Grenoble. During the previous 20 years, there were two separate laboratories, the French and the German part, respectively; these have now been put together into one single laboratory, Frenchmen and Germans working together, with one director and one single technical and scientific policy. The aim of the laboratory is to provide high magnetic fields with a wide range of scientific instrumentation (temperatures 30 mK to 1000 K, pressures up to 24 GPa, voltages nV to 50 kV, currents pA to several kA, etc.) allowing many interesting investigations. In the years 1990/1991, most of the technical installations were renewed and the dc power supply was extended from 10 MW to 25 MW. We now have one of the world's most modern power- and cooling installation for the generation of high magnetic fields in operation. At the beginning of next year, a 20 MW resistive magnet will be in operation to produce fields in the 30 Tesla range. In addition, the MPG and the C.N.R.S. have decided to finance a new hybrid system for fields in the 40 Tesla range which will be working around the year 2000. All these magnets guarantee the leading role of the Grenoble-HML also in the years to come. In accordance with its mission the in-house-research at the HML shows a considerable diversification into several fields in condensed matter physics, where the use of high magnetic fields is interesting or necessary, such as the study of metals, semiconductors, 2D electronic systems, magneto-optics, polymers and all sorts of soft matter and even some biological systems.

Solid State Chemistry

MAIER's department is concerned with physical chemistry of the solid state, more specifically with chemical thermodynamics and transport properties (in particular ion conductors, but also semiconductors and high temperature superconductors). A major theme is the understanding of mass transport, chemical reactivities and catalytic activities in terms of defect chemistry, and thus optimization of corresponding parameters. Besides the clarification of local properties, also their superposition to the overall system property is investigated (inhomogeneous systems, especially multiphase systems and functional ceramics). In this context interfaces and microsystems are in the focus of interest. The research ranges from modelling, phenomenological theory to electrochemical and thermochemical experiments. Since electrochemical investigation immediately affects the coupling of chemical and electrical phenomena, the research is directed towards both basic materials problems (such as ion distribution at interfaces, transport in mixed conductors) as well as energy and information technology (fuel cells, chemical sensors).

The department of VON SCHNERING investigates cluster compounds with polyanions (elements of group 13, 14, 15) and polycations (transition elements), as well as metal complexes and special molecules. The synthesis of new compounds, crystal growth, structure determination, and determination of chemical and physical properties are central

activities and serve for a better understanding of structure and properties. The relationships of equilibrium conditions and kinetical processes are investigated by means of phase analysis, decomposition reactions and chemical reactions of solid state materials towards new molecular and polymeric cluster compounds. The determination of superstructures and disordered structures, investigations of valence electronic densities and dynamics of molecules in crystals as well as lattice energy considerations are important additional tools. Evaluation of Periodic Nodal Surfaces (PNS) for crystallographic symmetry groups is being done with respect to a generalization of the topological pattern of crystalline matter. Physical phenomena and chemical problems concerning valence electron distributions, ionic conductivity, diffusion effects and phase transitions are also investigated in this context. The experimental work is complemented by quantum mechanical calculations (e.g. Electron Localization Function, ELF). Related software is developed applying new computer architectures. The visualization of experimental and theoretical data by 3D computer graphics helps to correlate and to understand even complex phenomena.

SIMON's department emphasizes the investigation of metal-rich compounds (main group metals, d- and f-metals). The purpose of the work is on the one side the development of concepts of structure and bonding (e.g. systematization of condensed cluster concept) and on the other side the search for new materials (e.g. metal-rich compounds, transition metal clusters, reduced rare-earth halides, hydride, carbide, boride and boride-carbide halides of the rare-earth metals, alkali metal suboxides, alkaline earth subnitrides), phase relationships and relations between structure, chemical bonding and properties. Electron crystallography develops into a powerful tool in characterizing microcrystalline phases up to full structure refinement. Superconductivity is of special interest following a chemical view of the phenomenon in terms of a virtual (pairwise) localization of conduction electrons. Other fields of interest are structures of molecular crystals (in-situ grown crystals of gases and liquids). Experimental techniques like diffractometry with X-rays and neutrons, XPS, UPS, HRTEM, and measurements of magnetic susceptibility as well as electrical transport properties are used.

Service Groups

In contrast to other service groups the term CHEMIESERVICE (CS) (Kremer) refers to its main clients. The essential task of the CS is to support the experimental chemists of the institute with physical measurements. The emphasis hitherto lies on investigations of electrical and magnetic properties. Routine measurement of electrical conductivity, dielectric constant and magnetic susceptibility allows the selection of promising substances for more detailed investigations. This requires a high versatility of each of the experimental methods including, for example, the possibility of measurements on small samples under inert atmosphere. Several methods for a contactless determination of electrical properties have been developed recently. In the future we shall focus on methods better suited to

small samples using the know-how of other service groups (technology, high pressure, low temperature). In addition, when necessary, the CS brings new materials to the attention of the physics departments. The experimental facilities of the CS can, of course, also be used by physicists to supplement their investigations.

EDV's (Gliss) 1997 activities continued at about the 1996 level. Again, the number of workstations and servers has increased. Network operation was consolidated and an attempt was made to enhance our current service (based on 10 MBit/s ethernet and 100 MBit/s FDDI) by 100 MBit/s ethernet and switching technology for virtual LANs. The first switches supporting the new technology have been installed. A general backup solution for the MPI für Metallforschung and some groups at the MPI für Festkörperforschung using facilities at the DLR (Deutsche Forschungs- und Versuchsanstalt für Luft- und Raumfahrt) was introduced. The institutes use a 10 MBit/s fiber-optic link to the DLR's computing center and the IBM ADSM system there. All goals as to cost effectiveness and robustness have been met. The bandwidth of the link has been proven sufficient. At least one incident of a server loosing its data and recovering them through the system has established credibility for our solution. Both institutes have agreed to continue computing activities in a changed organizational from the beginning of 1998 making this the last report covering activities concerning both institutes.

The EPITAXY GROUP studies kinetics of semiconductor crystal growth by liquid phase epitaxy (LPE). The influence of crystallization mechanisms on morphology, defects, and dopant distribution is investigated with layers of GaAs, Si, and Ge as well as $\mathrm{Si_xGe_{1-x}}$ on Si. Centrifugal forces are utilized for growth from solutions. This research led to extremely high-purity GaAs layers and very thin multilayers of GaAs and Si, and other systems. Selective epitaxy on partially masked substrates and seeded lateral overgrowth yields defect-free silicon-on-insulator layers. Crystalline layer growth is performed on ceramics, glassy carbon, or glass from metallic solutions below 500°C. Epitaxial layer growth of very pure isotope semiconductors, for example $^{28}\mathrm{Si},\ ^{29}\mathrm{Si},\ ^{30}\mathrm{Si},$ is a recent interesting research topic. LPE processes, layer growth takes place close to thermodynamically equilibrium, the epitaxial layers have a high structural perfection, hence superior electronic quality. The layers are usable for basic research and for applications, e.g. transistors, detectors, and solar cells.

The CRYSTAL GROWTH GROUP (Schönherr) applies and modifies techniques for growth of bulk crystals from the melt, vapor and solution. Examples of materials are Si, AlSb, Bi, II-VI-compounds, Ag- and Cu-halides, superconducting oxides. Particular techniques have been modified for the growth of crystals with isotopic components. The growth kinetics and habit development are quantified by in-situ observation for crystals grown from the vapor. Superconducting oxide ceramics are synthesized by solid state reactions which are thermo-gravimetrically monitored. For optimizing crystal growth from the vapor phase, vapor pressure and binary gaseous diffusion coefficients are experimentally determined.

The X-RAY DIFFRACTION GROUP (Peters) is in charge of taking care of X-ray sources and diffraction cameras belonging to the 'Röntgenpool'. Nondestructive investigations on single crystals and on powder samples can be performed with film exposing methods. For extended X-ray diffraction measurements of single crystals, four-circle diffractometers are available. For the evaluation the SIEMENS SHELXTLPLUS system for solving, refining and displaying crystal structures from diffraction data is employed.

Research within the HIGH PRESSURE GROUP (Syassen) is concerned with the effects of hydrostatic pressure on structural, lattice dynamical, and electronic properties of crystalline solids and their high pressure phases. The primary experimental methods are synchrotron X-ray diffraction and low-temperature optical spectroscopies. Materials currently under investigation are semiconductors and their heterostructures, transition metal compounds including superconducting cuprates, inorganic molecular and low-dimensional solids, and intermetallic rare earth compounds. Laboratory facilities for optical spectroscopy and X-ray diffraction under pressure are available for use by other scientific groups (in-house and external). Pressure experiments in other research groups are supported through design and maintenance of pressure equipment.

The Service Group OPTICS AND SPECTROSCOPY (Kuhl) develops new optical instruments and components and measures optical properties of solid, liquid and gaseous samples. Available are grating and Fourier spectrometers for absorption and reflectivity studies within the spectral range from 180 nm to 1 mm wavelength. Investigations of optical properties of high-T_c superconducting materials have been emphasized. The construction and operation of optical instruments in other groups is supported by technical advice. The research concentrates on generation of pico- and femtosecond optical pulses, as well as on studies of ultrafast relaxation of nonequilibrium carriers, excitons and phonons in semiconductors. Short optical pulses are used to generate and analyze pico- and subpicosecond electrical pulses by means of photoconductive switching and electro-optic sampling. These techniques are applied for characterization of high speed electronic and optoelectronic devices and coherent THz-spectroscopy on high-T_c superconductors.

Main subject in the MBE GROUP (Eberl) is the preparation and characterization of III/V and group IV semiconductor heterostructures. We apply molecular beam epitaxy (MBE) for the material systems AlGaAs/GaAs, InGaAs and InGaP on GaAs substrate, and SiGe/Si on Si substrate. Our main interest is the preparation of low-dimensional structures. Lateral confinement is achieved by MBE-growth on patterned substrates, and by island formation in epitaxial growth of stained heterostructures. We are also investigating an atomically defined in-situ etching technique based on $AsBr_3$ within the MBE system. The group IV element MBE activities are concentrated on the preparation of $Si_{1-y}C_y$ and $Si_{1-x-y}Ge_xC_y$ alloy layers for new Si based devices.

The TECHNOLOGY GROUP (Habermeier) offers service work in the fields of thin film deposition technology, microlithography and fabrication of contacts to semiconductors and ceramic materials. The experimental facilities for the thin film work include the conventional high vacuum evaporation and sputtering (dc, rf and reactive) techniques. Additionally, pulsed laser deposition facilities are installed to prepare thin films with complex chemical composition such as high temperature superconductors, perovskites with colossal magnetoresistance and ferroelectric materials. In the area of microlithography simple masks with design rules down to 5 μm can be realized in one photoreduction step. Recently, a Laser Mask Macro Projector has been installed which offers the possibility for improved mask making and direct, chemistry-free thin film patterning. The etching techniques available include wet chemical etching, ion milling and plasma etching as well. The research activities of the group are closely related to the service tasks. Thin film deposition of high temperature superconductors by pulsed laser deposition and rf sputtering play a central role. Interface and surface related properties such as defect structure, electrical transport and flux pinning of $YBa_2Cu_3O_7$ have been studied in some detail. Single crystal type films of materials with 'colossal' magneto-resistance (La-Ca-Mn-O and La-Sr-Mn-O) are prepared and investigated especially with respect to the interrelation of microstructure and transport properties. Recently a giant sensitivity of resistance with external hydrostatic pressure has been explored.

The LOW TEMPERATURE GROUP (Gmelin) comprises research laboratory (TTL) and a technical service-group (TTS), the latter belonging to the Max–Planck–Institut für Metallforschung. The research activities in TTL focus on the investigation of thermal properties of solids, the study of microscopic (nm-scale sub μsec) temperature profile measurements (thermography) and on the transport in semiconducting micro-contacts. Specific heat, thermal conductivity and thermal expansion are measured between 0.3 K and 320 K and partially within applied magnetic fields up to 16 T; specific heat can be investigated also up to 1700 K. Small samples (mg-range) are measured with a new type of high precision adiabatic-differential-scanning calorimeter. In 1997, with preference magnetic and electronic phase transitions have been studied by specific heat experiments: Intermetallic compounds of the type REAuGe (RE = rare earth), and REAgGe, quasicrystals of the type Al-Pd-Mn, $P_{1-x}Y_xBa_2Cu_3O_{7-\delta}$ single crystals, pyrochlores $REMo_2O_7$, $Mn_{2-x}Cr_xSb$ compounds, BiOHal (Hal = Cl, Br, J) and $NdSrMnO_{3-y}$ compounds. Studies and development of highly sensitive semiconductor tips for high-resolution thermal scanning continued. In TTS the service is currently offered for technical gases, vacuum pumps, l iquid nitrogen and liquid helium supply, and for any type of cryogenic construction, design, documentation and consulting. About 240,000 litres of liquid helium were liquefied and distributed in 1997.

A selection of research results from 1997

Physics of nanostructures and defects

Fullerenes, fullerides and nanotubes

Superconductivity

New methods and models

New structures and compounds

Transport

Carbon-induced Ge quantum dots in Si

Recently semiconductor quantum dots have found considerable interest due to their atom-like discrete energy spectrum. Arrays of quantum dots promise improved performance for semiconductor lasers and single electron devices (K. Eberl, Physics World **10**, 47 (1997)). Si is an indirect semiconductor and thus shows only extremely weak light emission. Charge carrier localization in 10 nm size quantum dots in Si may offer a possibility to obtain more intensive light from Si-based structures. This contribution describes latest results on a new concept for making self-assembling quantum dots in Si which show intensive photoluminescence in the wavelength range of $\lambda = 1.3$ μm.

The lattice constant of Ge is 4% larger than that of Si. Therefore, Ge forms islands during deposition on (100)-oriented Si due to Stranski–Krastanov growth mode. The Ge-islands are typically larger than 50 nm and assemble themselves on a 3 to 4 monolayer thick wetting layer. The photoluminescence (PL) which is observed from the large Ge-dots is weak in intensity because the band offset in pseudomorphic Si/SiGe heterostructures is mainly in the valence band. In other words, there is significant hole confinement within the Ge-dots, but the electrons are not localized in the dots because of the type II band alignment.

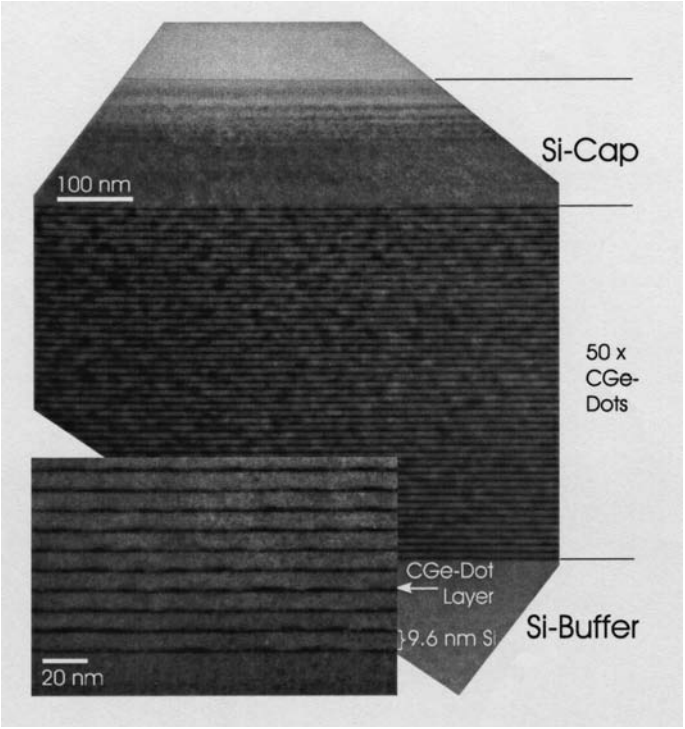

Figure 1: *Cross-sectional TEM-image of a stack of 50 layers of carbon-induced Ge-dots. The inset shows very small, well-developed but vertically uncorrelated islands.*

A small amount of only about 0.2 monolayers C followed by 2.4 monolayers Ge results in the formation of very small Ge quantum dots which are 10–15 nm in diameter and

1–2 nm in height. Unlike to an identical structure without the pre-growth of C, a variety of advantageous aspects such as strain compensation, strongly enhanced no-phonon PL at a wavelength of around 1.3 μm and the possibility of effective waveguiding make this C-induced Ge-dots attractive for optoelectronic devices.

Two samples, a 50 layer-stack of CGe-dots and a 50 period Si/Ge superlattice without C, are grown on Si using solid source molecular beam epitaxy. Figure 1 shows a cross-sectional TEM image of 50 layers of C-induced Ge-dots. No dislocations can be found within the whole investigated sample area. The on average darker color of the dot-layer stack compared to the Si buffer and cap layers visualizes, what might be advantageous for future optoelectronic applications: The stacked CGe-dot layers are expected to exhibit a larger refractive index than Si because of the smaller average bandgap. The CGe-dot stack could therefore be used as a light generating as well as light guiding structure.

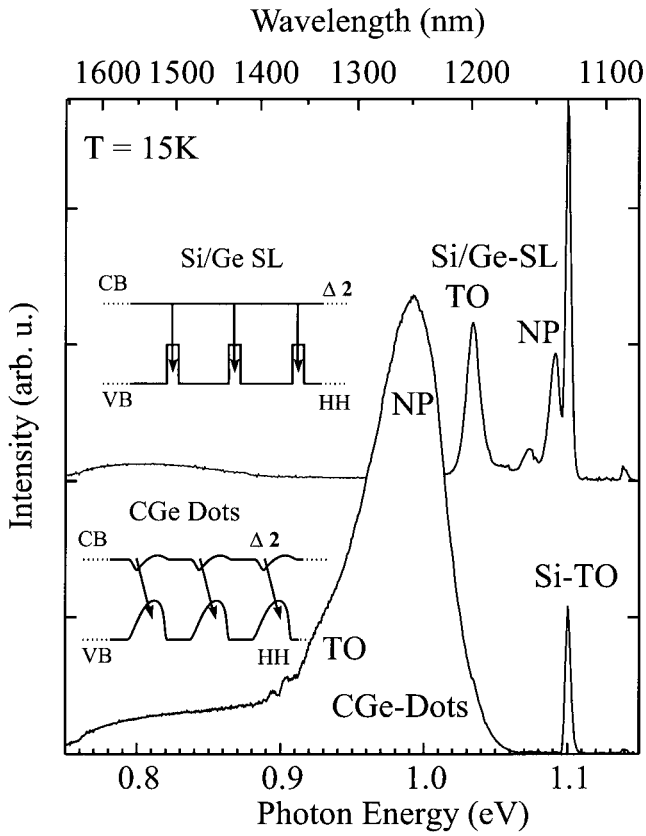

Figure 2: *Comparison of photoluminescence spectra of a 50 period 9.6nm Si/2.4 ML Ge superlattice (SL) with a 50 period 0.2 ML C/2.4 ML Ge-dot superlattice. Due to 3D confinement the optical transition of the CGe-islands is red-shifted by 100meV. Efficient spatially indirect recombination channels result in strongly enhanced no-phonon PL-signal for the CGe-dots. The insets show the band edge alignment of the two different structures. For the Si/Ge SL the main band-offset is given in the valence band (VB), whereas for the CGe-dots a larger conduction band (CB) offset and spatially indirect recombination is assumed.*

The inset of Fig. 1 presents a five times enlarged image of the C-induced Ge-dot layers. Well-developed islands are formed. Surprisingly, there is practically no vertical alignment of the dots in contrast to what has been observed for conventionally grown Ge-islands where strain fields in neighboring layers induce Ge-dots at identical lateral positions. We assign this effect to the pre-growth of carbon. The carbon atoms introduce a rough surface including strong local strain fields. The diffusion length of the arriving Ge atoms is drastically reduced and vertical alignment of the Ge atoms on top of the underlying islands is suppressed.

In Fig. 2, PL-spectra at T = 15 K of two samples are presented. Besides the Si-TO line, PL-peaks corresponding to the Si/Ge superlattice and the C-induced Ge-dot superlattice are observed at 1.090 eV (no-phonon) and 0.990 eV, respectively. Due to Ge-island formation the optical transition of the CGe-dots is red-shifted by 100 meV to a wavelength of 1252 nm, which almost coincides with 1.3 μm wavelength, which is used for long-range optical fiber communication. However, compared to previous PL-spectra of a single layer of CGe-dots (O.G. Schmidt et al., Appl. Phys. Lett. **71**, 2340 (1997)) the transition energy is shifted by 30 meV to the low energy side. We attribute this red-shift to electronic coupling of carriers localized in neighboring dot layers. Whereas for the Si/Ge superlattice the no-phonon (NP) and TO-phonon lines are well resolved and comparable in intensity, a much broader PL-peak with a strongly enhanced NP-peak is observed for the CGe-dots. The broadness is attributed to the inhomogeneous dot size distribution. But more important, the integrated intensity of the CGe-islands is by a factor of 15 larger than that of the Si/Ge superlattice and is explained by efficient, spatially indirect recombination of electrons confined in an underlying C-rich SiGeC wetting layer with heavy holes confined in the Ge rich upper part of the island, which has been discussed in detail elsewhere (O.G. Schmidt et al., Appl. Phys. Lett. **71**, 2340 (1997)).

In conclusion, we have presented a stack of 50 layers of carbon-induced Ge-dots. This structure exhibits very small, well-developed but vertically uncorrelated islands. Due to the pre-grown carbon, net compressive strain within the whole structure is kept much smaller than for a reference Si/Ge superlattice without C. Together with strongly enhanced photoluminescence signal this structure offers a large potential for future optoelectronic devices. There is significant design flexibility for further light output optimization by changing the Si spacer thickness, the C pre-deposition, the Ge thickness and the total number of stacked layers.

(K. Eberl, O.G. Schmidt and S. Schieker; J.Y. Jin-Phillipp and F. Phillipp
(MPI für Metallforschung))

Single-electron transistor probes two-dimensional electron system

In the last several years theoretical and experimental investigations have emphasized the important role of the edge of a two-dimensional electron system (2DES) in understanding the quantum Hall effect: Strips of metal-like and insulator-like behavior, so-called compressible and incompressible strips, are expected to develop with magnetic field within the depletion region at the edge of the 2DES. Theoretical works (see for instance K. Lier and R.R. Gerhardts, Phys. Rev. **B50**, 7757 (1994)) describe these strips at the edge as a consequence of quantizing the electronic levels of the 2DES by the magnetic field into Landau and spin levels. Increasing the electron concentration from the edge to the bulk, which happens over a typical distance of 1 μm, requires locally filling up more and more levels, but whenever a level is filled, due to the energy quantization it is energetically favourable to keep the electron concentration constant for a certain width. An incompressible strip is formed. The widths and the positions of these strips depend on the imprinted potential profile at the edge and on the quantization energy, i.e. the magnetic field. In the experiments here, a single-electron transistor (SET), made of metal, is used as a local electrometer to investigate the bulk and the predicted edge strips of the 2DES.

Figure 3 a shows a sketch of the SET which is deposited on top of the $Al_{0.33}Ga_{0.67}As$-GaAs heterostructure with the 2DES, 86 nm below the surface. The SET consists of a small aluminum island – 0.1 μm in width and 1 μm in length – which is coupled by aluminum oxide tunneling barriers to the aluminum source and drain electrodes. Due to the small size of the electronic island and small area of the tunnel junctions (about 0.1 μm by 0.1 μm), the total capacitance C of the island is small. Adding an electron to the island requires the Coulomb charging energy $e^2/2C$ (about 0.1 meV here), which acts like an energy barrier and blocks electrical transport through the island at the temperature $T < 100$ mK used in our experiments. Alloyed ohmic contacts to the 2DES allow to use the 2DES as a gate electrode for the SET island. With changing V_{2DES}, the electrostatic potential of the island is shifted and the energy for adding an electron is lowered. The island is charged by another additional electron whenever the voltage is increased by $\Delta V_{2DES} = e/C_{2DES}$ where C_{2DES} is the 2DES-island capacitance. As shown in Fig. 3 b, a sequence of conductance peaks is observed with the period ΔV_{2DES} – the so-called Coulomb blockade oscillations (CBO).

Applying a magnetic field B perpendicular to the 2DES, the Coulomb blockade oscillations shift on the axis of the externally applied voltage V_{2DES}, as shown in Fig. 3 c. These shifts reflect the variation of the chemical potential of the 2DES at constant electron concentration with changing magnetic field (Y.Y. Wei, J. Weis, K. v. Klitzing and K. Eberl, Appl. Phys. Lett. **71**, 2514 (1997)). This becomes clear when taking into account the intrinsic contact voltage $V_{contact}$ in series with the external applied voltage V_{2DES} which contributes to the electrostatic potential difference between the 2DES and SET island. This contact voltage is given by the difference in the chemical potentials (workfunctions) of the aluminum and the 2DES in the heterostructure. The magnetic field affects the electronic structure of the 2DES whereas in comparison the effect on the aluminum is negligible. Therefore, changes in the contact voltage follow mainly the variations of the

chemical potential of the 2DES. In the low magnetic field regime, the depopulation of Landau levels with increasing magnetic field is nicely observed. This is different at high magnetic fields in the regime of well developed quantum Hall plateaus where the Fermi level is located in the mobility gap, i.e. between two Landau levels: The 2DES no longer works as a gate electrode for the SET. The 2DES below the SET island is electrically decoupled from the edge where the voltage V_{2DES} is applied. Instead relaxation processes and charge fluctuations versus time become visible (in Fig. 3 c around B = 3 T).

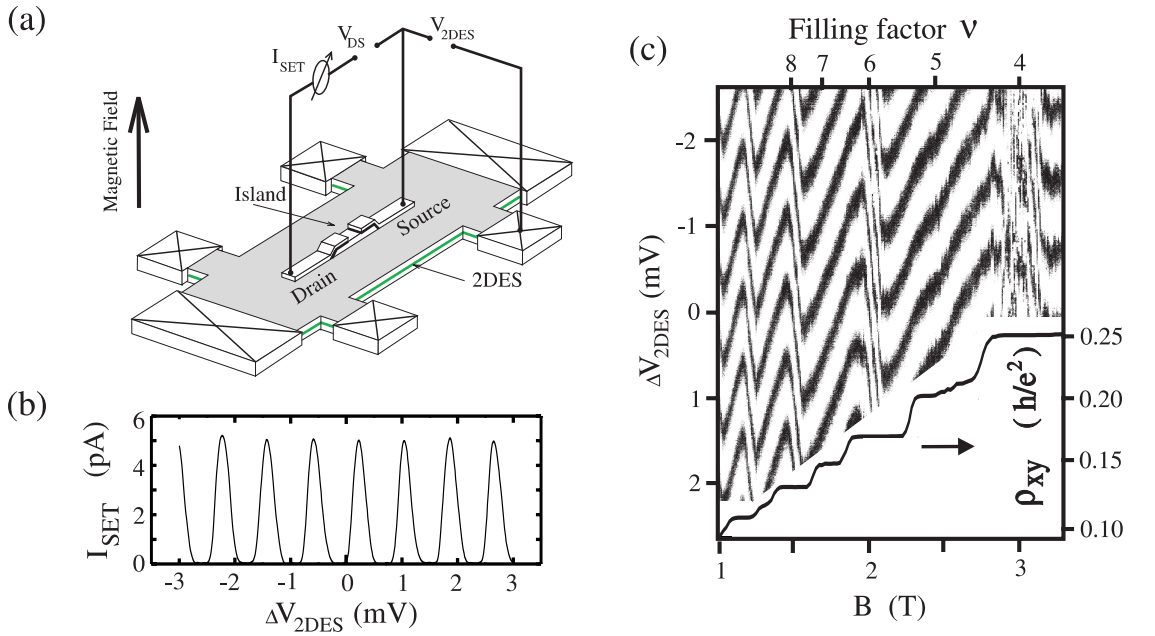

Figure 3: *(a) A single-electron transistor consisting of a metal island, which is coupled to drain and source electrodes via tunneling barriers, is deposited on top of a Hall bar which has been etched into a GaAs/AlGaAs heterostructure containing a two-dimensional electron system (electron concentration n_s=2.9× 10^{11} cm^{-2}, electron mobility μ_e=4× 10^5 cm^2/Vs at T=4K). Alloyed ohmic contacts give electrical connection to the 2DES. (b) The Coulomb blockade oscillations measured at T=100mK by using the 2DES as the gate electrode for the SET island (V_{DS}=80μV). (c) The Coulomb blockade oscillations shown in greyscale as a function of magnetic field. The shifts reflect the variations of the chemical potential of the 2DES. For comparison, the quantum Hall curve is shown in the inset.*

The 2DES in the bulk has lost its good conductivity and the screening properties of a metallic layer. This interpretation is verified by changing the voltage applied to the metal electrode on the backside of the heterostructure. Coulomb blockade oscillations as a function of *backgate voltage* are not observable whenever the 2DES, which lies between the backgate and the SET, shows metal-like behavior in the bulk. But Coulomb blockade oscillations as a function of the backgate voltage become visible within the quantum Hall regime which demonstrates that under this condition the 2DES behaves like an insulator and can not screen the voltage variations of the backgate for the SET island.

By electrostatically depleting the 2DES below a metal gate electrode as shown in Fig. 4 a, the edge of the 2DES is redefined at a distance of about 0.9 μm from the SET island. Instead of measuring the CBO, a feedback circuit is used which keeps the SET current constant by controlling V_{2DES}. The fluctuations of the feedback signal are plotted in Fig. 4 b. In the quantum Hall regime (for instance around B = 9 T and zero sidegate voltage), the SET is decoupled from the edge, i.e. the 2DES does not work as an effective gate electrode and therefore the feedback signal fluctuates due to charge fluctuations in the 2DES below the SET island. With a more negative depletion voltage, the edge is shifted further towards the SET island. The feedback signal becomes stable (for instance for $V_{sidegate} < -1$ V at B = 9 T), since the metal-like region at the boundary of the 2DES has been moved below the SET by the sidegate voltage.

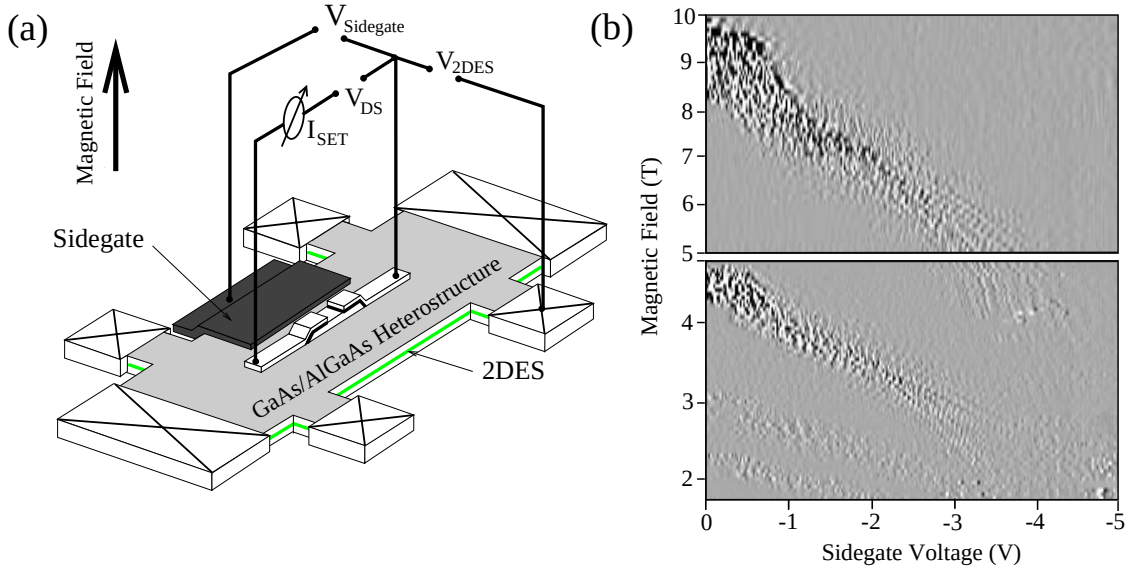

Figure 4: *(a) The second experimental setup: A sidegate electrode is deposited close to the SET island. It is used to redefine an edge of the 2DES close to the SET island (2DES electron concentration n_s=2.1$\times 10^{11}$ cm^{-2}, electron mobility μ_e=1.3$\times 10^6$ cm^2/Vs). (b) Greyscale plot of the 'fluctuations' observed in the SET current as a function of sidegate voltage and of magnetic field. With more negative sidegate voltage, the edge is shifted closer to the SET.*

In conclusion, fluctuations in the feedback signal in Fig. 4 b can be identified as incompressible (insulating) regions at the position of the SET. At low magnetic fields, several strips of different screening properties become visible as expected from the compressible–incompressible strip model. Since the sidegate voltage moves the electrically defined edge, the $V_{sidegate}$ axis in Fig. 4 b can be directly used as a measure of the distance of the SET from the edge. Simple model calculations show that the relation is almost linear. The 2DES is depleted below the gate at $V_{sidegate} = -0.25$ V, i.e. the edge is at the boundary of the sidegate and reachs the SET at about $V_{sidegate} = -4.5$ V. To confirm that we have strips which are – at least on a length scale of several tens of microns – isolated from each other by an incompressible strip, the electrochemical potentials of the different metal-like

strips are separately modulated and the capacitive coupling to the SET island is detected as a function of the edge position. By this technique, the strips are resolved individually and even the chirality of the strips is demonstrated (not shown).

In summary, the chemical potential of the 2DES is directly measured by a SET. Charge fluctuations become visible in the quantum Hall regime where the bulk of the 2DES is decoupled from the edge of the 2DES. By using a sidegate at a distance of about 0.9 μm distance from the SET island, fingerprints of strips with different screening properties are clearly detected.

(J. Weis, Y.Y. Wei, K. v. Klitzing and K. Eberl)

Transition between integer and fractional quantum-Hall-effect induced by a lateral superlattice

For a homogeneous two-dimensional electron system in a strong perpendicular magnetic field, the Quantum-Hall-Effect (QHE) appears in two different shapes. The *integer QHE* (IQHE) reflects quantization of the *single particle kinetic energy* into discrete Landau levels. It manifests itself in a Hall conductivity which, close to complete filling of the topmost Landau level, is an integer multiple of the conductance quantum e^2/h.[1] The *fractional QHE* (FQHE) occurs in systems clean enough for *electron correlations* to be effective. Near fractional filling $\nu := 2\pi\ell^2 n = p/q$ with odd denominator q, the Hall conductivity, plotted versus magnetic field, shows a plateau at the fractional quantized value $\sigma_H = (p/q)(e^2/h)$.

Non-interacting electrons in a lateral, *bidirectional superlattice*, in contrast, are expected to show the IQHE whenever the Fermi energy lies in a gap between adjacent Landau level subbands (Hofstadter spectrum). These subbands form as a consequence of commensurability effects between the lattice unit cell area and the magnetic unit cell, i.e. the area comprising a single flux quantum. Thus, the IQHE occurs in these inhomogeneous system at prominent *fractional fillings*.

Specifically, non-interacting electrons in a commensurate bidirectional superlattice $V = \tilde{V}_0(\cos(2\pi x/a) + \cos(2\pi y/a))$, such that three flux quanta penetrate the lattice unit cell area $A = a^2$, show the IQHE with $\sigma_H = 0(e^2/h)$ at complete filling of the lowest of three Hofstadter subbands, i.e. at the fractional filling $\nu = 1/3$. On the other hand, at filling factor $\nu = 1/3$ (i.e. three flux quanta per electron) *interacting electrons in a homogeneous system* form an incompressible liquid, the ground state of which is separated from the excitation spectrum by the correlation gap Δ. This state shows the FQHE at $\sigma_H = (1/3)(e^2/h)$.

---

[1] A non-spin degenerate Landau level can host one electron per flux quantum, comprising a sheet density n of $(2\pi\ell^2)^{-1}$, where the magnetic length ℓ is given by $\ell^2 = (\hbar c)/(eB)$.

Our investigations are based on the following setup. Imagine a QH system at fixed filling factor $\nu = 1/3$ subjected to a superlattice potential with tunable amplitude. The above considerations imply different limiting behavior for small ($V_0 \to 0$) and large ($\Delta \ll \tilde{V}_0 \ll \hbar\omega_c$) potential amplitude.[2] Although both limiting states are described by an incompressible liquid, a FQH state forms in the small V_0 limit, while at large modulation potential the single particle potential energy dominates the electron correlations, resulting in an IQH state.

This development is demonstrated in Fig. 5 where the energy spectrum of four electrons is shown as a function of $V_0 = \tilde{V}\exp(-\pi/6)$. The right part of Fig. 5 shows the normalized spectrum at larger potential amplitude and, for comparison, the spectrum of four non-interacting electrons. It is obvious that for a strong potential the interacting and non-interacting spectra are very similar, indicating a transition to a quasi–non-interacting electron system. The question to be answered, however, is whether the transition from the strongly interacting FQH system to the weakly interacting IQH state occurs as smoothly as suggested by Fig. 5.

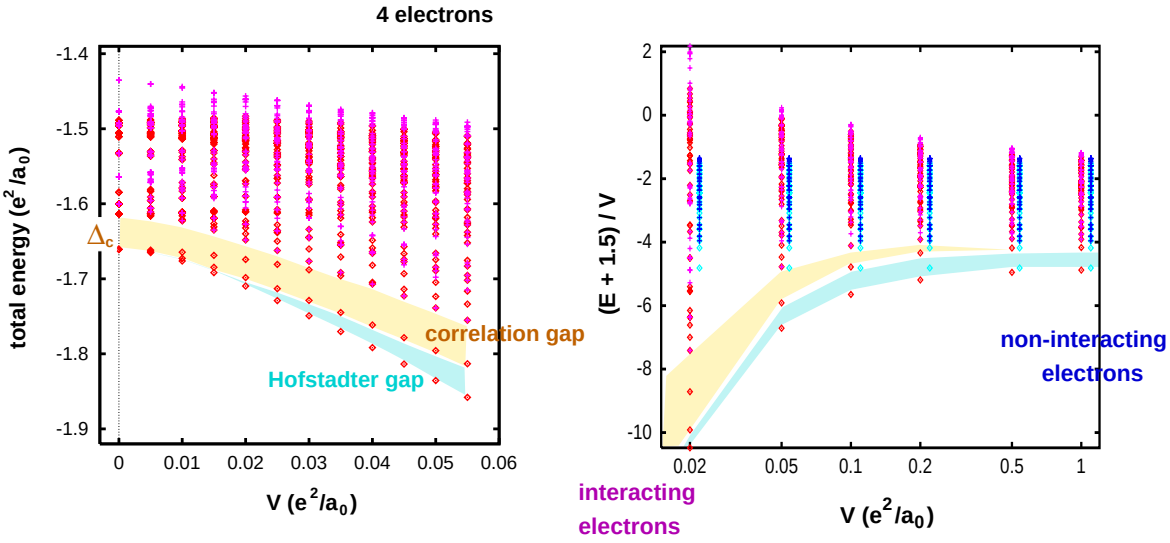

Figure 5: *Low energy part of the four-electron spectrum versus modulation amplitude V. At small system sizes, the Hofstadter gap opens at very small modulation strengths and coexists with the correlation gap at a finite range of amplitudes.*
To the right: Comparison of interacting (left columns) and non-interacting (right) electrons. (Spectra are offset and normalized by the modulation amplitude.)

Recalling that the Hall conductivity is inseparably connected to a topological invariant of the systems ground state, i.e. the winding number with respect to wave vector transport around the Brillouin zone (the so-called Chern number), it becomes obvious that the fractional to integer transition requires an essential change in the systems ground state. It is anticipated that this transition takes place in form of a quantum-phase transition which

[2] The amplitude has to be small compared to the Landau level separation $\hbar\omega_c$ to avoid Landau level mixing.

can be monitored by the gap separating the ground state from the excited states. At the critical point the gap closes from both sides ($V \searrow V_c$, $V \nearrow V_c$), giving rise to a transition between incompressible states via an intermediate compressible state. At finite temperatures the transition region is finite. Thus, this transition should exhibit a behavior similar to the well-known transitions between adjacent IQH plateaus in a homogeneous system, although one has to keep in mind that for the latter the critical parameter is the filling fraction, which is kept constant here.

To support this hypothesis we performed finite size calculations where we diagonalized the few-particle Hamiltonian, subject to quasi-periodic boundary conditions on the wave functions. The number N_e of electrons coincides with the number $N_x \times N_y$ of lattice cells contained in the supercell area. Performing a finite size analysis for system sizes up to eight electrons and unit cells, we were able to estimate the critical potential amplitude $V_c = 1.2\Delta$ from the fixed point of the appropriate scaling ansatz (see Fig. 6),

$$LW = Q_r\left(L^{\theta}\frac{v - v_c}{V_c}\right) , \qquad (1)$$

where the subscript $r = L_x/L_y$ indicates the aspect ratio dependence of the finite size data. We choose the effective dimensionless size of the two-dimensional system to $L = 2\,N_x Ny\,/\,(N_x + N_y)$. The renormalized potential amplitude $v = \tilde{V}/\Delta(N_x, N_y)$ accounts for the size dependence of the correlation gap in the very small systems accessible by direct diagonalization and θ labels the inverse critical correlation length exponent. As suggested by the similarity to IQH transitions and as predicted by a field theoretical treatment, a critical dynamical exponent $z = 1$ was assumed in the above scaling ansatz, Eq. (1).

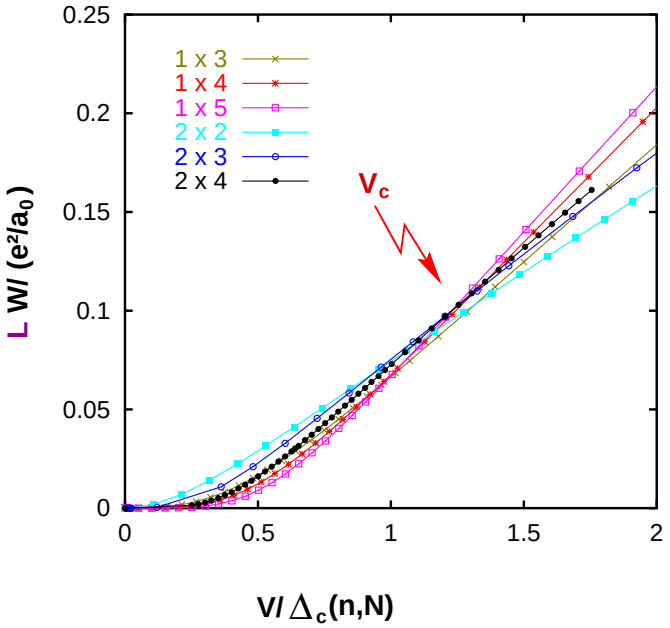

Figure 6: *Gap between the ground state and first excited state W scaled by the system size L versus reduced modulation amplitude. The approximate crossing of the curves indicates the critical reduced modulation amplitude. (System sizes in units of the lattice constant, z=1.)*

Fitting the aspect ratio dependence to the functional form $Q_r = ((1/r + r)/2)^{\kappa}Q$, our data show astonishingly good scaling behavior, assuming $\theta = 0.43$, the same value which was observed for transitions between IQH plateaus (see Fig. 7).

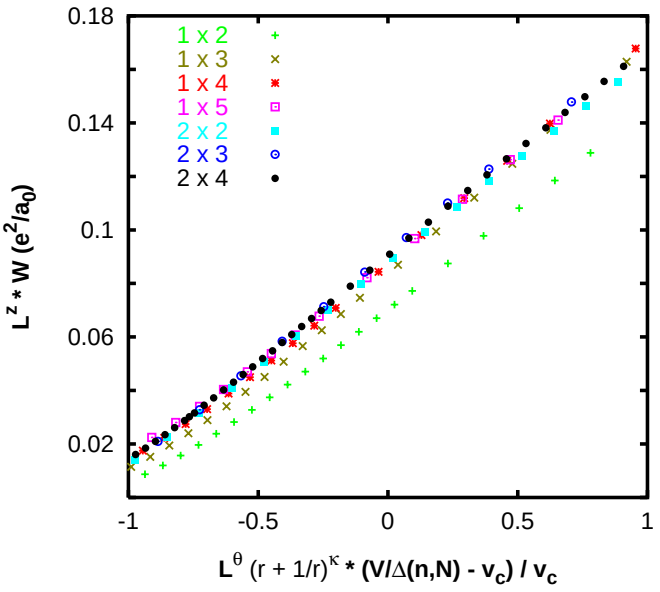

Figure 7: *Scaling behavior of the energy gap W near the critical point. An inverse critical exponent θ=0.43 was estimated from the data.*

We, nevertheless, want to emphasize that the size variation accessible to our calculations are much to small to reliably estimate the critical exponents. However, its agreement with field theoretical predictions give confidence in the critical field value $V_c = 1.2\,\Delta$ predicted here, and in the hope that the essential physics of the phase transition is already captured in the behavior of our small systems.

(D. Pfannkuche; A.H. MacDonald (Indiana University at Bloomington, USA))

Spin-flip Raman scattering in II-VI semiconductor nanostructures

Electron and hole g factors, which describe the splitting of electronic states in a magnetic field, are among the fundamental properties of semiconductors. The effective electron g factor in solids usually differs strongly from the vacuum value. It depends on the spin-orbit coupling and is directly related to band parameters.

In nanostructures like quantum wells (QW) and quantum dots (QD) the g factors of electrons and holes often deviate from those of bulk semiconductors. Several reasons can be adduced to explain these differences: (i) The band parameters are changed by the confinement, especially the energy gap. (ii) The symmetry is reduced, a fact which results in an anisotropy of the *electron* g factor. (iii) Strain due to the lattice mismatch in heterostructures leads to further shifts of the electronic states which change the g factor. In low-dimensional systems combinations of these effects, which depend distinctly on structural parameters like, e.g. the QW width L_W, or the QD radius R, cause a rather complicated behavior of the g factors. On the other hand, variations of the g factors with

these parameters can be exploited to gain insight on their properties on a microscopic level. For this purpose we studied g factors of II-VI semiconductor nanostructures, such as $CdTe/Cd_{1-x}Mg_xTe$ QW and CdS QD using resonant spin-flip Raman scattering (SFRS), which is one of the most reliable experimental techniques for a direct measurement of g factors. In comparison to other methods, e.g. optically-detected magnetic resonance (ODMR), Hanle-effect measurements under optical orientation of electron spins, quantum-beat spectroscopy, and polarized-exciton luminescence, which only yield the g factors of either excitons, electrons, or holes, SFRS in many cases allows one to determine all these quantities in a single experiment.

Typical SFRS spectra for $CdTe/Cd_{1-x}Mg_xTe$ QW and CdS QD are shown in Fig. 8 for excitation in resonance with the exciton ground state. The spin-flip Raman shifts of the exciton (EX) and electron (E) lines are directly proportional to the magnetic field B, giving absolute values of the respective g-tensor components along the field direction. The energy splitting between these two lines, E and EX in Fig. 8 a, gives the absolute value of the hole g factor. The sign of the g factors can be usually determined from the selection rules of experiments under circular polarization.

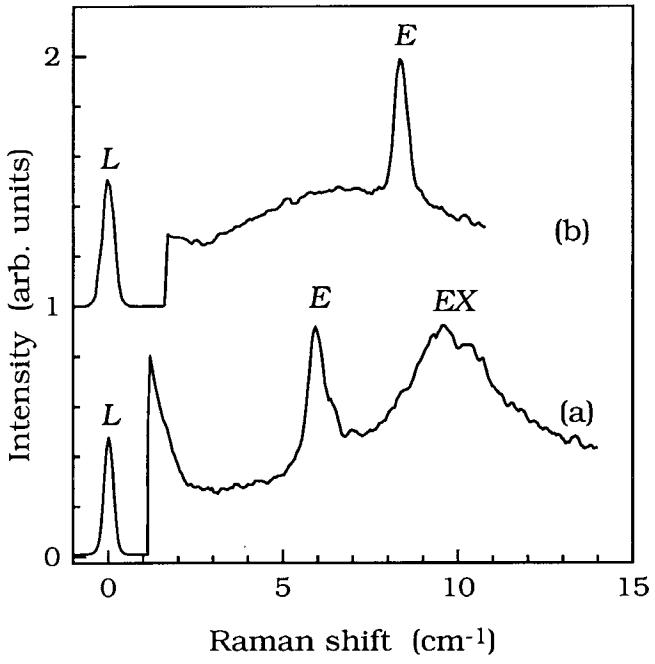

Figure 8: *SFRS spectra of (a) 45 Å $CdTe/Cd_{0.85}Mg_{0.15}Te$ QW and (b) CdS QD with a mean radius of nanocrystals $\bar{R}$=70 Å measured at B=10T. The exciton and electron spin-flip lines, and the laser line (attenuated by a neutral-density filter) are marked with EX, E, and L, respectively.*

Experimental values for electron g factors g^e, vs. the exciton ground state energy E_{ex}, are shown in Fig. 9 a for $CdTe/Cd_{1-x}Mg_xTe$ QW with different L_W and Mg content in the barriers x, and in Fig. 9 b for CdS QD with different mean radii of the nanocrystals $\bar{R}$. With increasing confinement (larger E_{ex}), the g^e values in $CdTe/Cd_{1-x}Mg_xTe$ QW become larger than g^e in bulk CdTe ($g^e \approx -1.645$). In CdS QD, the values for g^e are close to that in bulk CdS ($g^e \approx 1.77$) and their changes do not exceed 1%, when the excitation energy varies from 2.54 to 2.71 eV. We assume that for the experimental conditions of *size-selective excitation* of the QD, E_{ex} is equivalent to the excitation energy. Relatively

small variations of $g^e - g_0$ ($g_0 = 2$ is the free electron Landé factor) are expected since both, gap and spin-orbit splitting change rather little with the size-confinement. The increase in g^e with E_{ex} in both systems can be understood by **k·p** theory.

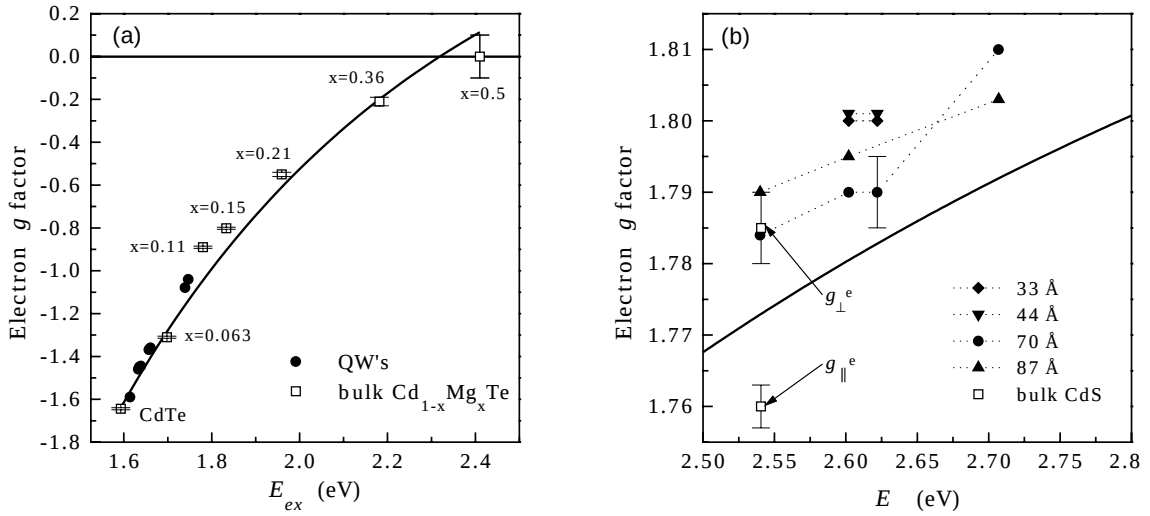

Figure 9: *Dependence of the electron g factor (filled symbols) on the energy of the ground exciton state E_{ex} in (a) CdTe/$Cd_{1-x}Mg_xTe$ QW and in (b) CdS QD with different mean radii of the nanocrystals (as indicated). The g factors for bulk $Cd_{1-x}Mg_xTe$ and the two components of g^e ($g^e_\parallel$ and $g^e_\perp$) for bulk CdS are shown by open squares. The solid lines represent a result of 5-band **k·p** model calculations.*

Results of a model calculation are shown in Figs. 9 a and 9 b by the solid lines. The good agreement with the experimental data leads to the conclusion that the variation of the electron g factor in nanostructures with structural parameters is mainly determined by confinement effects on the gap, i.e. by E_{ex}.

The SFRS technique also allows one to study the anisotropy of electron and hole g factors, which reveals itself in a dependence on the orientation of the magnetic field with respect to the crystal axes. In low-dimensional systems based on zinc-blende semiconductors, like CdTe/$Cd_{1-x}Mg_xTe$ QW, the point symmetry reduction from T_d (bulk) to D_{2d} (QW), due to both confinement and strain, results in a splitting between light- and heavy-hole states, ΔE_{lh-hh}. This splitting leads to the electron g factor anisotropy Δg ($\Delta g \equiv g^e_\perp - g^e_\parallel$, the symbols $\perp$ and $\parallel$ correspond to the orientation of B with respect to the growth direction z). Figure 10 shows the dependence of Δg on ΔE_{lh-hh} in different structures. The insert depicts the anisotropic behavior of g^e for different angles γ between B and z. The circles in Fig. 10 are for structures with different L_W and the same Mg content x = 0.15. Hence, they illustrate the effect of confinement. The triangles in Fig. 10 show the effect of the strain for structures with the same $L_W = 70$ Å and different x. Δg is *positive* in all QW studied and becomes larger with increasing ΔE_{lh-hh}.

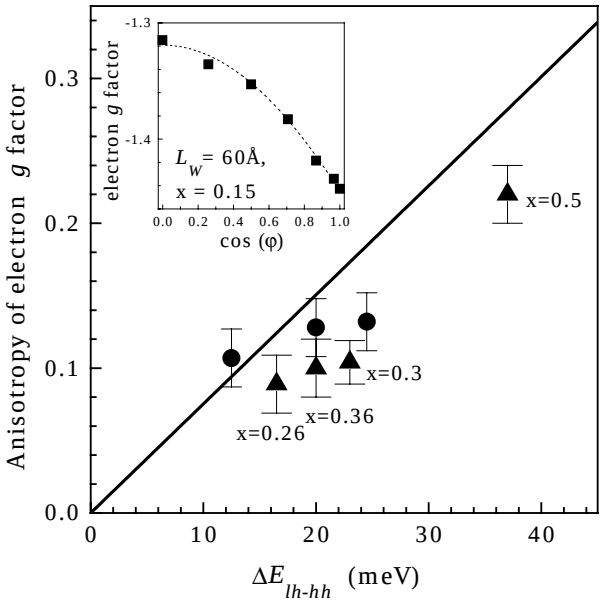

Figure 10: *Electron g factor anisotropy Δg versus the light-hole–heavy-hole splitting, ΔE_{lh-hh}, in CdTe/$Cd_{1-x}Mg_xTe$ QW with different QW widths and Mg content x. The solid line represents a 2-band **k·p** calculation. The inset depicts the anisotropic behavior of g^e for a L_W=60 Å QW.*

This trend can be illustrated using a 2-band **k·p** model for the Γ_6^c and Γ_8^v bands (solid line in Fig. 10). The contribution from other bands ($\Gamma_7^v, \Gamma_7^c, \Gamma_8^c$) to the electron g factor should be almost isotropic and can be neglected here.

In conclusion, the carrier g factors have been measured by SFRS in CdTe/CdMgTe QW and CdS QD. Their anisotropy and changes with different parameters have been described using 5-band **k·p** theory.

(A.A. Sirenko, T. Ruf, V.I. Belitsky, C. Trallero-Giner, A.I. Ekimov and M. Cardona; D.R. Yakovlev, W. Ossau, A. Waag and G. Landwehr (Univ. Würzburg))

Hydrogen molecules in semiconductors

Hydrogen is an important impurity in many semiconductors because of its tendency to form complexes with most crystal defects and impurities. In combination with its presence during crystal growth and processing it has gained both fundamental and technological interest. Extensive experimental and theoretical work on hydrogen in Si has lead to far greater understanding of the properties of hydrogen in this material compared to all other semiconductors. Theoretical calculations have predicted the formation of a stable hydrogen dimer in Si, either in the form of H_2^*, in which one hydrogen is in the bond-centered position while the other is in the antibonding position, or as the H_2 molecule, positioned at or near the interstitial tetrahedral site within the Si lattice. Although many experimental results were explained in terms of the formation of such dimer species, direct experimental evidence

for their existence in crystalline Si has proven to be difficult to obtain. Infrared modes gave the first evidence for the presence of the H_2^* defect in Si. A Raman line at 4158 cm^{-1}, was also recently identified as the vibrational excitation of the H_2 molecules in Si. Our study addresses the important question of the H_2 position in the Si lattice. After treatment of the Si samples in hydrogen/deuterium plasmas we detect the Raman lines due to H_2, D_2 and HD molecules (Fig. 11). The Raman frequencies are summarized in Table 1 and compared to Raman frequencies of hydrogen molecules in the gas, liquid or solid phase.

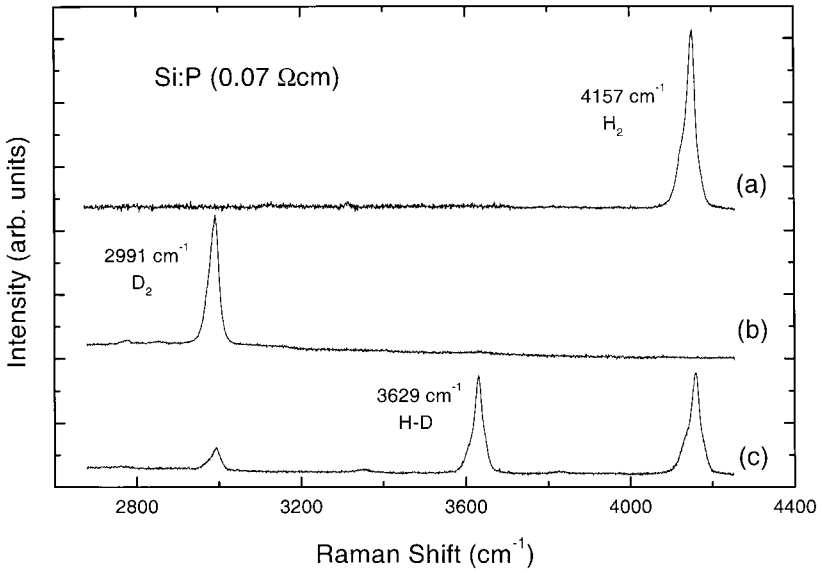

Figure 11: *Room temperature Raman spectra of Si:P, after exposure at 200° C for 8 hours to: (a) H_2 plasma, (b) D_2 plasma and (c) H_2/D_2 (50:50) plasma.*

Surprisingly, the Raman vibrational frequencies are very similar in Si and in H_2 gas. This is in contradiction to theoretical investigations, where a pronounced shift towards lower frequencies is calculated. The formation and the annealing of the Raman H_2 signal is very similar to the behavior of Si-H modes detected in the same samples, which are related to the formation of extended defects (platelets) by the plasma treatment. Our results strongly suggest that the H_2 molecules giving rise to the measured Raman lines are located within the voids created by the platelets.

Table 1. *Summary of the observed Raman transitions Q(0) of H_2, D_2, and HD molecules in different environments.*

matrix	H_2 (cm^{-1})	D_2 (cm^{-1})	HD (cm^{-1})
GaAs	3934.1	2842.6	3446.5
Si	4157	2991	3629
H_2 (gas)	4161.13	2993.55	3632.06
H_2 (liquid)	4153.78	2987.99	3623.65
H_2 (solid)	4151.8	2982.46	3621.85

The behavior of the H_2 molecules in GaAs is quite different. The Raman lines for H_2, D_2, and HD are much sharper in GaAs and the frequencies of the lines are clearly shifted from the position reported in hydrogen gas (Fig. 12). We interpret these lines as vibrational excitations of isolated H_2, D_2, and HD molecules, respectively, in the GaAs lattice. Table 1 summarizes the observed lines together with the corresponding transitions found in different matrices. The mass dependence is almost the same for all materials, although our frequencies are by 100–200 cm^{-1} lower than those found in the other matrices. The frequency ratio r of the H2-line by the D2-line is for all cases close to $\sqrt{2}$, the value that would be expected for a free, harmonic oscillation of two hydrogen (deuterium) atoms.

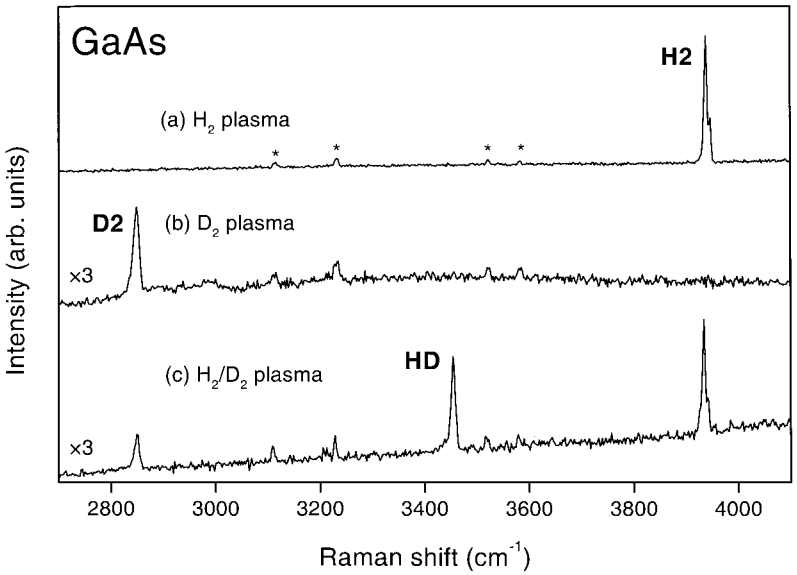

Figure 12: *Raman lines observed at T=77K after different plasma treatments. (a) SI-GaAs after 8 h H_2 plasma treatment at T=254° C. (b) LT-GaAs after 3 h D_2 plasma treatment at T=200° C. (c) SI-GaAs after 8 h H_2/D_2(50:50) plasma treatment at T=200° C. (*) indicates residual laser plasma lines.*

The H2-line measured with a higher resolution clearly shows a second, weaker component at 3934.1 cm^{-1}. No splitting is observed for the HD- and D2-lines. The linewidths of the H2-, HD-, and D2-lines are 3 cm^{-1}, 8 cm^{-1}, and 7 cm^{-1}, respectively. These results suggest a possible explanation for the observed 8 cm^{-1} large splitting of the H2-line, if one assumes a rotational motion of the H_2 molecules. Due to the nuclear spin of hydrogen, ortho-H_2 and para-H_2 states exist, which have due to the rovibrational coupling slightly different energies. The conversion of ortho-H_2 to para-H_2 is usually a very slow process with a time constant (in non-paramagnetic matrices) of many days. As a consequence, the room temperature distribution of 25% para-H_2 and 75% ortho-H_2 is maintained during the cooling down of the sample. Therefore, at low temperature, two Raman transitions are observed with an intensity ratio of 1 : 3.

In conclusion, our results show for the first time experimentally the existence of isolated hydrogen molecules trapped in the GaAs lattice. In agreement with theory, these molecules are only weakly perturbed by the host and can rotate easily. The influence of the GaAs matrix is reflected by a considerable frequency shift to lower values as compared to molecules in free space or in solid gas matrices. In Si, the hydrogen molecules are trapped in large extended defects, as evidenced by their vibrational frequencies, which are almost identical to those of the free molecules.

(V. Alex, A. Leitch, J. Vetterhöffer and J. Weber)

Silicon-Germanium layer stuctures for solar cell application grown by liquid phase epitaxy

Silicon-Germanium alloys have attracted interest because of their possible potential for applications in photovoltaics. Active SiGe layers increase the near-infrared absorption in a solar cell. A theoretical approach, in addition, has suggested the possibility to increase the efficiency limits of solar cells by carrier multiplication through Auger generation in cell structures which contain high Ge concentration. The major problem in the growth of SiGe/Si heterostructures is the lattice mismatch between SiGe layer and Si substrate. The lattice mismatch causes the formation of dislocations during the relaxation of the layers. Threading dislocations decrease the hole mobility. The density of dislocations penetrating the active layer can be reduced by growing a buffer layer in which the Ge concentration is graded continuously or step-wise. Liquid phase epitaxy is suitable for growing such graded SiGe layers and, furthermore, for producing SiGe layers of more than 20 μm in thickness.

The surface morphology of relaxed SiGe layers grown on (100) Si substrates shows a characteristic crosshatch pattern when grown with a low Ge concentration. Higher Ge content favors the development of pyramids. To avoid pattern formation and obtain layers of homogeneous thickness and almost flat surfaces, we used (111) Si substrates. The layers were grown in conventional LPE tipping boat systems or an LPE centrifuge for 4 inch-wafers under the conditions of near-thermodynamic-equilibrium in H_2 atmosphere at ambient pressure. As solvents indium, gallium or bismuth were used. They are different in their solubility for Si and Ge and in their incorporation as dopant into the layer. SiGe layers grown from Bi solution are only a few μm thick and show a rapid increase of the Ge content from the interface to the layer surface. This is ideal for a thin graded buffer layer. The active p-type SiGe layers were grown from In solution with Ga as dopant.

The structural quality of the layers was studied by electron microscopy. In a $Si_{0.9}Ge_{0.1}$ layer grown directly on the Si substrate misfit and threading dislocations were generated at the Si/SiGe interface and in the SiGe layers, respectively. The density of threading dislocations in the active SiGe layer is considerably reduced when grown on a buffer layer as shown in Fig. 13. Stress relaxation in the buffer layer takes place via lateral propagation

of dislocation loops in the lower part of the buffer, so that the upper part can grow almost dislocation-free. No more misfit dislocations nucleate at the interface between buffer and base layer. The etch pit density (EPD) of the 10at% Ge containing SiGe layer grown directly on the Si substrate was about $5 \times 10^7\,\mathrm{cm}^{-2}$. When this layer was grown on a buffer layer the observed EPD was less than $7 \times 10^5\,\mathrm{cm}^{-2}$.

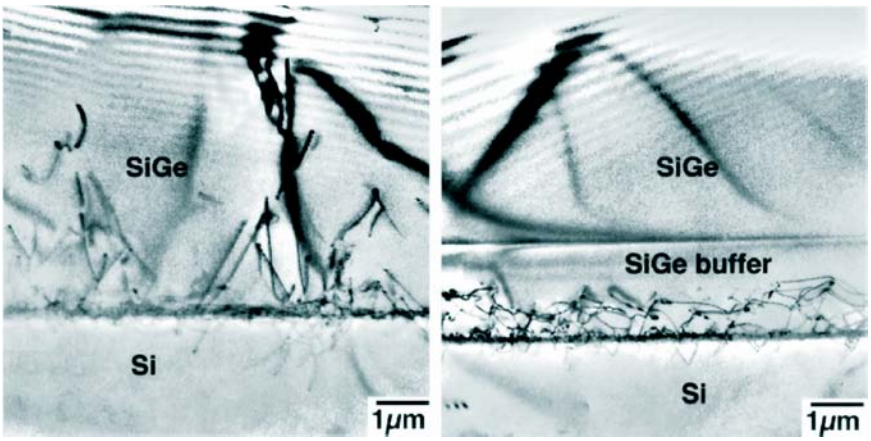

Figure 13: *Left: $Si_{0.9}Ge_{0.1}$ layer grown on (111) Si substrate. Misfit dislocations at the Si/SiGe interface; threading dislocations penetrate the layer. Right: $Si_{0.9}Ge_{0.1}$ layer grown with SiGe buffer layer on (111) Si substrate. Density of threading dislocations is strongly reduced. TEM-image.*

In collaboration with IMEC, Belgium, and other european partners first SiGe solar cells were processed with LPE-grown layers which have been grown directly on a (111) p^+-Si–substrate. The active base layer had a doping concentration of $5 \times 10^{16}\,\mathrm{cm}^{-3}$. The Ge content varied from 8at% at the Si/SiGe interface to 12at% at the surface. The emitter has been diffused from a solid source. Finally, the surface of the layer structures were passivated with silicon nitrides films which were deposited by remote or direct plasma CVD. Thermal oxidation (900°C) was avoided since it leads to degradation of both the surface and the bulk of the SiGe material. Remote plasma hydrogenation was also included in the process to passivate the dislocations and defects in the bulk of the SiGe epitaxial layer. However, it turned out that hydrogenation had no effect on cell performance with these layers, despite the fact that a dislocation density of $> 10^6\,\mathrm{cm}^{-2}$ had been found at the Si/SiGe interface. The conversion efficiency of these $4\,\mathrm{cm}^2$ large cells was found to be around 9%. The best cell with 9.1% efficiency has a short-circuit current of 24.4 $\mathrm{mA/cm}^2$, an open-circuit voltage of 540 mV and a fill factor of 68.9%. From the measured and the calculated internal quantum efficiency data a carrier diffusion length L_n greater than $70\,\mu$m was extracted. This value is 5 to 6 times larger than the layer thickness. Furthermore EBIC-data and the increase of the short circuit current of the cells by increasing the cell thickness indicate that the diffusion length is higher than the cell thickness.
Cells made from SiGe layers grown on graded SiGe buffer layers are currently under investigation. First results predict efficiencies higher than 9%.

(A. Gutjahr, M. Konuma, I. Silier, N. Rollbühler and F. Banhart; K. Rombach,
J. Poortmans and K. Said (IMEC, Belgium))

Metalicity and superconductivity in alkali-doped fullerides

The alkali-doped fullerides A_3C_{60} (A = K, Rb) have attracted much interest, not least because they are superconducting up to a relatively high transition temperature ($T_c \approx 30$–40 K). In these systems the electron-electron interaction is expected to play a large role. The effective Coulomb interaction between two electrons on the same molecule is $U \approx 1.2$–1.5 eV. This should be compared with the width $W \approx 0.6$–0.8 eV of the partly filled t_{1u} band. Since the ratio $U/W \approx 1.5$–2.5 is larger than unity, it has been argued that these systems are Mott-Hubbard insulators. The experimentally observed metalicity, would then be due to slight deviations from stoichiometry and the presence of a small number of holes. This would be a similar situation as for the high-T_c compounds, and it would probably have important implications for the explanation of the physical properties. In addition, the strong Coulomb repulsion raises questions about how this repulsion can be overcome by the rather weak phonon-induced attraction, leading to superconductivity.

There have been several studies of the criterion for a Mott-Hubbard metal-insulator transition, finding $U_c/W \approx 1$. These studies neglect the orbital degeneracy. For A_3C_{60} the partly filled t_{1u} orbital has a degeneracy N = 3, and we here study the effect of this degeneracy. We can express the band gap for a solid with M molecules and N electrons per molecule as

$$E_g = E(NM+1) + E(NM-1) - E(NM) \ , \tag{2}$$

where $E(K)$ is the ground state energy of a system with K electrons. Eq. (2) is simply the difference between the ionization and affinity energies, which is zero for a large metallic system. We first consider the limit when U is very large. For the case with K = NM electrons there are then N electrons on each molecule. Hopping is then almost completely suppressed, since this would cost the large energy U. We can then easily write down the energy $E(NM)$. The case with the extra electron ($E(NM+1)$) is illustrated in Fig. 14. One molecule now has N + 1 electrons, i.e. an extra electron.

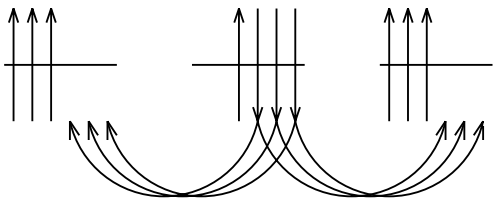

Figure 14: *Illustration of how the extra occupancy can hop in N different ways to a neighboring site for the orbital degeneracy N=3.*

The figure illustrates that this extra occupancy can hop to a given site in N ways (assuming a one-particle hopping matrix elements only between orbitals on neighboring sites with the same quantum number). The matrix element between the state in Fig. 14 and the state where the extra occupancy has moved to a neighboring site is then $\sqrt{N}t$, i.e. it has an extra factor $\sqrt{N}$ compared with the one-particle hopping matrix element t. This arguments

suggest a hopping energy of the order $\sqrt{N}W/2$ in E(NM + 1) and a similar contribution for E(NM – 1). Similar results are also obtained for more general assumptions about the hopping. This results in

$$E_g \sim U - \sqrt{N}W \ . \tag{3}$$

Extrapolating this result to intermediate values of U, we obtain the criterion for a Mott transition

$$U/W \sim \sqrt{N} \ . \tag{4}$$

The arguments above are not rigorous and they need to be checked. For this purpose we have performed exact diagonalization and quantum Monte Carlo calculations for a model of A_3C_{60}, which is essentially a Hubbard model with the orbital degeneracy N = 3. The exact diagonalization calculations illustrate that Eq. (3) is essentially right in the large U limit. For systems with few nearest neighbors we have found, however, a somewhat stronger dependence on N and for systems with frustration (nonbipartite lattices) we have found a prefactor that is somewhat larger than one.

To study the behavior for intermediate values of U, we need to consider larger systems than can be studied by exact diagonalization. For this purpose a lattice quantum Monte Carlo method was developed, using a fixed node like approximation. We found this method to be very accurate in cases where the accuracy can be checked. Figure 15 shows the band gap E_g. For U $\leq$1.5 eV the gap extrapolates to zero as $1/M \to 0$, while it stays finite for U $\geq$ 1.75 eV. This corresponds to $U/W \approx 2.5 \approx 1.5\sqrt{3}$, where the prefator 1.5 corresponds to the expected ratio for a nondegenerate frustrated system.

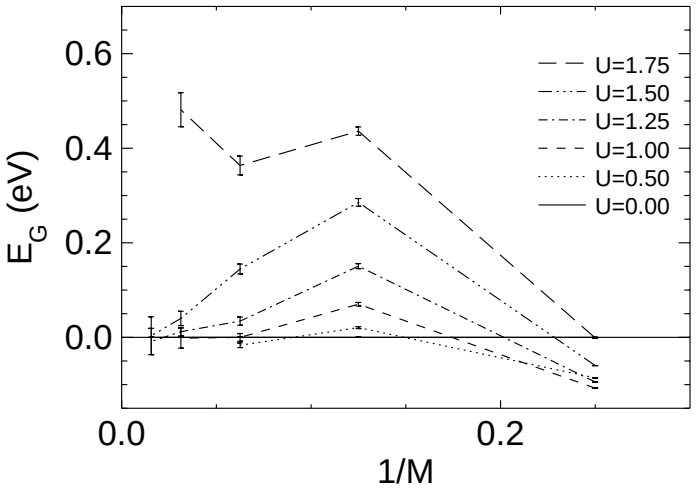

Figure 15: *The band gap for different U as a function of 1/M, where M is the number of molecules. E_G is the band gap E_g plus some finite size corrections. The band width is W=0.6eV.*

These calculations put the systems A_3C_{60} (A = K, Rb) on the metallic side of a Mott transition, implying that these systems are not doped Mott-Hubbard insulators. This is strongly supported by recent measurements of T_c as a function of doping. Our results suggest, however, that these systems are close to a Mott-Hubbard transition and indeed strongly correlated. Indeed, recently several alkali doped fullerides have been found, which are insulators at normal pressure but become metals under pressure, confirming that these systems are close to a transition.

Examples of the latter systems are A_4C_{60} and $NH_3K_3C_{60}$. A_4C_{60} (A = K, Rb, Cs) has a bct lattice structure, i.e. a bipartite (non-frustrated) lattice. Theoretical arguments suggest that the absence of frustration should reduce the prefactor in front of $\sqrt{N}$ in Eq. (4), which is supported by exact diagonalization calculations. This favors A_4C_{60} being on the insulating side of a Mott transition. Furthermore, in A_4C_{60} the t_{1u} has four electrons per molecule. Generalizations of the simple arguments above suggest a slight increase of the band gap for fillings different from half-filling, which also contributes to put A_4C_{60} on the insulating side of a Mott transition. Our Monte Carlo calculations therefore find A_4C_{60} to be an insulator with a gap of the right order of magnitude. Experiments furthermore find a substantially larger gap for K_4C_{60} (bct lattice) than for Na_4C_{60} (fcc lattice), confirming the importance of the lattice structure. $NH_3K_3C_{60}$ has a distorted fcc lattice, which substantially reduces the frustration. Preliminary calculations suggest that the insulating character, also in this case, can be understood in terms of a reduced frustration.

For conventional superconductors it is assumed that retardation effects strongly reduce the effective Coulomb interaction (Coulomb pseudopotential μ^*), allowing the phonon induced interaction to cause superconductivity. For the alkali-doped fullerides we have found that the retardation effects are very inefficient (see annual report 1992). Within the random phase approximation (RPA), however, screening can reduce the Coulomb interaction sufficiently to make superconductivity possible. The accuracy of the RPA for these strongly correlated systems is, however, an open question. To test this accuracy, we have introduced a test charge q_0 on one of the molecules in the model above. The screening charge on this molecule was then calculated, using the same QMC method as above. The results are shown in Fig. 16. The figure illustrates that RPA is surprisingly accurate until the system is very close to a Mott transition. On the insulating side, on the other hand, RPA is a very poor approximation, as expected. These results strongly support our earlier conclusion that the Coulomb pseudopotential μ^* is reduced primarily by screening effects and not by retardation effects, as assumed for conventional superconductors.

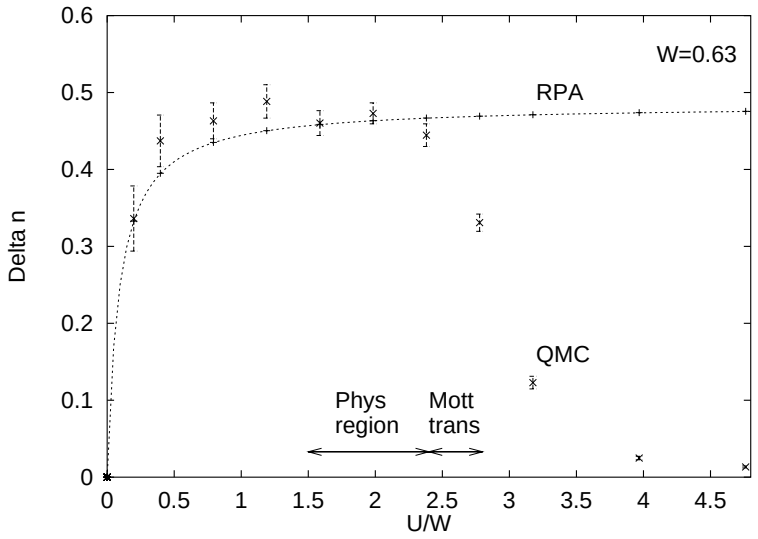

Figure 16: *Screening of a test charge q_0=0.5. Delta n is the screening charge on the same molecule as the test charge. The figure compares RPA and QMC as a function of U/W. RPA is quite accurate until the system is close to a Mott transition.*

$NH_3K_3C_{60}$ is an insulator at normal pressure but becomes a metal and a superconductor under pressure. It is interesting that for this system T_c grows with pressure, in strong contrast to A_3C_{60} (A = K, Rb). The screening results above suggest that as the pressure is increased and the system moves away from the Mott transition, the screening becomes more efficient. This would then reduce μ^* and increase T_c.

To summarize, we find that it is important to take the orbital degeneracy into account when studying the metal-insulator transition. The proper lattice structure (frustration) and the filling of the band are also important. We expect these considerations to be important also for other systems where Hubbard-like models are appropriate. We find a very efficient screening until the systems are very close to a Mott transition. This provides a different mechanism for reducing μ^* than the one assumed for conventional superconductors.

(E. Koch, O. Gunnarsson and R.M. Martin)

Carbon-nanotubes

For those interested in 'molecular electronics' nanotubes are intermediate between molecules and solids – small enough to show molecular properties (some 10 Å in diameter) and large enough to fit to present lithographic microstructures (some micrometer in length). But nanotubes are also of more immediate practical interest: Due to the small radius of curvature at their tip nanotubes are good electron emitters and can be used as electron nano-guns for displays, they are discussed as storage medium for hydrogen and other gases ('nanoscale gas cylinder') and – last but not least – they are better conducting and not more expensive than high quality carbon black and thus they are excellent fillers for conducting plastics.

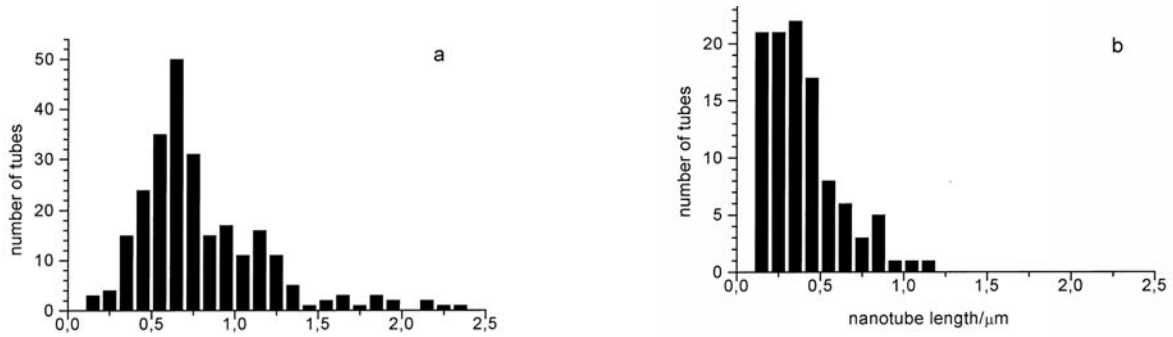

Figure 17: *Chromatographic separation of nanotubes. Histograms of nanotube lengths (scale in μm) in two different fractions obtained from one column.*

The production of carbon nanotubes is fairly easy: Vapor deposition from carbon plasma (evaporated graphite or cracked hydrocarbons). More complicated is the purification and separation from side-products. For this purpose we have developed a chromatographic procedure. The raw material is treated with detergents during agitation by ultrasound. This leads to stable aquaous suspensions, which can be passed through chromatographic columns. The fractions are not only free from side-products but also the tubes are selected by size, as indicated in the histograms of Fig. 17.

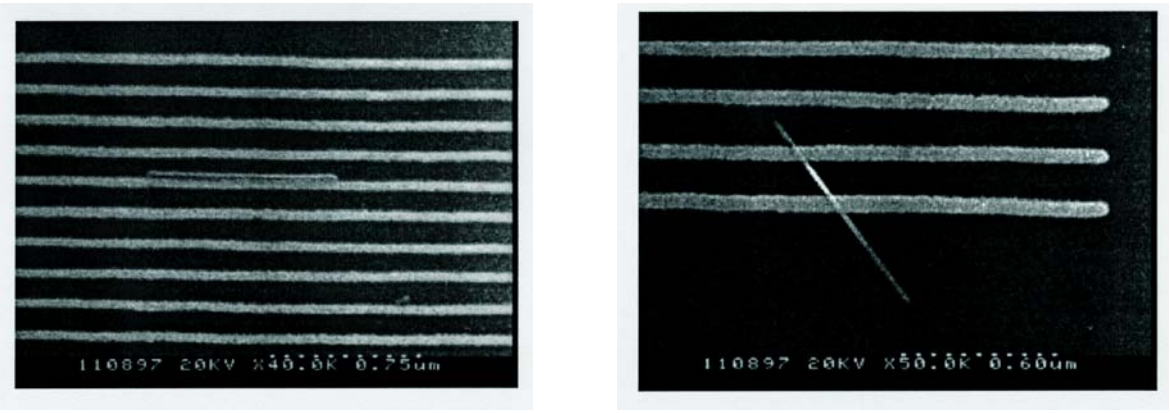

Figure 18: *Position-selective surface chemistry. Individual multi-walled nanotubes adsorbed in parallel (left) and with an angle (right) on electrode lines separated by 100nm.*

Carbon nanotubes can be manipulated by an STM tip. This method is useful for scientific investigations, but for any technical application it would be too time-consuming. A more practical technique is chemical self assembly and in particular *position-selective surface chemistry*. Figure 18 shows a silicon waver with a 1 μm oxide layer onto which gold leads have been deposited by electron beam lithography, about 50 nm wide and 100 nm apart. The chemical surface treatment of gold and of silicon oxide has been such that in one case the nanotubes prefer to align parallel and in the other perpendicular to the gold leads.

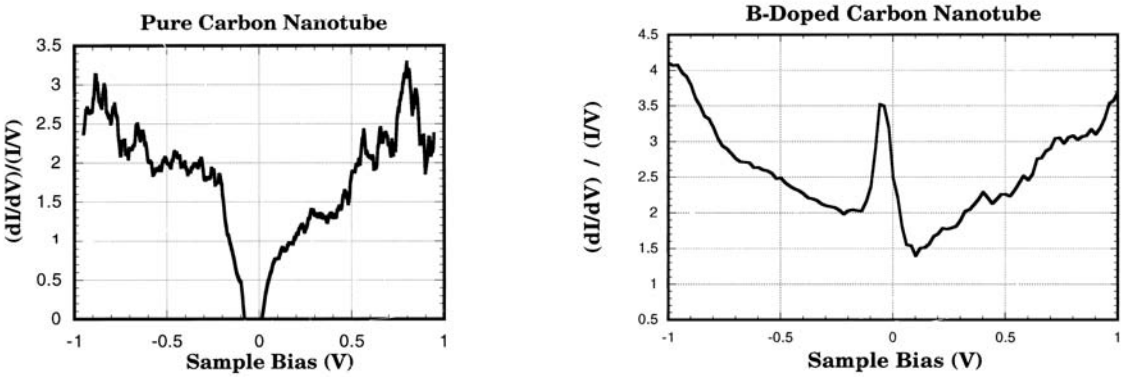

Figure 19: *Electronic density of states obtained from the scanning tunneling characteristics measured on a pure (left) and boron-doped (right) carbon nanotube.*

Depending on the diameter and the chirality (screw pitch), a carbon nanotube can be either semiconducting or metallic. The electronic density of states can be determined from scanning tunneling spectroscopy. Figure 19 shows the normalized derivative of the tunneling characteristic which is proportional to the density of states.

The upper panel is for a nanotube of pure carbon. A gap of about 0.1 eV is seen, which is reasonable for a tube with a fairly large diameter. The lower panel corresponds to a boron-doped tube, in which some carbon atoms have been replaced by boron. Now the tube is metallic (no gap) and there is a peak near the Fermi level.

The next step in our research efforts will be to correlate the density of states with transport properties – and in particular to look for tubes with 'intratubular junctions', where there are sections with different electronic properties along the tube.

(S. Roth, M. Burghard, G. Düsberg and S. Curran; Ph. Redlich (MPI für Metallforschung))

Carbon replacement in fullerene molecules

We have found that it is possible to replace a carbon atom in C_{60} (or C_{70}) by a transition metal, thus creating a cluster with composition MC_{59}. The first step in this process is to coat a C_{60} molecule with a partial layer of transition metal. This is accomplished by mixing C_{60} vapor and metal vapor in a low-pressure He buffer gas. Metal atoms condense onto the surface of the fullerene cage. The metal-coated C_{60} molecules are then heated and ionized with a short laser pulse while still in the vapor phase. The products are subsequently analyzed in a time-of-flight mass spectrometer. Different groups of transition metals react with the C_{60} in different ways. The reaction products of Ta or Nb with C_{60} are predominantly cube-shaped metal carbide clusters, e.g. $Ta_{18}C_{18}$, see Fig. 20.

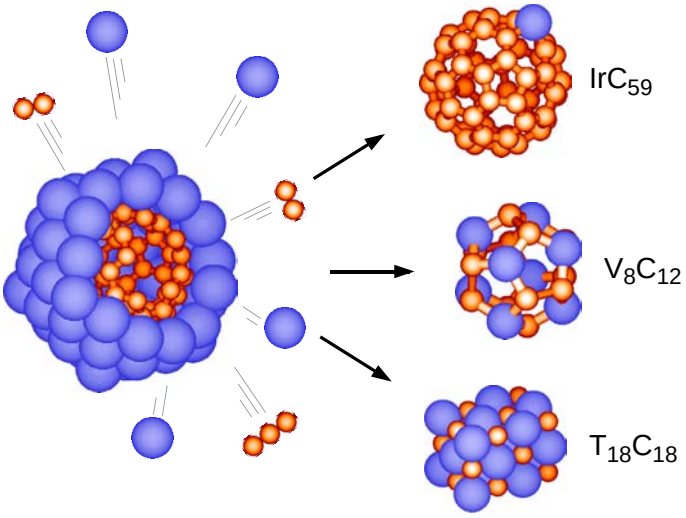

Figure 20: *When heated, transition metal coated C_{60} transforms to various reaction products.*

If vanadium or titanium-covered C_{60} is heated strongly enough, the principal product is the Met-Car M_8C_{12}, Fig. 20. Finally, several Fe, Ni, Co, Rh or Ir atoms on C_{60}, when heated, result in a replacement reaction yielding MC_{59}.

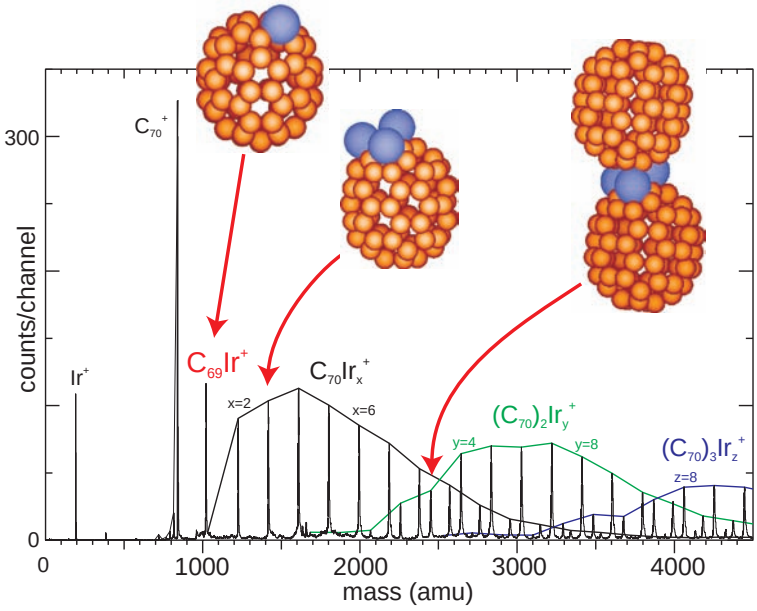

Figure 21: *Mass spectrum of the reaction products after laser heating $(C_{70})_xIr_y$ clusters. Notice the strong peak due to the reaction product $C_{69}Ir^+$.*

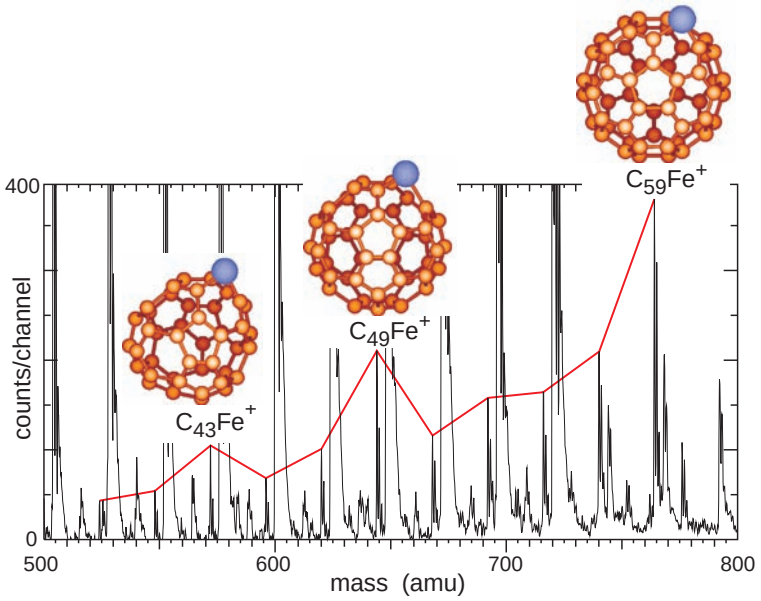

Figure 22: *Mass spectrum of the reaction products after laser heating $(C_{60})_xFe_y$ clusters. The relatively high intensity of peaks corresponding to clusters containing a total of 60, 50 and 44 atoms indicate a fullerene cage structure.*

The replacement reaction is particularly strong for iridium on C_{60} or C_{70}. Neutral clusters having the composition $(C_{70})_xIr_y$ were heated and ionized with a laser pulse of 193 nm.

The laser fluence was moderate, insufficient to cause appreciable carbon loss in the pure C_{70} molecule, yet strong enough to create $C_{69}Ir^+$, see Fig. 21. Since fullerene cage structures must contain an even number of atoms, this cluster cannot correspond to an isolated iridium atom on the surface of a fullerene. Notice also that the mass peak corresponding to $C_{70}Ir^+$ is negligibly weak in Fig. 21. Therefore, it seems that $C_{69}Ir^+$ might be a 70 atom fullerene.

However, we need additional evidence that Ir has replaced a carbon atom in the cage, since this mass peak could conceivably indicate the formation of a metal carbide molecule IrC on the outside of the cage structure C_{68}. This evidence has been found by examining the interaction of Fe and Co with C_{60}. If Fe or Co coated C_{60} is intensely heated with a laser pulse, not only MC_{59} is observed among the reaction products, but also MC_{57}, MC_{55}, MC_{53} ... MC_{41}. Within this set, the mass peaks for MC_{59}, MC_{49} and MC_{43} are particularly intense, see Fig. 22. It is a well established fact that the pure carbon fullerenes having 60, 50, and 44 atoms are unusually stable. Figure 22 indicates that the same cage structures containing one metal atom retain this characteristic.

(W. Branz, F. Tast, N. Malinowski, M. Heinebrodt, I.M.L. Billas and T.P. Martin)

Far infrared (FIR) ellipsometric study of the c-axis optical response of $Y_{1-x}Ca_xBa_2Cu_3O_{7-\delta}$

The non-metallic and incoherent electronic c-axis conductivity $\sigma_c^{el}(\omega,T)$ of the cuprate high-T_c superconductors has attracted considerable attention. The most peculiar feature is the gap-like suppression of $\sigma_c^{el}(\omega,T)$ in the normal state which has recently been observed in underdoped $YBa_2Cu_3O_{7-\delta}$ (Y-123) crystals. This observation has raised the question of whether the unusual properties of the c-axis conductivity are related to the pseudogap in the spin- and charge excitations of the CuO_2 planes rather than to the insulating rocksalt layers which separate the metallic CuO_2 planes and act like 'blocking layers'. In the former case $\sigma_c^{el}(\omega,T)$ should evolve as a function of the hole doping of the CuO_2 planes, in analogy to the pseudogap which occurs only for underdoped samples and disappears right at optimum doping. In the latter case the anomalous features of $\sigma_c^{el}(\omega,T)$ should depend on the structural and electronic details of the 'blocking layers'. In particular, for Y-123 the CuO chains should have a pronounced influence since they seem to become metallic upon oxygenation and reduce the thickness of the 'blocking layer'.

In order to resolve this question we have performed ellipsometric measurements of the far infrared (FIR) c-axis conductivity $\sigma_c(\omega,T)$ on a series of $Y_{1-x}Ca_xBa_2Cu_3O_{7-\delta}$ single crystals for x = 0 and 0.14 and variable δ. The partial substitution of Y^{3+} by Ca^{2+} introduces extra holes into the CuO_2 planes in addition to those that are transferred from the CuO chains as controlled by the oxygen content. This enables us to access almost the entire doping range from strongly underdoped to strongly overdoped. Furthermore, the opposing effects of hole doping due to the Ca-substitution and hole depletion due to a deoxygenation of the CuO chains allows us to study samples which have a comparable doping state of the CuO_2 planes but significantly different oxygen content and metallic properties of the CuO chains.

The ellipsometry measurements have been performed at the U4IR beamline of the National Synchrotron Light Source (NSLS), Brookhaven National Laboratory, USA, using a home-built setup attached to a Nicolet Fourier spectrometer. The high brilliance of the synchrotron allows us to perform accurate measurements on crystals with ac-faces as small as $0.5 \times 1\,mm^2$. The ellipsometry technique provides significant advantages over conventional reflection methods. Ellipsometry is self normalizing and does not require a reference sample. The real and the imaginary parts of the dielectric function are obtained directly without a Kramers-Kronig transformation and therefore no extrapolation beyond the measured range is necessary. Figure 23 a to 23 d shows the data for the Ca-free Y-123 crystals which are more fully oxygenated at a given doping state. Figure 24 a to 24 f shows the real part of the FIR c-axis conductivity $\sigma_{1c}(\omega,T)$ for the $Y_{0.86}Ca_{0.14}$ $Ba_2Cu_3O_{7-\delta}$ single crystals in order of increasing oxygen content and doping.

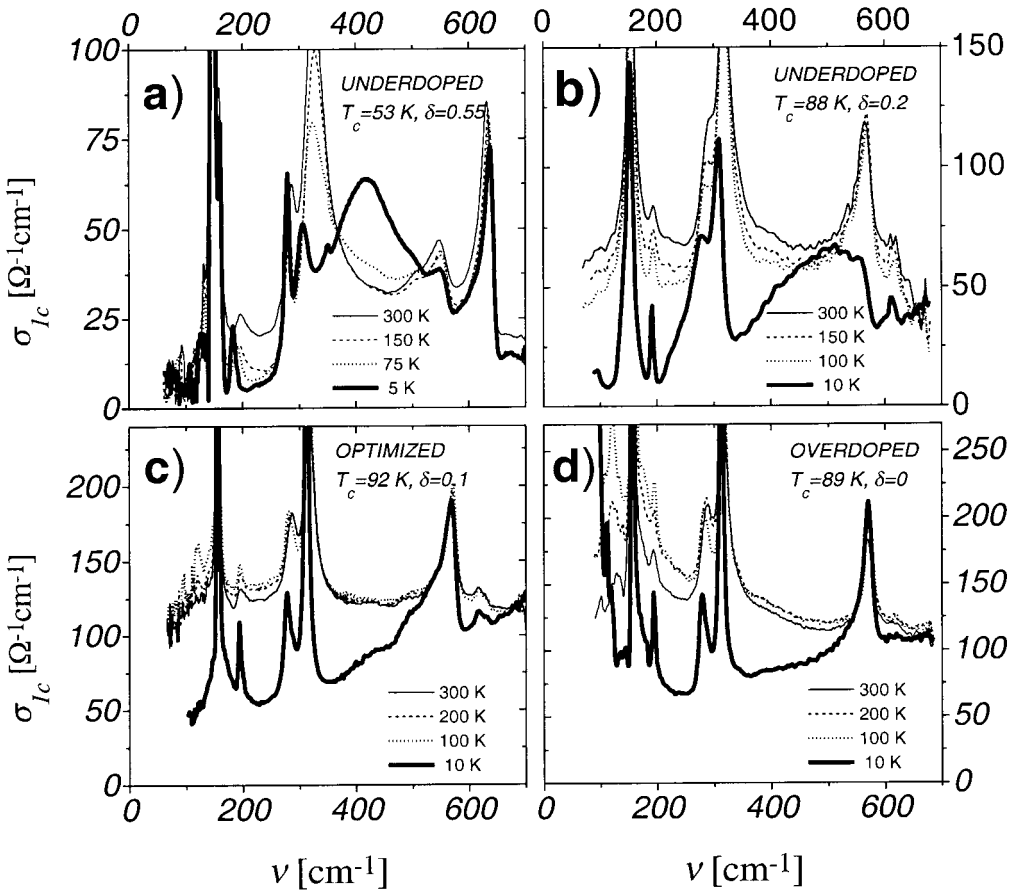

Figure 23: *The real part of the FIR c-axis conductivity of a $YBa_2Cu_3O_{7-\delta}$ single crystal for variable oxygen deficiency δ and doping of a) δ=0.55, T_c=53K (underdoped); b) δ=0.2, T_c=88K (underdoped); c) δ=0.1, T_c=92K (optimally doped) and d) δ=0, T_c=89K (overdoped). The data are shown in the SC state by the thick solid lines, in the normal state just above T_c by the dotted lines, at intermediate temperatures by the dashed lines and at room temperature by the thin solid lines.*

The oxygen deficiency of the crystals can be estimated from the spectral weight of the phonon mode at 620 cm^{-1} which involves the vibration of an apex oxygen next to an empty chain fragment. This mode is absent for the fully oxygenated crystals while its spectral weight increases with the oxygen deficiency. There are five more IR-active phonon modes superimposed on the electronic background which will not be further discussed here. From Figs. 23 a, 23 b and 24 a, 24 b it is apparent that all the underdoped samples exhibit a gap-like suppression of $\sigma_{1c}^{\mathrm{el}}(\omega, \mathrm{T})$ already in the normal state. The gap-like decrease of $\sigma_{1c}^{\mathrm{el}}(\omega, \mathrm{T})$ with decreasing temperature forms below $\nu < 650$–$700\,\mathrm{cm}^{-1}$. For the strongly underdoped samples it is somewhat obscured by a broad peak at 400–500 cm^{-1} which is of phononic origin and grows at the expense of the phonons at 320 cm^{-1} and at 570 cm^{-1}.

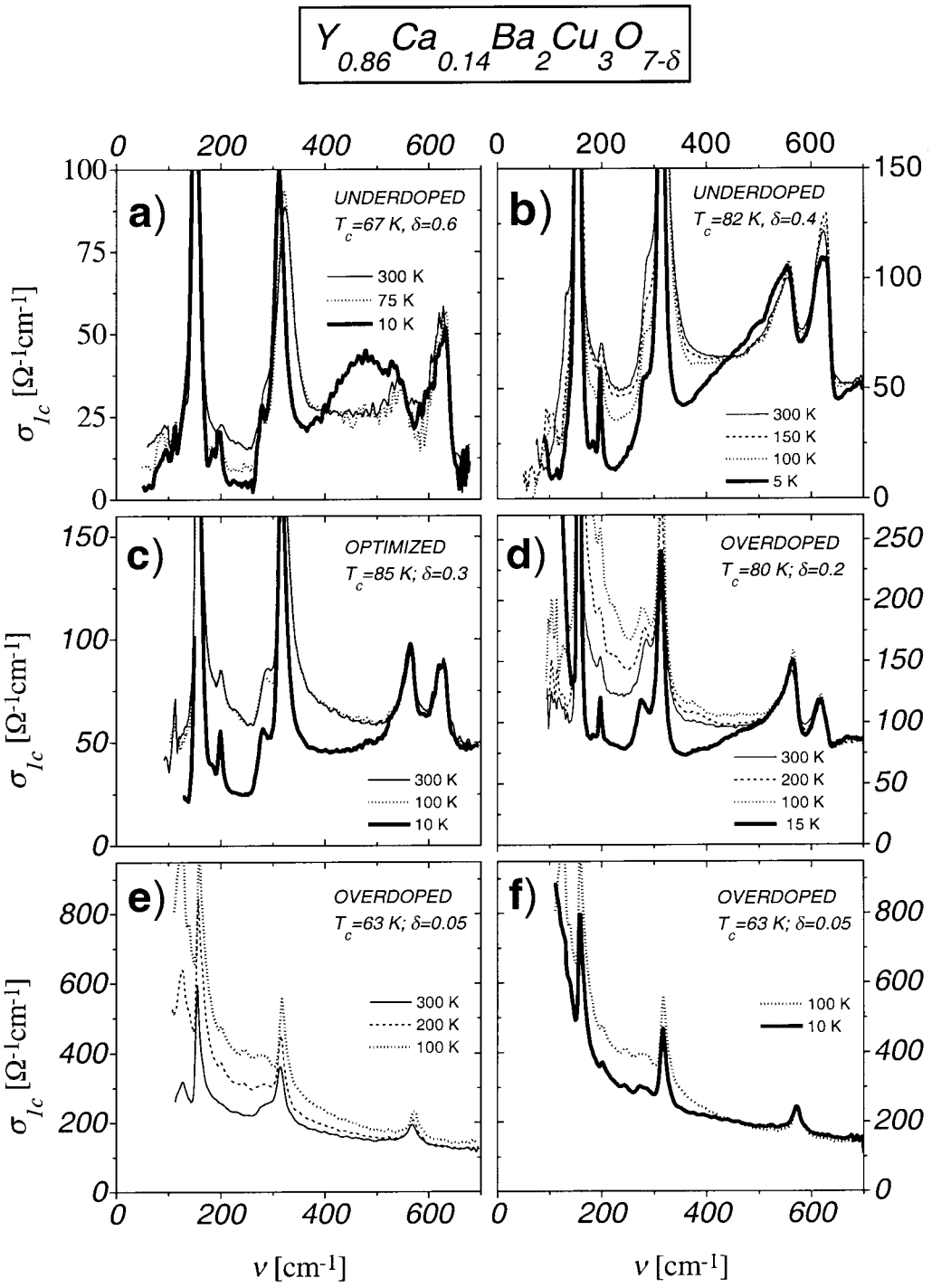

Figure 24: *The real part of the FIR c-axis conductivity of the $Y_{0.86}Ca_{0.14}Ba_2Cu_3O_{7-\delta}$ single crystal with variable oxygen deficiency δ and doping of a) δ=0.6, T_c=67K (underdoped); b) δ=0.4, T_c=82K (underdoped); c) δ=0.3, T_c=85K (optimally doped); d) δ=0.2, T_c=80K (overdoped) and e, f) δ=0.05, T_c=63K (overdoped). The data are shown in the SC state by the thick solid lines, in the normal state just above T_c by the dotted lines, at intermediate temperatures by the dashed lines and at room temperature by the thin solid lines.*

Figure 23 c and 24 c show that the gap like suppression of $\sigma_{1c}^{el}(\omega, T)$ above T_c disappears right at optimum doping. For both optimally doped samples $\sigma_{1c}^{el}(\omega, T)$ is almost independent of temperature and frequency in the normal state. Evidently, the temperature- and the frequency dependence of $\sigma_{1c}^{el}(\omega, T)$ are determined solely by the doping state of the CuO_2 planes. The oxygen deficiency and the metallic properties of the CuO chains merely affect the absolute values of $\sigma_{1c}^{el}(\omega, T)$ which are higher for the Ca-free Y-123 crystals. Right past optimum doping for the overdoped crystals $\sigma_{1c}^{el}(\omega, T)$ exhibits a metallic behavior since it increases with decreasing temperature and frequency. For the most strongly overdoped crystal the absolute values of $\sigma_{1c}^{el}(\omega, T)$ seem to be the highest reported for a cuprate superconductor.

Overall, our data confirm that the gap-like suppression of $\sigma_{1c}^{el}(\omega,T)$ in the normal state occurs only for underdoped samples while it disappears right at optimum doping. This analogy in the doping dependence suggest a close relationship to the pseudogap-effect which depletes the low energy spin- and charge excitations of the CuO_2 planes. Therefore, the non-metallic and incoherent c-axis charge dynamics of the underdoped cuprates appears to be an intrinsic property of the spin- and charge dynamics of the CuO_2 planes which confines the charge carriers.

For the overdoped crystals this confinement is gradually relaxed since $\sigma_{1c}^{el}(\omega,T)$ exhibits a metallic dependence on temperature and frequency. Simultaneously, however, we observe a suppression of the SC critical temperature T_c and the SC energy gap 2Δ, which can be estimated from the onset of the loss of spectral weight in the SC state when the carriers condense into a delta function at zero frequency. In addition, a growing fraction of the charge carriers remains unpaired in the SC state (see Figs. 23 d, 23 f and 24 d). These effects indicate that SC state is suppressed by strong pair breaking in the overdoped regime. This raises the question of whether the pseudogap and the confinement of the charge carriers are necessary prerequisites for the occurence of high-T_c superconducitivty in the cuprates.

We are indebted to D. Böhme for technical assistance and to L. Carr and G.P. Williams for support at the U4IR beamline of the NSLS. We also acknowledge the magnetization measurements by E. Brücher and R.K. Kremer. The Ca-substituted crystals were provided by M. Kläser (Universität Karlsruhe) and Th. Wolf (Forschungszentrum Karlsruhe). The Ca-free crystals were grown by C.T. Lin.

(C. Bernhard, R. Henn, A. Wittlin and M. Cardona)

Strongly correlated electrons coupled to optical phonons

The role of the electron-phonon (e-ph) coupling for the mechanism leading to superconductivity (SC) in the high-T_c cuprates is still controversial. The importance of electronic correlations suggests itself from the fact that the high-T_c is achieved upon doping a Mott insulator. Hence, many theoretical approaches neglect the phonons altogether and search for a purely electronic mechanism. An obvious shortcoming of such theories is the fact that they would never lead to an isotope effect.

While the experimental situation concerning the magnitude of the isotope effect and the relevant ions producing it is still not quite settled, it appears to be widely accepted by now that especially for underdoped samples, T_c is rather susceptible especially to the mass of the oxygen ions (Zech *et al.*, 1994). Near optimal doping, however, only a small isotope effect is observed. In addition, anomalous frequency shifts of phonon modes as well as other lattice anomalies have been observed at or slightly above T_c (see review by Egami and Billinge, 1994). These findings strongly suggest that the electronic and phonon degrees of freedom should be treated on an *equal footing*.

The simplest model to describe the *electronic* low-energy properties of doped CuO_2 sheets is the t-J model (Zhang and Rice, 1988). The oxygen bond stretching modes, which have the highest frequency in the cuprates, can couple effectively to the local charge density through the variation of the Zhang-Rice singlet energy upon displacement of the in-plane oxygen ions. Taking this effect into account, we arrive at the generalized t-J Holstein model for CuO_2 sheets or chains (Poilblanc *et al.*, 1996),

$$H = -t \sum_{\langle i,j\rangle,s} P_i c^\dagger_{is} c_{js} P_j + J \sum_{\langle i,j\rangle} \left(\mathbf{S}_i \cdot \mathbf{S}_j - \frac{1}{4} n_i n_j \right)$$

$$+ \hbar\Omega \sum_{i,\delta} a^\dagger_{i,\delta} a_{i,\delta} + \Lambda \sum_{i,\delta} (n_i - n_{i+\delta}) \left(a_{i,\delta} + a^\dagger_{i,\delta} \right) .$$

Here, we have simply added a free phonon term, and the e-ph interaction resulting from the Zhang-Rice singlet energy variation (linear in the oxygen displacement) to the usual t-J model. The label δ differentiates between **x** and **y** bonds, and $a_{i,\delta}$ is the phonon annihilation operator belonging to the oxygen between the copper sites i and $i+\delta$. The above coupling was shown to lead to strong renormalization and anomalous line shapes for the bond stretching modes at $\mathbf{k} = (\pi, 0)$ (Khaliullin and Horsch, 1997). A simpler (and often used) version of the e-ph term couples a *single* oscillator per site to the *local* charge density n_i rather than the difference $n_i - n_{i+\delta}$. This could be appropriate to describe the coupling of the Zhang-Rice singlet to apical oxygen vibrations. Below we shall elaborate on the difference between the two possibilities. Realistic values for the CuO_2 sheets are $t = 0.4\,\mathrm{eV}$, and $J/t = 1/3$.

The t-J Holstein model can not be solved analytically, and even a reliable numerical treatment with currently available methods is restricted to the case of one dimension (1D). Hence, we limit ourselves to 1D, and use numerical diagonalization supplemented by a

variational truncation of the phonon Hilbert space to map out the ground state phase diagram of the model. The variational truncation consists in restricting to a finite number of phonon states per site, and is well controlled.

Of particular interest is the influence of the e-ph coupling on SC correlations. Quantum fluctuations do not allow long range SC order in 1D, however, by studying the range of the fluctuations it is possible to indicate whether a small coupling in the other two space dimensions could lead to a SC ground state. The correlations of longest range can be determined by calculating a single correlation exponent K_ρ, which characterizes the Luttinger liquid. The latter is the generic fixed point for interacting gapless metallic electrons in 1D, analogous to the Landau Fermi liquid in higher dimensions. The SC correlations decay at long distances asymptotically like $\langle P^\dagger(x)P(0)\rangle \sim x^{-(K_\rho+1/K_\rho)}$.

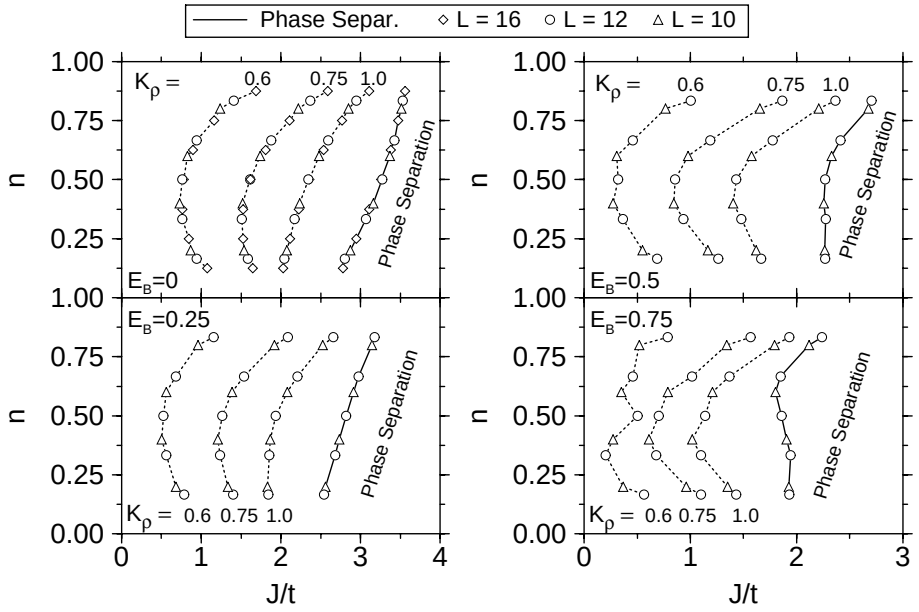

Figure 25: *The zero temperature phase diagram of the 1D t-J Holstein model for Ω/t=0.2 at various values of the e-ph coupling E_B and system sizes L. The plots show the phase separation boundary, and lines of constant K_ρ.*

Among the three competing possibilities (charge density wave, spin density wave, singlet SC), the SC correlations are of longest range provided $K_\rho > 1$. In the standard t-J model this occurs for $2 < J/t > 3$, while at even larger values of $J/t > 3$, a phase separated state is stabilized, where holes cluster together. The phase separation boundary is determined by the zeros of the inverse compressibility κ^{-1}. In Fig. 25, we show the phase diagram in the J – n plane for different e-ph couplings $E_B/t = \Lambda^2/\Omega t$, and fixed phonon frequency $\Omega/t = 0.2$ (experimental values for the oxygen bond stretching or apical modes are 50–80 meV), for the case of the *local* coupling. Its effect is to shift the region of dominant SC correlations ($K_\rho > 1$) to smaller J/t, i.e. into a more realistic regime. Hence, this type of coupling is possibly helpful for SC. At the same time, the onset of phase separation is shifted in a similar way to smaller J/t. The size of the region with dominating SC correlations remains roughly constant.

A more detailed analysis of the SC correlations is achieved by measuring the singlet pair-pair correlation function $D_{pair}(j) = \langle P_j^\dagger P_0 \rangle$, (where $P_j^\dagger = (c_{j,\uparrow}^\dagger c_{j+1\downarrow}^\dagger - c_{j,\downarrow}^\dagger c_{j+1\uparrow}^\dagger)/\sqrt{2}$) and its susceptibility $S_{pair}(k) = \frac{1}{L}\sum_{j,l}^{L} e^{ik(j-l)} \langle P_j^\dagger P_l \rangle$. Looking at the results for quarter filling in Fig. 26, we notice a *suppression* of the SC correlations as the e-ph coupling is increased. The peak in $S_{pair}(k=0)$ signals the onset of phase separation. Note, that there is a small discrepancy between the critical J value as determined by the zeros of κ^{-1} (indicated by the arrows in Fig. 26 a, and the position of the peak in $S_{pair}(k=0)$. This is due to finite size effects.

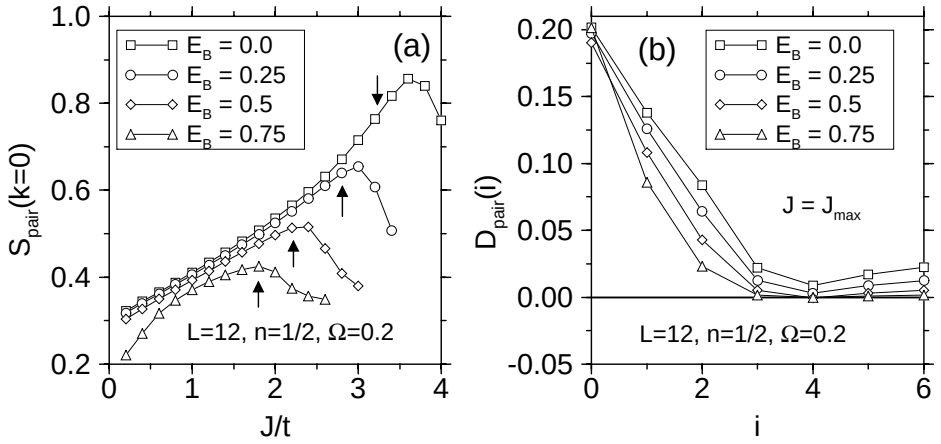

Figure 26: *(a) The singlet SC structure factor $S_{pair}(k=0)$ for various E_B. The arrows mark the occurrence of phase separation. (b) The pair-pair correlation function $D_{pair}(i)$ for various E_B evaluated at the value $J=J_{max}(E_B)$, where $S_{pair}(k=0,J,E_B)$ has a maximum.*

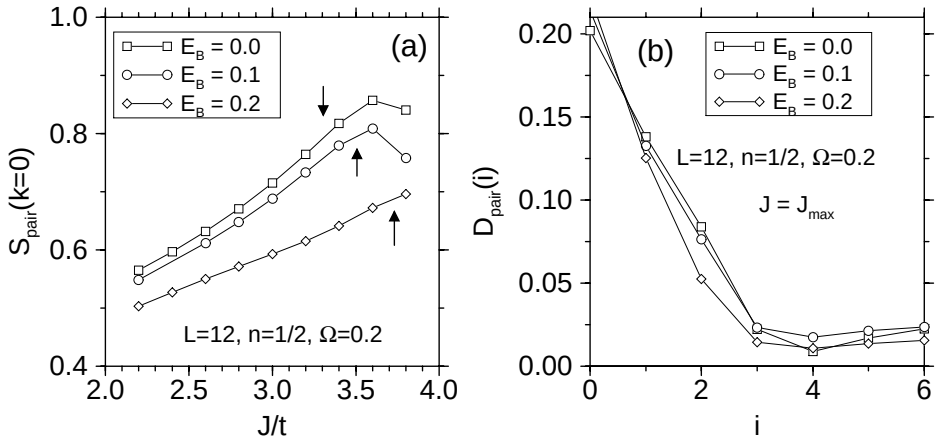

Figure 27: *(a) The singlet SC structure factor $S_{pair}(k=0)$ for the non-local e-ph coupling and various E_B. The arrows mark the occurrence of phase separation. (b) The pair-pair correlation function $D_{pair}(i)$ for various E_B evaluated at the value $J=J_{max}(E_B)$, where $S_{pair}(k=0,J,E_B)$ has a maximum.*

These results clearly demonstrate that for constant J, the local e-ph coupling suppresses the tendency towards superconductivity. However, it also slows down the charge motion, which results in an increase of the effective J/t ratio. Hence, SC correlations dominate at smaller, more realistic J values.

Turning to calculations using the non-local (q-dependent) e-ph coupling, Fig. 27 shows $D_{pair}(i)$, and $S_{pair}(k=0)$ evaluated for this case. While we see a similar suppression of both quantities, the marked difference to the local case is that the peak in $S_{pair}(k=0)$ is now moving to larger J/t as the e-ph coupling is increased. This means that the phase separation and the region of dominating SC correlations adjacent to it are pushed to even more unrealistic values of J, leaving no positive effect of the e-ph coupling on SC.

In conclusion, our results indicate that within an approach of strongly interacting electrons, the bond stretching and apical oxygen phonon modes which are expected to have the strongest e-ph coupling in the high-T_c cuprates suppress SC correlations. On the other hand, a favorable effect of a pure local coupling (as it would arise from coupling to the apical oxygen modes) is to increase the effective J/t ratio. Moreover, a q-dependent coupling, appropriate for the bond stretching modes of the in-plane oxygens, only leads to a weakening of SC tendencies.

(R. Fehrenbacher)

From LDA band structures to few-orbital tight-binding Hamiltonians: Applications to the van Hove scenario of high-T_c materials and to ladder compounds

Current research in high-temperature superconducting materials suggests the importance of the LDA electronic band dispersion, in addition to correlation effects. There is therefore a need for constructing *ab-initio* tight-binding Hamiltonians which are capable of reproducing the details of the LDA band structures close to the Fermi level and which are sufficiently simple that they can serve as the one-electron part of the full many body Hamiltonians.

Though the traditional LMTO–ASA method provided a tight-binding representation for the Hamiltonian, it was not possible to extract accurate *ab-initio* tight-binding parameters for a few orbital Hamiltonian in an automatic way. In recent years an improved version of the LMTO method has been proposed which satisfies this objective. The elegant feature of the new LMTO method which makes an accurate reduction of the problem possible is that the Hamiltonian can be expanded in two-centered tight-binding terms even when the combined correction is included and after the downfolding procedure has been performed.

A further advantage of the new LMTO method is that the basis functions are complete to first order in $(E-E_\nu)$ (E_ν is the energy about which linearization is performed) in both muffin-tin spheres *as well as* in the interstitial region. This increases the energy range over which the band structure is accurate. Since the downfolding procedure introduces additional energy dependences of the Hamiltonian one now expects the description of band structure after massive downfolding to be accurate over a wider energy range.

Here we present an application of the improved method for getting a few band tight-binding Hamiltonian for infinite-layer $CaCuO_2$. The LDA band structure for this material, properly relaxed, is very similar to other well characterized high-T_c materials. We have performed our study for $CaCuO_2$ in the primitive tetragonal structure consisting of parallel copper-oxygen planes perpendicular to the c-axis with copper on a square lattice and oxygen bridging the coppers in the a- and b-directions but slightly out of the copper planes with a $+7^o$ buckling angle in the a-direction and a -7^o buckling angle in the b-direction. Calcium separates the planes above the center of the copper square. Figure 28 a shows the full LDA band structure for $CaCuO_2$ between the $k_{||}$ points (0,0), (π/a,0), ($\pi/a, \pi/b$) and (0,0) for $k_z = \pi/2c$, i.e. half way between the $k_z = 0$ and the first Brillouin zone boundary plane in the k_z direction. Figure 28 b shows the oxygen p-bands after downfolding of all other orbitals. Figure 28 c shows the $Cu_{x^2-y^2}$ band which is obtained by downfolding all other orbitals. It may be seen that there is excellent agreement between this band and the equivalent band in Fig. 28 a over an energy range of 2 eV around the Fermi energy. Unfortunately the tight-binding Hamiltonian for this one-band model is very long ranged.

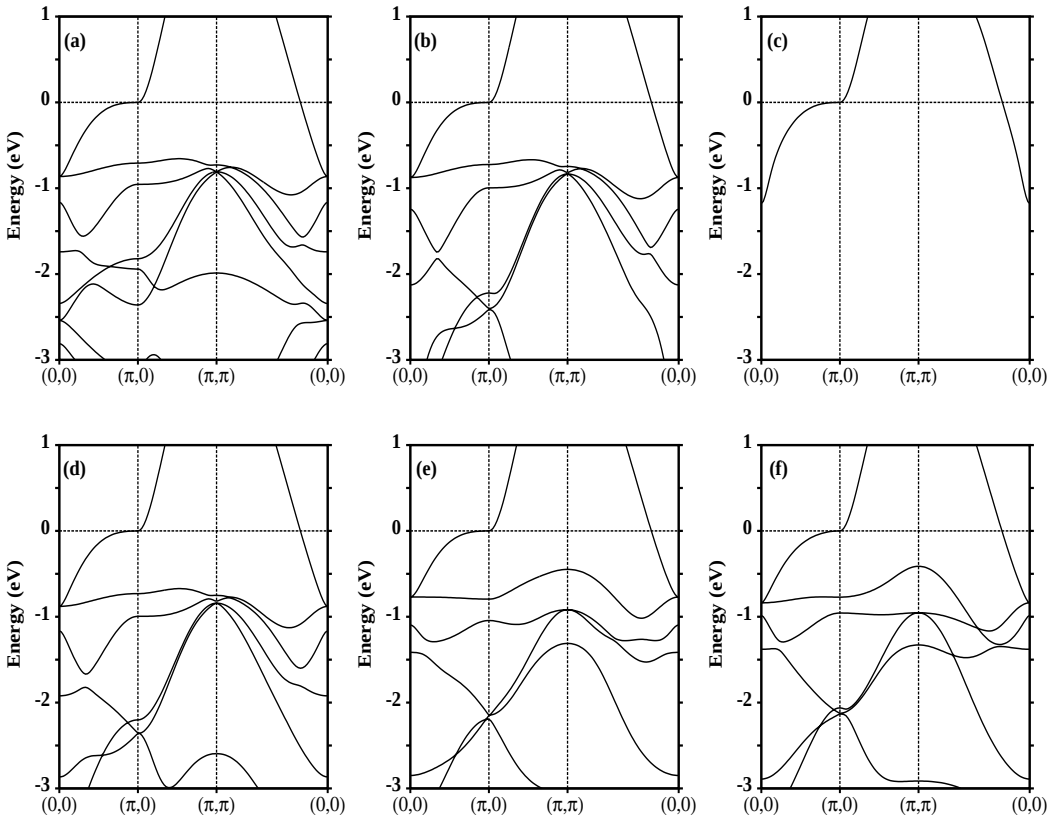

Figure 28: *The electronic structure of $CaCuO_2$ from various models. (a) The full LDA band structure around the Fermi level which is zero. (b) The energy bands with all orbitals downfolded except for the six oxygen p-orbitals. (c) The energy band from an orthogonal $Cu_{x^2-y^2}$ single orbital Hamiltonian. (d) The LMTO electronic structure for the eight band model. (e) The same as (d) but for an orthogonal representation. (f) The electronic structure from the eight band orthogonal tight-binding model with up to second neighbor interactions.*

It may therefore be more useful to explicitly keep more orbitals in the basis in order to achieve shorter range. For the present compound eight orbitals are sufficient to obtain this, namely four orbitals with σ interactions: $\mathrm{Cu}_{x^2-y^2}$, Cu_s, Oa_x and Ob_y (the labels a and b indicate the crystallographic directions relative to copper in which oxygen is sitting) and four orbitals with π interactions: Oa_y, Ob_x, Oa_z and Ob_z. The LMTO band structure with all other orbitals than these downfolded is shown in Fig. 28 d. Figure 28 e shows the electronic structure obtained from this eight orbital Hamiltonian transformed to an orthogonal representation. Finally the eight orbital Hamiltonian was Fourier transformed to real space and the band structure of this, after elimination of the small hopping integrals going beyond second nearest neighbor, is shown in Fig. 28 f. Again there is excellent agreement with the full band structure in Fig. 28 a over an energy range of about 2eV around the Fermi level.

The eight orbital chemical Hamiltonian discussed above for $\mathrm{CaCuO_2}$ is generic for the cuprates and it may be Löwdin downfolded to an energy dependent one band Hamiltonian. This provides further insights and is useful for a weak-coupling treatment of the many-particle interactions. If the in-plane oxygen π orbitals Oa_y and Ob_x are removed and only the nearest neighbor interactions are retained then the constant energy contours (CEC) may be obtained as the k-roots of the simple function $\mathrm{F}(\varepsilon,\mathrm{k}) \equiv \mathrm{u} - \mathrm{d}(\varepsilon) - \mathrm{v}^2(\mathrm{u} + \mathrm{s}(\varepsilon)) + (2 - \mathrm{u})\mathrm{p}(\varepsilon)$. The co-ordinate system is given by $\mathrm{u} = 1 - \frac{1}{2}(\cos \mathrm{ak}_x + \cos \mathrm{ak}_y)$ and $\mathrm{v} = \frac{1}{2}(\cos \mathrm{ak}_x - \cos \mathrm{ak}_y)$, and the *quadratic* functions of energy, $\mathrm{d}(\varepsilon)$, $\mathrm{s}(\varepsilon) \equiv \frac{1}{\mathrm{S}}$ and $\mathrm{p}(\varepsilon)$ describing the pdσ, spσ and $\sigma\pi$ scattering, respectively. The scattering function $\mathrm{p}(\varepsilon)$ is proportional to t_{zd}^2 and hence to the dimpling angle squared.

We shall now discuss the influence of the scattering functions on the CEC and in particular on the van Hove singularity (VHS) in the density of states (DOS) which is relevant for the van Hove scenario for the high-$\mathrm{T_c}$ cuprates. For flat $\mathrm{CuO_2}$ planes $\mathrm{p} = 0$, and if we, in addition, neglect the coupling $\mathrm{t_{sp}}$ so that $\mathrm{S} = 0$ the resulting CEC of this three orbital pdσ model are simply given by $\mathrm{d}(\varepsilon) = \mathrm{u}$, which are straight lines in u-v space. The CEC in k space are $\Gamma(0,0)$ centered electron pockets if the energy is less than that of the saddle point at $\mathrm{X}(\pi,0)$, $\varepsilon(\mathrm{X})$, and they are $\mathrm{M}(\pi,\pi)$ centered hole pockets if the energy is above $\varepsilon(\mathrm{X})$. This correspond to hole or electron doping away from half filling, respectively. Since the Γ and M centered contours are congruent for the same electron/hole doping we refer to this band shape as symmetric. The corresponding $\mathrm{d}_{x^2-y^2}$-weighted DOS (dDOS) with $\mathrm{s} = 200$ ($\mathrm{S} = 0.005 \simeq 0$) and $\mathrm{p} = 0$ is shown in the upper part of Fig. 29 a. The abscissa is the electron doping in a narrow range around zero, which corresponds to the Fermi level, μ, at the saddle point. The DOS has a sharp symmetric logarithmic VHS. If the coupling to the Cu_s is included, the result is a 4 orbital spdσ model and the term $-\mathrm{v}^2/(\mathrm{u}+\mathrm{s})$ is added to $\mathrm{F}(\varepsilon,\mathrm{k})$. The hybridization with the Cu_s depresses the conduction band near (π, 0) and (0,π) and thereby increases the mass towards Γ and decreases it towards M. The saddle point becomes asymmetric and the CEC now bulge towards Γ. The k-space contours remain closed around Γ for energies below that of the saddle point at X, and closed around M for energies above $\varepsilon(\mathrm{X})$. The dDOS for $\mathrm{s} = 0.6$ ($\mathrm{S} = 1.67$) and $\mathrm{p} = 0$ is shown in the upper part of Fig. 29 b. The VHS from the asymmetric saddle point is logarithmic and

still symmetric. If the planes are dimpled or buckled then hybridization between the σ and the π orbitals is allowed, i.e. $p \neq 0$. If the dimpling exceeds a critical value then the saddle point becomes extended. The dDOS corresponding to an extended saddle point with s = 0.6 (S = 1.67) and p = 0.14 is shown in the upper part of Fig. 29 c.

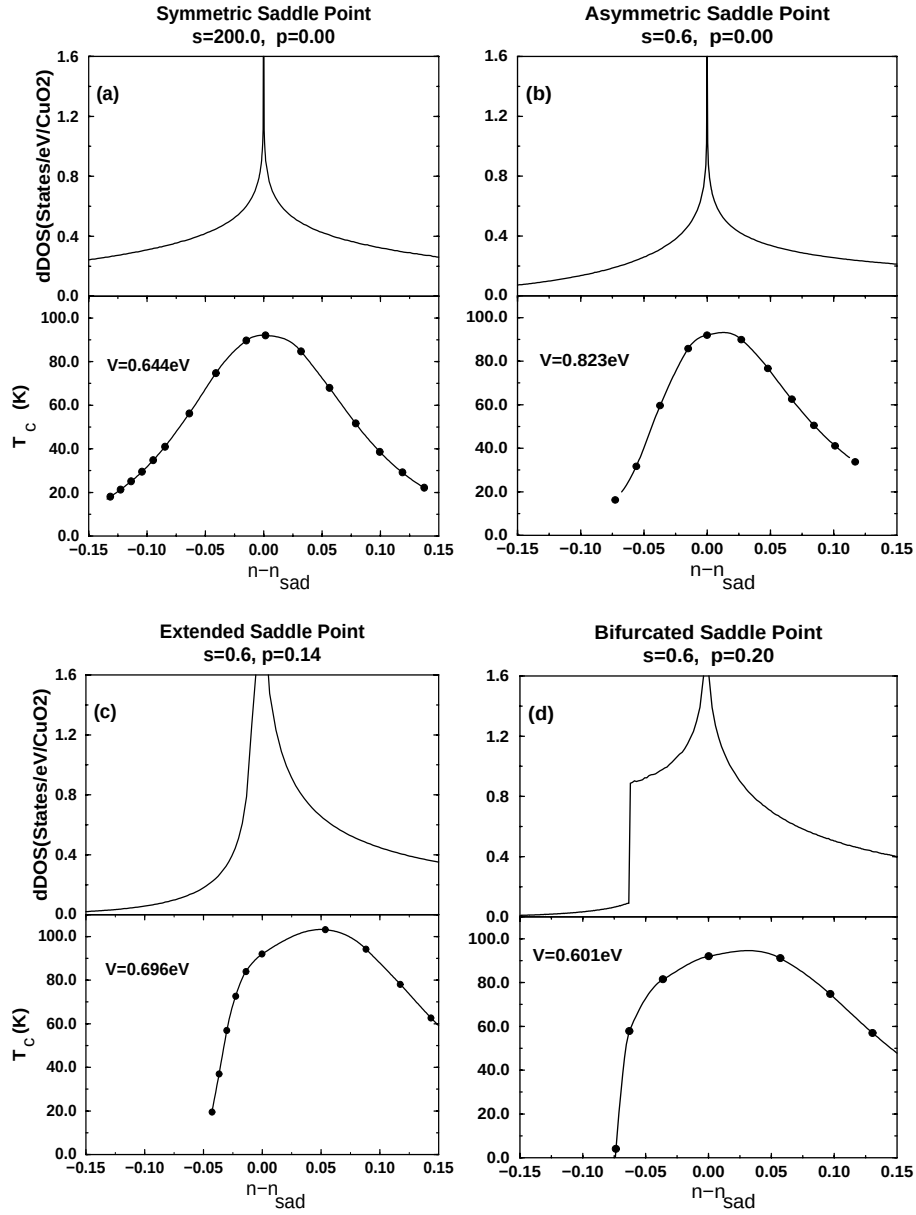

Figure 29: *The $d_{x^2-y^2}$ weighted density of states and doping dependence of the superconducting transition temperature T_c for various van Hove singularity scenarios as described in the text.*

The extended saddle point gives rise to a broad $|\varepsilon|^{-\frac{1}{4}}$ VHS, where the high energy side is about 4 times broader than the low energy side. With increasing dimpling the saddle points become bifurcated to the positions $k_{bi} = ((\pi/a) \pm \Delta k_{bi}, 0)$ and $(0,(\pi/a) \pm \Delta k_{bi})$ and the band structure has local minima at the X and Y points. For energies below the saddle point

and above $\varepsilon(\mathrm{X})$, the Fermi surface has electron pockets around X and Y in addition to the Γ-centered electron sheet. For energies below $\varepsilon(\mathrm{X})$, or above $\varepsilon(\mathrm{k_{bi}})$ the contours are closed around Γ or M, respectively. For $\mathrm{s} = 0.6$ and $\mathrm{p} = 0.20$ the saddle point is bifurcated and the corresponding dDOS is shown in Fig. 29 d. The VHS is again logarithmic and the step appearing at the low energy side is due to the appearance of the electron pockets at X and Y. In order to explore the role of the VHS on the doping dependence of the d-wave superconducting transition temperature $\mathrm{T_c}$, we computed $\mathrm{T_c}$ based on weak coupling theory where the gap equation (5) is given by,

$$\Delta_k = \sum_{k'} V_{k,k'} \frac{\Delta_{k'}}{2E_{k'}} \tanh\left(\frac{E_{k'}}{2T}\right), \tag{5}$$

with $\mathrm{E_k^2} = (\varepsilon(\mathrm{k}) - \mu)^2 + \Delta_\mathrm{k}^2$, for d-wave pairing $\Delta_\mathrm{k} = \Delta \cdot \mathrm{v}$ and we have chosen a phenomenological form for the pair interaction $\mathrm{V_{k,k'}} = \mathrm{V} \cdot \mathrm{v} \cdot \mathrm{v'}$. The value of V is adjusted to give a $\mathrm{T_c}$ of 92K when the doping corresponds to μ at the saddle point. The variation of $\mathrm{T_c}$ with doping is shown in the lower parts of Figs. 29 a to 29 d. The general behavior is the same for all cases considered. Starting from low hole doping, the $\mathrm{T_c}$ increases with hole doping, goes through a broad maximum close to but before the doping level corresponding to the saddle points and then decreases in the overdoped regime. As mentioned above the maximum $\mathrm{T_c}$ is reached on the high energy side of the saddle point, i.e. the Fermi surface is a large M centered hole surface in all cases.

For the extended and bifurcated saddle points the $\mathrm{T_c}$ increases slowly on the underdoped side of the saddle points while it drops abruptly on the overdoped side in agreement with experiments. The reason for this difference is that in the overdoped regime the Fermi surface recedes faster from those k-points which have large v^2-weights.

In conclusion our simple model can explain the doping dependence of superconducting transition temperature observed experimentally within weak-coupling theory.

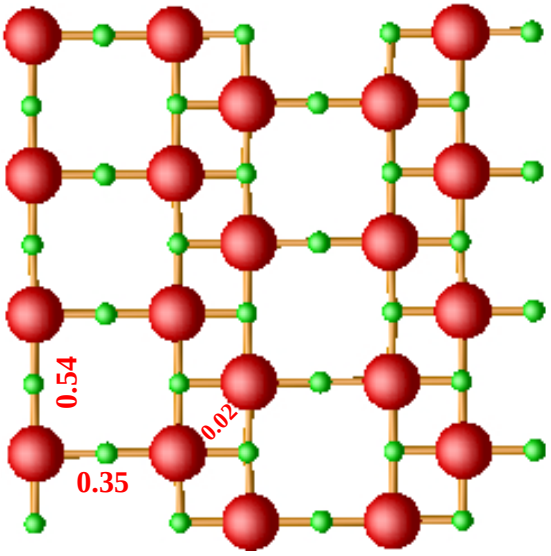

Figure 30: *The Cu_2O_3 ladder plane (Cu is large and red and O is small and green). The nearest neighbor intra- and inter-ladder effective hopping integrals between the Cu atoms shown in the figure are in eV.*

As another application of the downfolding method we have studied the electronic structure of the simplest ladder compound $SrCu_2O_3$. In contrast to the high-T_c cuprates, the key structural element of the ladder compounds is the presence of line defects consisting of CuO double chains which divide the CuO_2 plane into a system of coupled ladders. This is illustrated for a two leg ladder system $SrCu_2O_3$ in Fig. 30. Rice *et al.* suggested that the two leg ladder compound $SrCu_2O_3$ will have a large spin gap and may be superconducting on doping. This prediction led to a serious effort to synthesize cuprates with doped ladders. Very recently superconductivity in the two leg ladder system $Sr_{14-x}Ca_xCu_{24}O_{41}$ have been discovered and these are the first cuprate superconductors without the CuO_2 planes.

We have employed the downfolding technique to calculate the hopping integrals of an effective tight-binding model for $SrCu_2O_3$. The crucial antibonding band of the single CuO_2 plane is broken into two rung bands for the two leg ladder system. We find that the full LDA band structure of $SrCu_2O_3$ close to the Fermi level can be reproduced very well by this effective 2-band Cu-Cu model with intra- as well as inter-ladder interactions. The important hopping parameters of the effective ladder model are shown in Fig. 30. The inter-ladder hopping is very small compared to the intra-ladder hopping. We also find a strong anisotropy between the $t_\perp$ (= 0.35 eV) and $t_\parallel$ (= 0.54 eV) intra-ladder hoppings. This anisotropic intra-ladder hopping is consistent with the anisotropic antiferromagnetic coupling constant seen in numerical analysis of susceptibility data as well as neutron scattering results.

(O.K. Andersen, C. Arcangeli, I. Dasgupta, O. Jepsen, T. Saha-Dasgupta and R.W. Tank)

Growth of $Hg_{1-x}Re_xBa_2Ca_{n-1}Cu_nO_{2n+2+\delta}$ single crystals from a flux in self-atmosphere

The Hg-based superconductors $HgBa_2Ca_{n-1}Cu_nO_{2n+2+\delta}$, with n = 3 and n = 2 exhibit extremely high transition temperatures of 130 K and 120 K, respectively. The synthesis of the cuprates, however, is accompanied with considerable difficulties because of the high decomposition pressure and toxicity of HgO. With the addition of ReO_2 the high decomposition pressure was sufficiently reduced so that the particular cuprates could be crystallized from a self-component solution in a closed capsule of fused silica.

The composition of the starting mixtures are summarized in Table 2. The preparation of the solution materials consists of two steps. First, mixtures (usually 3 g) of $BaCO_3$, $CaCO_3$, and CuO are ground in a ball mill, transferred into an alumina crucible after 4 hours and heated for two days in air at 880°C. From the calcined product pellets are formed and fired at 920°C in flowing oxygen for two days. Secondly, the sintered pellets are ground together with HgO and ReO_2 in well ventilated facilities. The ground mixtures are loaded into a cylindrical Al_2O_3 crucible of 1 cm in diameter and 70 cm in length. The crucible is placed in a quartz glass ampoule which is evacuated and sealed off at $\approx 10^{-3}$ bar.

While the addition of Re reduced the decomposition of HgO, it partly substitutes Hg to yield the compound $Hg_{1-x}Re_xBa_2Ca_{n-1}Cu_nO_{2n+2+\delta}$. This compound is chemically rather stable. It can be crystallized by the self-component flux method as known from $YBa_2Cu_3O_{7-\delta}$. Only a low Hg vapor pressure is needed to avoid the decomposition of the cuprate. This Hg pressure is obtained by the Hg self-atmosphere when the solution is enclosed in a sealed capsule. For, e.g. 3 g source material the necessary free volume of the ampoule has to be less than 10 cm^3. Starting with the soaking temperatures given in Table 2 the solutions are first slowly ($\approx 1°C/h$) cooled to 950°C and than fast to room temperature.

Table 2. *Parameters used for the growth of* $Hg_{1-x}Re_xBa_2Ca_{n-1}Cu_nO_{2n+2+\delta}$ *single crystals from solution.*

n	Starting cation ratio (at%) HgO	ReO_2	BaO	CaO	CuO	Crystal formula	Soaking temp.(°C)	Growth time (h)
2	19.70–12.00	0.30–8.00	40.00	10.00	30.00	$Hg_{1-x}Re_xBa_2CaCu_2O_{6+\delta}$ (x∼0.02–0.25)	1005–1020	55–70
3	16.42–10.00	0.25–6.67	33.33	16.67	33.33	$Hg_{1-x}Re_xBa_2Ca_2Cu_3O_{8+\delta}$ (x∼0.02-0.25)	1005–1020	55–70

Clusters of black and shiny plate-like crystals of $Hg_{0.97}Re_{0.03}Ba_2Ca_2Cu_3O_{8+\delta}$ were found to grow at the bottom of the crucible, as shown in Fig. 31. The upper part of the crucible contained a multiphase ceramic wrapped into a layer of a brick-red matrix identified to be HgO. The solidified melts contained internal and surface cavities. Platelet crystals appeared from inside of these cavities into the solidified solution and were often firmly embedded in a solidified matrix, making removal difficult without damage. In particular, $Hg_{0.9}Re_{0.1}Ba_2Ca_2Cu_3O_{8+\delta}$ crystals measuring up to $3 \times 3 \times 0.15\,mm^3$ were found in the cavities.

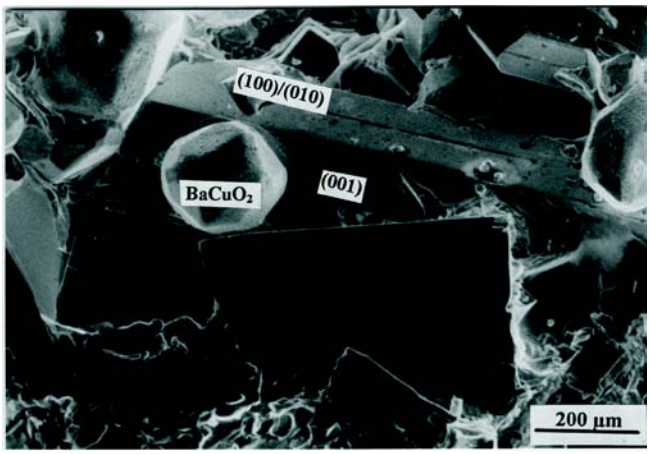

Figure 31: *Single crystals of* $Hg_{0.97}Re_{0.03}Ba_2Ca_2Cu_3O_{8+\delta}$ *clustering on the bottom of the crucible.*

The $Hg_{1-x}Re_xBa_2Ca_{n-1}Cu_nO_{2n+2+\delta}$ crystals appeared with the three basic faces (001), (100) and (010) as seen in Fig. 31. For $x = 0.07$, $n = 3$ and $x = 0.10$, $n = 2$ the structures were determined to be tetragonal with $a = 3.8634$ Å, $c = 12.7723$ Å and $a = 3.8531$ Å,

c = 15.6677 Å, respectively. No twin boundaries could be found by TEM investigation. A dark-field image, g = [200], taken under the two beam condition is shown in Fig. 32. This image exhibits a tweed-like contrast which provides evidence for a possible tweed tetragonal structure phase in the present samples.

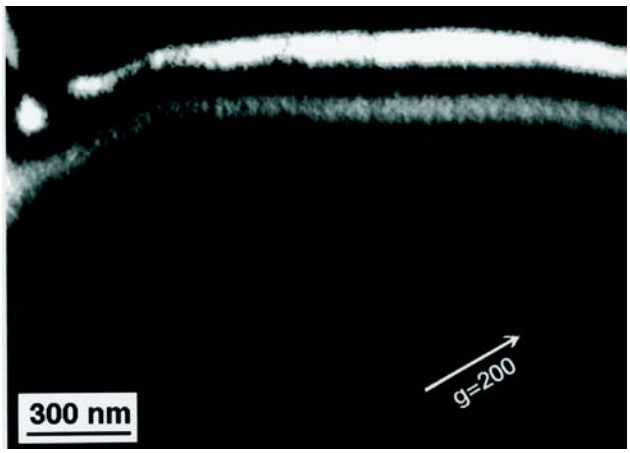

Figure 32: *Tweed-like structure of CBED patterns of a* $Hg_{0.97}Re_{0.03}Ba_2Ca_2Cu_3O_{8+\delta}$ *crystal. A dark-field image g=*[*200*].

Small precipitates of $Hg_{1-x}Re_xBa_2Ca_{n-1}Cu_nO_{2n+2+\delta}$ are formed at the growth steps within the fast cooling period from 950°C to room temperature. A typical example with an as-grown decorated (001) is shown in Fig. 33. The surface contains high and low macro-steps whose widths have been estimated by optical microscopy to be $\approx 50\,\mu$m and $\approx 8\,\mu$m, respectively. The crystal surface between either high or low macro-steps is composed of micro-steps whose height is too low to be measured by conventional optical microscopy. It is assumed that the macro-steps form by bunching of the micro-steps when the growth of the (001) faces proceeds layer by layer. Presumably the steps arose from screw dislocations.

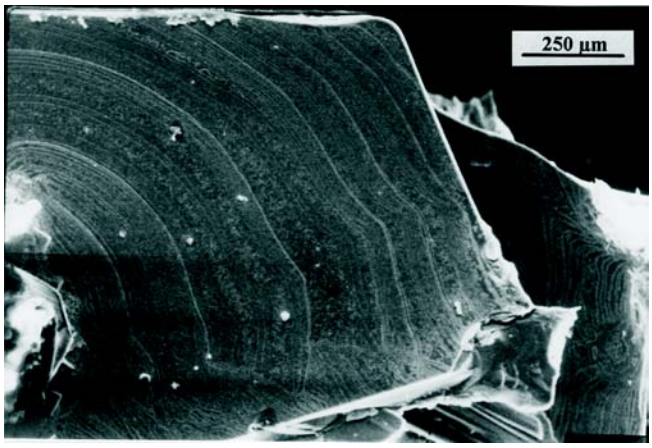

Figure 33: *Decorated (001) surface of a* $Hg_{0.97}Re_{0.03}Ba_2Ca_2Cu_3O_{8+\delta}$ *single crystal.*

A particular smooth decorated (001) surface is shown in Fig. 34. The $Hg_{1-x}Re_xBa_2Ca_{n-1}Cu_nO_{2n+2+\delta}$ precipitates are aligned along a spiral. Thus it is assumed that the crystal was growing through a single screw dislocation. Similar growth spirals have been observed on single crystals of $YBa_2Cu_3O_{7-\delta}$.

Figure 34: *Single crystals of $Hg_{0.9}Re_{0.1}Ba_2Ca_2Cu_3O_{8+\delta}$ isolated from the flux and showing a decorated spiral on (001) surface.*

In addition, in some crystal faces a few tiny cavities filled with droplets of Hg are observed by optical microscopy. It is assumed that they are caused by the decomposition of $Hg_{1-x}Re_xBa_2Ca_{n-1}Cu_nO_{2n+2+\delta}$ if the ambient Hg vapor pressure is not sufficiently high. When the amount of ReO_2 was too low a few small droplets of mercury were found in the upper cold part of the crucible or the inner quartz ampoule. By measuring the change of weight between the starting mixtures loaded into the crucible and solidified compound after growth, a loss of Hg was found which ranged from nearly zero to 12 wt% when the Re content was lowered from 11wt% to 1wt%, i.e. Y/(wt% Hg) = 12.97–2.12X/(wt% Re) + $0.09/X^2$(wt%Re)^2.

The DC-susceptibility of as-grown and annealed single crystals was measured as a function of the temperature with a SQUID magnetometer. The onset temperatures T_c of the as-grown $Hg_{0.97}Re_{0.03}$ $Ba_2Ca_2Cu_3O_{8+\delta}$ and $Hg_{0.9}Re_{0.1}Ba_2CaCu_2O_{6+\delta}$ crystals, was found to be 130 K, while the width of the transition was $\Delta T \approx 20$ K and ≈ 22 K, respectively. Annealing at 300°C in flowing oxygen gas of one atmosphere increased T_c to 132 K for the n = 3 and to 122 K for the n = 2 samples, i.e. $\Delta T \approx 2$ K for both compounds. Since 300°C is considered to be too low for cations to significantly move and induce changes in the structure, it is likely that the annealing treatment changes only the oxygen content in the superconducting phase. This implies that the superconducting phase in the as-grown crystals was in a slightly underdoped state. The oxygen deficiency of the crystals can also be traced to the fact that the cooling time after growth was too fast (1 hour).

(C.T. Lin and E. Schönherr)

Magnetic penetration depth in the new layered carbide halide superconductors $YY_2C_2X_2$ (X = Br, I) determined by muon-spin rotation experiments

Since the discovery of superconductivity in the rare-earth carbide halides $RE_2C_2X_2$ (RE = Y, La; X = Cl, Br, I) some work has been devoted to an understanding of their superconducting properties. Extensive experiments on the $Y_2C_2X_2$ system have revealed a number of characteristic details: For example, it has been demonstrated that by a proper adjustment of x in samples $Y_2C_2(Br_{2-x}I_x)$ the superconducting transition temperature can be raised to 11.6 K. An increase of the transition temperature of $Y_2C_2Br_2$ by 1.2 K has also been achieved by an intercalation of Na atoms into the van der Waals coupled doublelayers of halogen atoms. By a careful comparison with the superconducting properties of the dicarbide YC_2, which crystallizes in a three-dimensionally connected crystal structure (CaC_2 structure-type), it has been shown that the pronounced crystalline anisotropy in the layered yttrium carbide halides leads to a significant increase of the electron-phonon coupling strength. As a consequence of the anisotropy (e.g. anisotropy ratio $\gamma = 5.2 \pm 0.2$ for $Y_2C_2I_2$) the upper critical fields in the layered yttrium carbide halides are enlarged by almost two orders of magnitude as compared to YC_2. A clear $^{12}C/^{13}C$ isotope effect has been detected in YC_2. In contrast, there is no indication of a decrease of T_c when istope enriched ^{13}C is substituted, e.g. in $Y_2C_2Br_2$. Deviations from a simple Korringa law seen in the ^{13}C NMR relaxtion rate of $Y_2^{13}C_2X_2$ (X = Br, I) evidence a structured electronic density of states close to the Fermi energy arising from electronic bands of low dispersion.

While the upper critical fields B_{c2} could be very well extracted from investigations of the high-field magnetization data, a determination of the lower critical fields B_{c1} and the related London peneration depth $\lambda(0)$ from magnetization measurements is notoriously difficult. On the other hand, the London penetration depth contains important information about the superconducting state and is therefore an essential parameter to characterize a superconductor: For an isotropic superconductor in the clean limit the London penetration depth is related to the density of superfluid pairs at zero temperature $n_S(0)$ and the effective mass of the superconducting pairs m^* via the simple relation

$$1/\lambda^2(0) = \mu_0 e^2 n_S(0)/m^* . \qquad (6)$$

To determine the London penetration depth of $Y_2C_2X_2$ and YC_2 more precisely we performed muon-spin-rotation (μ^+SR) measurements at the Paul Scherrer Institut (Switzerland) in a temperature range from T_c to 0.1 K. The external magnetic field was applied perpendicular to the muon polarization direction. In the μ^+SR-technique, highly spin-polarized positive muons are deposited in the sample which itself is exposed to an external magnetic field kept within the London-limit ($B_{c1} \ll B_{ext} \ll B_{c2}$). Once come to rest at interstitial sites in the samples, the muons start to perform a Larmor precession in their local magnetic field. The time-resolved spin polarization of the muons is determined via the parity violation in the muon decay in which two neutrinos and a positron are generated. The positron is preferentially emitted into the direction of the muon spin.

The positron emission rate thus contains information about the Larmor precession and the depolarization of the muons. Via its Fourier transform the distribution of internal magnetic fields, ΔB, can be calculated. In a type-II superconductor ΔB is directly related to the penetration depth:

$$\langle \Delta B^2 \rangle \propto \Phi_0^2 / \lambda_{ab}^4 \tag{7}$$

From the muon-spin depolarization rates $\sigma(T)$ measured on polycrystalline samples of $Y_2C_2X_2$ and YC_2 we were able to extract the London penetration depths in a polycrystalline average with high accuracy (Table 3).

Table 3. *Critical temperatures* T_c*, depolarization rate* $\sigma(0)$*, and absolute values for the London penetration depth* $\lambda_{poly}(T \to 0)$ *of the investigated compounds.*

compound	T_c [K]	$\sigma(0)$ [μs^{-1}]	$\lambda_{poly}(0)$ [nm]
YC_2	3.85	1.25±0.03	246±4
$Y_2C_2Br_2$	5.05	0.35±0.02	554±5
$Y_2C_2I_2$	9.97	1.07±0.02	317±3

Taking into account the anisotropy ratio of $\gamma = 5.2 \pm 0.2$ for $Y_2C_2I_2$ we determined the in-plane and out-of-plane penetration depths λ_{ab} and λ_c that amount to 257 ± 3 nm and 1645 ± 10 nm, respectively. In Fig. 35 $\lambda(T)$-data are compared to the predictions of the BCS weak coupling theory and the two fluid (2FL) model. The results are in qualitative agreement with the analysis of the specific heat jump at T_c: Data taken on YC_2 pass along the BCS weak coupling curve, while $Y_2C_2I_2$-data are shifted towards the 2FL model indicating an enhanced electron-phonon coupling.

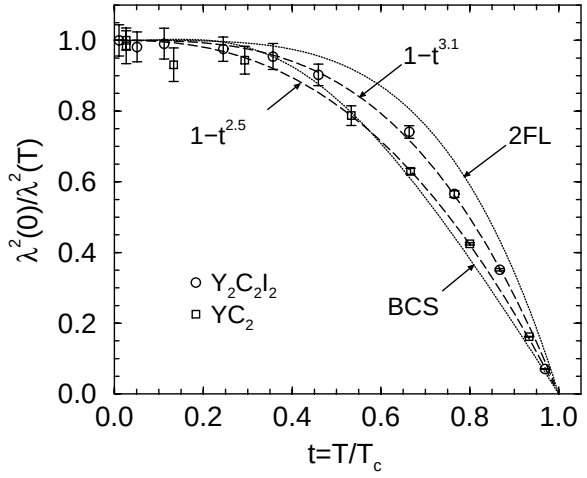

Figure 35: *Fits of the temperature dependence of the London penetration depth of* YC_2 *(squares) and* $Y_2C_2I_2$ *(circles) by a power law 1-*$(T/T_c)^p$ *(dashed lines). The temperature dependence expected for the weak-coupling BCS model and the two-fluid (2FL) model are indicated by the full lines.*

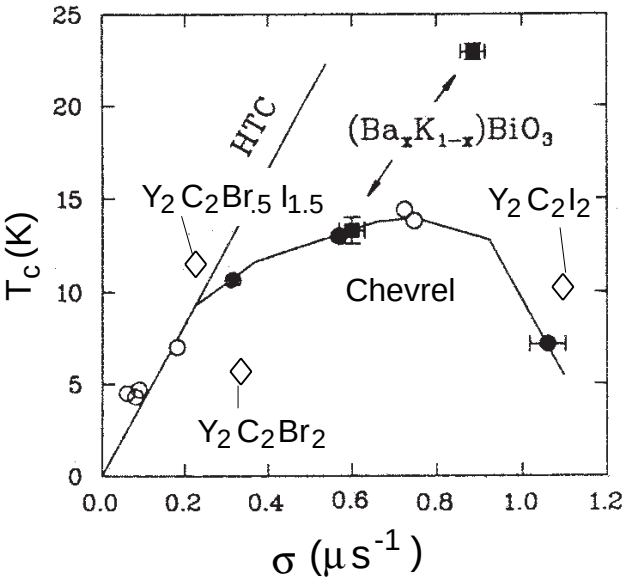

Figure 36: *Superconducting transition temperature T_c versus relaxation rate σ ($T \to 0$) ('Uemura-plot'). In the Uemura-plot $Y_2C_2X_2$ fall in a region close to the Chevrel-phases.*

In Fig. 36 the superconducting transition temperatures are plotted as a function of the μ^+SR depolarization rate at zero temperature ('Uemura-plot'). The results for $Y_2C_2Br_2$ and $Y_2C_2Br_{0.5}I_{1.5}$ lie close to the so-called Uemura-line for the underdoped high-T_c systems while $Y_2C_2I_2$ deviates to higher $\sigma(0)$ values as has been found for the overdoped high-T_c systems.

Judging from their position in the Uemura-plot, the $Y_2C_2(Br,I)_2$ compounds appear to be similar to the Chevrel-phases.

(R.W. Henn, Th. Gulden, Ch. Bernhard, R.K. Kremer and A. Simon; Ch. Niedermayer and Th. Blasius (Universität Konstanz))

Point-contact study of superconducting RNi_2B_2C compounds

The recently discovered intermetallic compounds, the nickel boro-carbides RNi_2B_2C (R = rare earth, Y), show an interesting interplay between superconductivity and magnetism with relatively high superconducting and magnetic critical temperatures. Besides the co-existence of both antiferromagnetism and superconductivity at the lowest temperatures, some of these compounds show re-entrant behavior to the normal state below the superconducting critical temperature. We have investigated the current-voltage characteristics of small metallic point contacts with these materials in order to get information on the order parameter in the superconducting state and on the scattering of the charge carriers with quasiparticle excitations, e.g. the electron-phonon interaction in the normal state.

For the normal-metal–superconductor contacts of the RNi_2B_2C compounds against a Ag-needle, the study of the Andreev-reflection process for the electrical transport across the interface yields direct access to the superconducting order parameter. In the inset of Fig. 37 we have plotted the variation of differential resistance dV/dI normalized with respect to the normal state of a $Ag-HoNi_2B_2C$ contact with the characteristic double-minimum gap structure related to the Andreev-reflection process. The Andreev-reflection spectrum can be described by the Blonder-Tinkham-Klapwijk model for a BCS superconductor which yields the superconducting order parameter. In Fig. 37 we have given the order parameter Δ as a function of the critical temperature T_c for different compounds. The dashed line shows the ratio $2\Delta/k_BT_c = 3.7$ which points to a moderate electron-phonon coupling upon comparing to the weak-coupling BCS value 3.5.

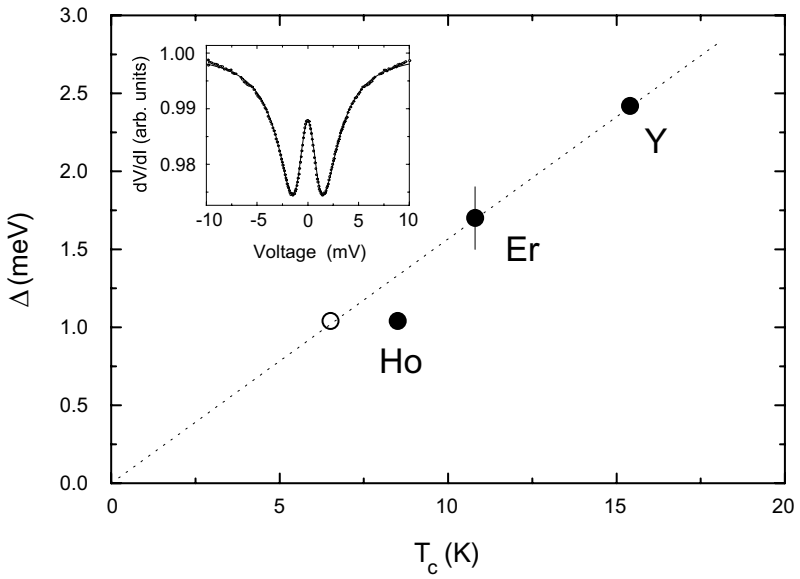

Figure 37: *The order parameter Δ as a function of the critical temperature T_c for Ho-, Er-, and YNi_2B_2C. The open symbol is for the Ho-compound with T_c^*=6.5K. The inset shows the dV/dI-data for a $Ag–HoNi_2B_2C$ point contact with the full curve for the Blonder-Tinkham-Klapwijk model of the Andreev-reflection double-minimum structure.*

In the temperature dependence of the point-contact spectra of the Ho-compound an anomalous behavior has been observed. Although the superconductivity sets in below $T_c = 8.5$ K, a well pronounced Andreev-reflection structure occurs only below $T_c^* \simeq 6.5$ K. The temperature dependence of the BCS spectra at low temperatures can be extrapolated to the same critical temperature T_c^*. Between T_c^* and T_c the spectra reveal broadened structures which could be the signature of a gapless superconducting state in this temperature region. Taking $T_c^* = 6.5$ K for the order parameter data in Fig. 37 gives a superconducting coupling strength which is comparable to the other investigated compounds. The gapless superconducting state points to pair breaking and coincides with the existence of an incommensurate spiral magnetic order of the Ho-ions. Below the Néel temperature $T_N \simeq 5$ K the antiferromagnetic order compensates the magnetic moments on the scale of the coherence length allowing the coexistence with a BCS superconducting state.

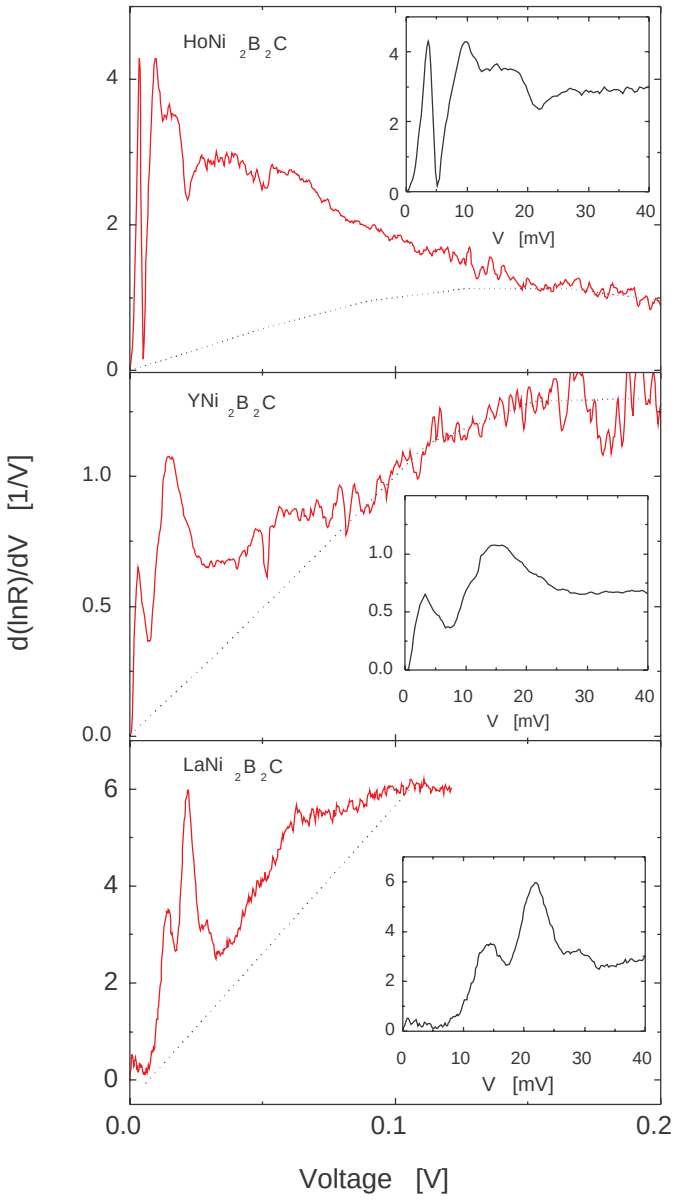

Figure 38: *The second derivative spectra d(lnR)/dV of point-contacts with different nickel-boride compounds in the normal state showing the absence of a soft phonon mode around 4meV in the nonsuperconducting La compound.*
$HoNi_2B_2C$: (B||c)=0.5T,
YNi_2B_2C: (B⊥c)=7T and
$LaNi_2B_2C$: B=0T.

By the application of a magnetic field B we have studied the contacts in the normal state. The point-contact spectra reveal reproducible structures in the second derivatives of the current-voltage characteristics. Figure 38 shows examples of the point-contact spectra $\mathrm{d}(\ln \mathrm{R})/\mathrm{dV}$ for different compounds. From experiments on ballistic point contacts in pure metals it is known that these measurements allow a direct energy-resolved spectroscopic investigation of the inelastic scattering of electrons. The second derivative gives direct access to the spectral function $\alpha^2\,\mathrm{F}$ for the electron interaction. The point-contact spectrum of $HoNi_2B_2C$ exhibits strong peaks at about 4 meV and 9 meV corresponding to the maxima of soft phonon density of states expected from the dispersion curves observed in $LuNi_2B_2C$. There is also an essential spectral intensity between 15 meV and 19 meV coinciding with a flattening of the phonon dispersion curves. The spectrum of YNi_2B_2C also

reveals a soft phonon peak at the same energy (4 meV). However, the compound $LaNi_2B_2C$ does not exhibit 4 meV and 9 meV soft phonon modes. The observation of these features in the electron-phonon interaction of the superconducting compounds, unlike the non-superconducting $LaNi_2B_2C$, could be connected with differences in the electronic structure between members of the same homological row. In this respect one should note that inelastic neutron scattering reveals phonon softening of the low-energy phonon branches in the non-magnetic Lu compound at about the same wave vector at which an incommensurate spiral structure occurs in the magnetic isostructural compounds. Moreover, theoretical calculations show that there is essential Fermi surface nesting at this particular wave vector.

The contacts with $HoNi_2B_2C$ showed very often a suppression of the low-energy phonon structures by an applied magnetic field B in the (a,b)-plane, but not for B $\|$ c. Usually, a magnetic field has no influence on the phonon density of states and on the electron-phonon coupling. For the field oriented in the (a,b)-plane, the magnetic order is destroyed at about 1–2 T. For higher fields the intensity of the phonon structures is hardly influenced by a magnetic field. Therefore, from our data one can conclude that there exists an interaction between the phonon and magnon branches of the excitation spectra in $HoNi_2B_2C$, which enhances the electron-phonon interaction with the soft phonon modes in $HoNi_2B_2C$, and which is suppressed by magnetic fields that destroy the magnetic order. Interestingly, in the nominally non-magnetic compound YNi_2B_2C a magnetic field was also found to influence the intensity of the low-energy phonon peaks which would point to the existence of magnetic interactions in this compound.

The point-contact investigations of the interaction between the different quasi particles (electrons, phonons, and magnons) point to a possible strong interaction between magnetic and vibrational degrees of freedom in these magnetically ordered superconductors, which would determine self consistently the resulting Cooper pairing of the electronic quasi-particles in the superconducting state.

(V.V. Fisun, L.F. Rybaltchenko, I.K. Yanson, A.G.M. Jansen and P. Wyder)

Molecular dynamics in low-spin excited states

Photochemical reactions, i.e. reactions that are induced by the absorption of photons, are important in many processes in chemistry and biochemistry. While the experimental investigation of light-induced dynamical phenomena on a microscopic scale has made great progress in the past few years due to new developments in laser chemistry, the theoretical means to investigate the dynamics in excited states remain limited in scope. In contrast, the study of ground state reactions has received a big boost from the development of first-principles molecular dynamics based on density functional theory (DFT) in the Kohn–Sham formalism. Of course, it would be extremely useful to extend this method to the study of photochemical reactions. The most important types of organic photoreactions are those that take place in the first excited singlet state (S_1) or in the lowest triplet state (T_1), other energy levels being in general too short-lived to be of interest. Since the T_1 state is the lowest state with triplet spin symmetry, standard Kohn–Sham theory can be used to explore the corresponding potential energy surface. However, S_1 reactions are not amenable to the ground state theory.

When performing molecular dynamics (MD) simulations it is of primary importance to keep the computational effort to a minimum and this excludes the use of correlated quantum chemical methods. It was the scope of our work to develop a simple approximate scheme that allows excited singlet states to be treated in a Kohn–Sham-like fashion. We use one spin-adapted function to represent the wavefunction and derive a self-consistent scheme using the Kohn–Sham approximation for the exchange-correlation part of the energy. Our approach allows stable molecular dynamics simulations to be conducted in the S_1 state in analogy to the well-established first-principles MD on the S_0 Born–Oppenheimer surface.

We assume that the excitation can be described by a pure HOMO–LUMO excitation, that is a transition of a single electron from the highest doubly occupied orbital to the lowest non-occupied orbital. By starting from a single-determinant picture and constructing spin-adapted functions we arrive at the following functional whose minimum is postulated to yield the energy of the first excited singlet state S_1:

$$\mathcal{H}[\{\psi_i(\mathbf{r})\}] = 2\langle m|\hat{H}|m\rangle - \langle t|\hat{H}|t\rangle - \sum_{i,j=1}^{n+1} \epsilon_{ij}\left(\int \psi_i^*(\mathbf{r})\psi_j(\mathbf{r})d\mathbf{r} - \delta_{ij}\right) \qquad (8)$$
$$i = 1,\cdots,n+1; j = 1,\cdots,n+1$$

Here, m and t functions are the wavefunctions that are obtained by occupying two orbitals with a single electron only, whereby the two electrons have opposite or equal spin respectively. $\hat{H}_m$ and $\hat{H}_t$ are the Hamilton operators for these two states. By minimization of the functional, a set of Schrödinger-like equations with state dependent self-consistent effective potential is obtained. With this scheme, MD runs can be performed in the first excited singlet state. We do this by optimizing the molecular orbitals after each MD step.

First calculations have been performed for seven small aldehydes, ketones, amides, and imines. All the investigated compounds contain hetero double bonds (C=O, C=N) which are among the most important photosensitive groups in organic chemistry. The lowest electronic excitation in these systems is an n $\rightarrow \pi^*$ transition: One of the lone-pair electrons is transferred to an antibonding orbital of the π system. These transitions are usually quite pure HOMO–LUMO transitions, thus our method is expected to work best for them.

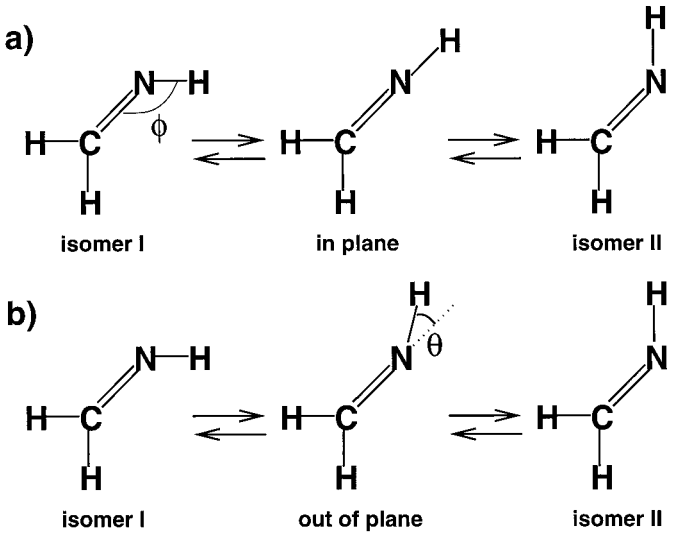

Figure 39: *The two possible pathways for the photoisomerization of formaldimine. a) in-plane mechanism, b) out-of-plane mechanism.*

The bond geometries are obtained with an accuracy that corresponds to that of ground state calculations; the performance of the method in this respect is clearly sufficient for the use in molecular dynamics runs. The calculated excitation energies are smaller than the experimental data by an average value of 0.4 eV. Since the energy shift is essentially constant for the vertical and adiabatic excitation energies of the compounds investigated, it can be concluded that the shape of the potential energy surfaces is not greatly affected and the resulting molecular dynamics is reasonably accurate.

As a small test case for excited state molecular dynamics we have investigated the photoisomerization of imines. This type of reaction has been investigated for many systems. With NMR techniques it could be proven that symmetrically substituted imines (R'=R") also undergo this isomerization upon excitation. In this case the two isomers are chemically identical. The excited states of some of the smallest imines have been investigated with ab-initio methods. In particular, the potential energy surface for the photoreaction of formaldimine (R=R'=R"=H) has been studied in detail. Two different reaction pathways are discussed in literature: The first pathway involves a linear arrangement of the carbon atom, the nitrogen atom and the moving hydrogen atom; the isomerization occurs in-plane. The second pathway represents an out-of-plane mechanism; the hydrogen atom moves out of the plane formed by the other atoms. Multi-Reference Configuration Interaction (MRD–CI) results show clearly that the out-of-plane mechanism is strongly favored; the linear arrangement is less stable than the bent geometry by roughly 0.9 eV.

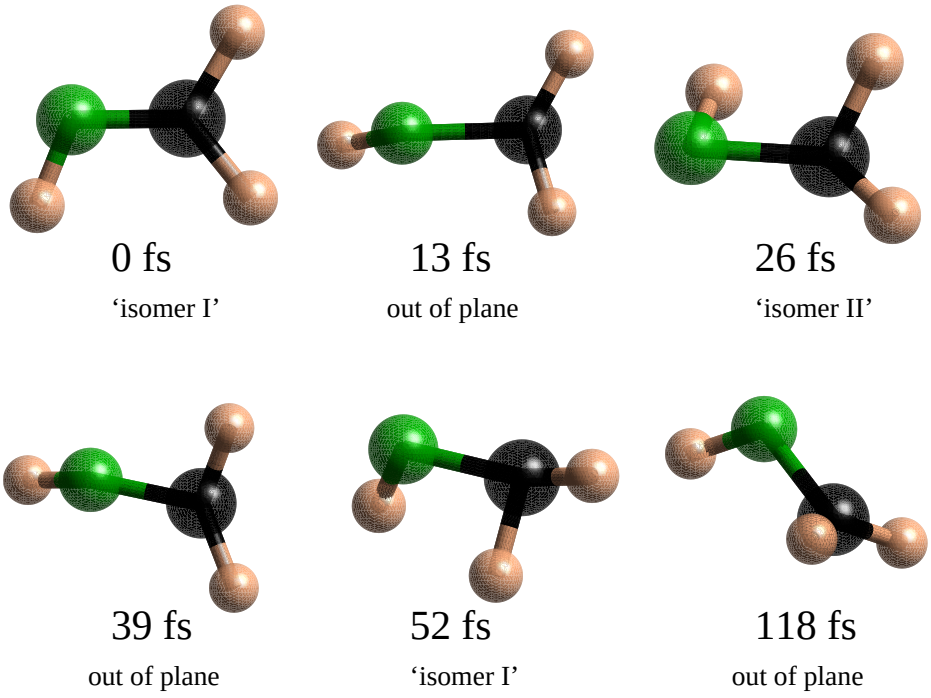

Figure 40: *Snapshots of the molecular dynamics simulation of the formaldimine isomerization in the first excited singlet state. The configurations observed at t=26fs and t=52fs, which are termed 'isomer I' and 'isomer II' respectively, correspond to excited-state geometries that are close to one or the other of the two ground state minima.*

We have performed a molecular dynamics run starting from the optimized ground state geometry of formaldimine. Initially the atoms were propagated on the ground state surface roughly at room temperature (310 ± 30 K) for about 0.5 ps. At a certain point during this simulation ($t = 0$) we changed the occupation and switched to our excited state formalism. This corresponds to simulating an instantaneous vertical transition to the first excited state. We find that the imine hydrogen atom starts to move out of the molecular plane immediately after the excitation. On a timescale of 10 fs, the kinetic energy rises by about 1600 K. We find that the out-of-plane arrangement is lower in energy than the linear in-plane geometry by 1.0 eV, which is in good agreement with the MRD–CI calculations (0.9 eV). However, in contrast to the MRD–CI potential energy surface calculations, where only the motion of the H-atom was considered our calculations include all internal degrees of freedom. Our results show that the whole structure is involved in the photoreaction, and not only the hydrogen atom.

In the future we hope to develop this method so that photochemichal reactions can be studied with an efficiency and accuracy comparable to that of ground state first-principles MD calculations.

(I. Frank, J. Hutter and M. Parrinello)

First principles molecular dynamics study of Ziegler–Natta heterogeneous catalysis

The Ziegler–Natta catalysis based on titanium chlorides plays a special role in the polymerization of α-olefins with a high degree of stereoselectivity. The problem of the nature of the active centers and their ability in producing isotactic polymers is a major motivation for the intensive experimental and theoretical investigations. In particular, theoretical approaches can provide all the informations that, due to the peculiar nature of these extremely fast reactions, are not directly accessible to experiments. Their aim is to supply the basic understanding necessary to improve the industrial applications.

In our study, we investigated via Car–Parrinello Molecular Dynamics the Ziegler–Natta $MgCl_2$ supported catalysis of olefins. We adopted a Becke–Lee–Yang–Parr gradient-corrected density functional (BLYP) and performed CPMD simulations at constant temperature using a system containing 24 formula units of the $MgCl_2$ substrate and one active Ti(IV) center. The temperature parameter was set to 323 K, according to experiments. Trouiller and Martins norm-conserving pseudopotentials including non-linear core corrections for Mg and Ti accounted for the valence-core interactions. In the first part of the project, we focused on Ti active sites on the (110) surface of the $MgCl_2$ support, analyzing the main catalyst models reported in the literature, namely the 6-fold Corradini centers, and investigating possible alternative configurations in an unbiased way, by simulating $TiCl_4$ deposition on the substrate. In this way we could identify a new 5-fold configuration of the catalyst as a results of a spontaneous reaction of the substrate with the $TiCl_4$ molecule. The activation of the catalytic centers is achieved by replacing a Cl atom of a Ti(IV) site with a methyl unit acting as chain terminator.

Simulations of the insertion of ethylene in the metal-carbon bond of the active centers has allowed to depict the reaction pathway leading to the formation of the polymer and to compare the reactivities of the different Ti configurations. By means of constrained first principles molecular dynamics we then determined the free energy profiles and estimated activation barriers in the alkene insertion processes. A subsequent study of the insertion of a second ethylene has given an interesting insight into the chain growth process providing a complete picture of the reaction mechanism. As far as the energetics is concerned, we found that in case of ethylene a barrier of about 12.7 kcal/mol characterizes the primary insertion in the Corradini center, while the 5-fold active site turns out to be more reactive, with a barrier of only 6.7 kcal/mol and an energy gain of 23.3 kcal/mol for the final product. These results are in good agreement with available experimental data concerning activation energies and experimental overall enthalphy for ethylene insertion (22.2 kcal/mol). The alkyl chain formation is α-agostic assisted during the first insertion and β-agostic for the subsequent olefin addition, a fact that reduces the steric hindrance among the hydrogens of the already formed polymer and the ones carried by the approaching ethylene. The chain grows more or less parallel to the surface of the support and all the ethylene insertions occur from the same side. This fixes univocally the reaction pathway.

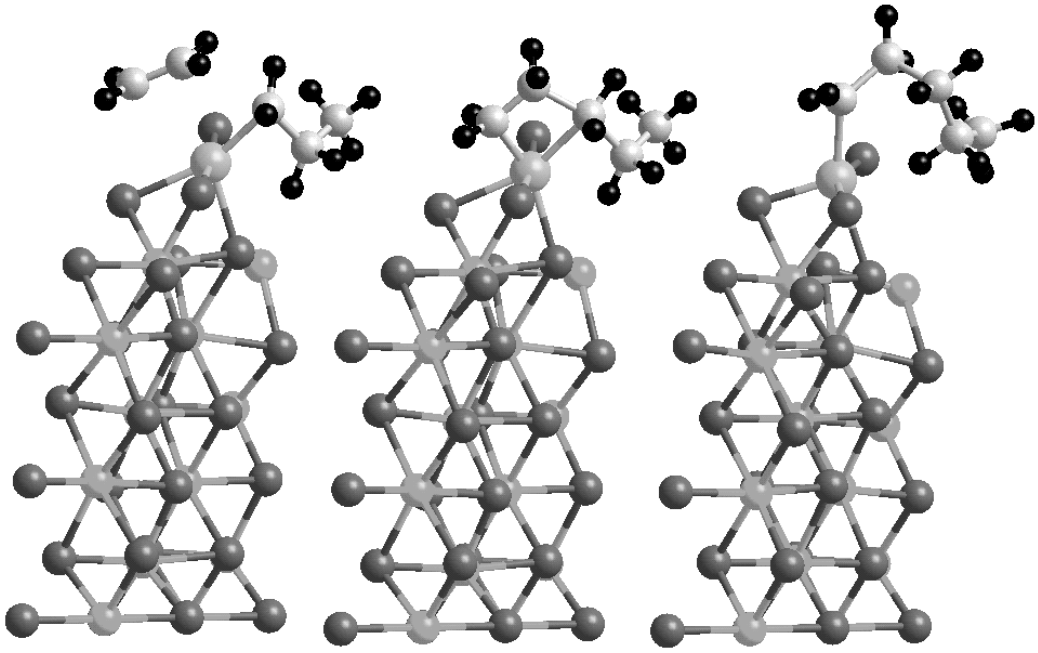

Figure 41: *Polyethylene chain growth process. From the left to the right are shown the π-complex, the transition state and the final product.*

In Fig. 41 the main phases of the alkyl chain growth, i.e. the complexation, the transition state and the final product, are illustrated by snapshots as obtained from our simulations. Some preliminary results about the polymerization of propene, as a further extension of our study, have supplied a first attempt to address the problem of the stereoselectivity. In this case, we used the same 5-fold active center discussed above. As in the example of the ethylene, the reactions proceed via the complexation, the formation of a four-membered ring, representing the transition state, and the final product, i.e. the completely inserted olefin. For the propene, the polymerization is α-agostic assisted and the stereoselectivity results as a natural consequence of the geometrical environment. In fact, because of steric repulsions of the propene with the substrate or the already formed chain, only one orientation is allowed and all the others forbidden, in the sense that unconstrained dynamics as well as attempts to optimize the geometries gave no stable π-complexes. In the specific case of the 5-fold site, all the forbidden orientations are the non-isotactic ones. Thus the stereoregularity is ensured at each step of the polypropylene formation. The complex stabilization occurs with a reorientation of the formed chain which displaces along the substrate in a way very similar to the one observed in the case of ethylene. This rules out a possible *alternating* mechanism which could give rise to syndiotactic chains.

To conclude, we got a comprehensive insight into the fundamental problems of this class of catalytic reactions at a fully *ab-initio* level.

(M. Boero and M. Parrinello)

Magnetic and orbital order in cuprates and manganites

The physical properties of doped transition metal oxides are the subject of intense experimental studies. Several fascinating phenomena are found in this class of compounds, such as magnetic order in the cuprates, or 'colossal magnetoresistance' in the manganites, but their theoretical understanding is not yet satisfactory. One of the open problems is the microscopic origin of the observed antiferromagnetic (AF) order in insulating $LaMnO_3$.

Ground state properties and low-energy excitations in strongly correlated transition metal oxides are generally assumed to be well described by effective Hamiltonians derived for the limit of a large on-site Coulomb interaction U. As an extension of the Heisenberg model, such models include also orbital degrees of freedom. Examples are: Cuprates (d^9 configuration of Cu^{2+}), nickelates (low-spin d^7 configuration of Ni^{3+}), and manganites (d^4 configuration of Mn^{3+}). In all cases, degenerate sets of e_g orbitals, ($|x\rangle \propto x^2-y^2$ and $|z\rangle \propto 3z^2-r^2$) are partly filled.

The case of a spin s = 1/2 model which describes the Cu^{2+} (d^9) ions in insulating $KCuF_3$, is described by

$$\mathcal{H}_{\rm Cu} \;=\; \sum_{\langle ij\rangle}\left\{-\frac{t^2}{\varepsilon(^3A_2)}\left(\vec{s}_i\cdot\vec{s}_j+\frac{3}{4}\right)\mathcal{P}^{\zeta\xi}_{\langle ij\rangle}+\frac{t^2}{\varepsilon(^1E)}\left(\vec{s}_i\cdot\vec{s}_j-\frac{1}{4}\right)\mathcal{P}^{\zeta\xi}_{\langle ij\rangle}\right.$$

$$\left.+\left[\frac{t^2}{\varepsilon(^1E)}+\frac{t^2}{\varepsilon(^1A_1)}\right]\left(\vec{s}_i\cdot\vec{s}_j-\frac{1}{4}\right)\mathcal{P}^{\zeta\zeta}_{\langle ij\rangle}\right\}-\frac{1}{2}E_z\sum_i(P_{ix}-P_{iz})\;, \qquad (9)$$

where t is the hopping element between $|z\rangle$ orbitals along the c-axis. The excitation energies of the $d_i^9 d_j^9 \rightleftharpoons d_i^8 d_j^{10}$ transitions, $\varepsilon(^3A_2) = U-2J_H$, $\varepsilon(^1E) = U$, and $\varepsilon(^1A_1) = U+2J_H$, depend on the Hund's rule element J_H in the excited Cu^{3+} (d^8) configuration. For each bond between neighbor atoms $\langle ij\rangle$ the operators $\mathcal{P}^{\alpha\beta}_{\langle ij\rangle}$ select the orbital states

$$\mathcal{P}^{\zeta\xi}_{\langle ij\rangle} \;=\; P_{i\zeta}P_{j\xi}+P_{i\xi}P_{j\zeta}\;, \qquad\qquad \mathcal{P}^{\zeta\zeta}_{\langle ij\rangle} = 2P_{i\zeta}P_{j\zeta}\;, \qquad (10)$$

being either alternating ($\mathcal{P}^{\zeta\xi}_{\langle ij\rangle}$), or parallel ($\mathcal{P}^{\zeta\zeta}_{\langle ij\rangle}$) to the bond. They are constructed with individual projection operators at each site i on the orbital parallel $|\zeta\rangle$ ($P_{i\zeta} = \frac{1}{2}-\tau_i^\alpha$) to the bond direction, and on the orbital perpendicular to it $|\xi\rangle$ ($P_{i\xi} = \frac{1}{2}+\tau_i^\alpha$). The orbital operators τ_i^α are associated with the three cubic axes (α = a, b, or c), and are built by the Pauli-matrices, $\tau_i^{a(b)} = \frac{1}{4}(-\sigma_i^z \pm \sqrt{3}\sigma_i^x)$, $\tau_i^c = \frac{1}{2}\sigma_i^z$. The last term $\propto E_z$ stands for the symmetry-breaking field in the orbital space.

A similar model for the e_g-superexchange between the total spins S = 2 of Mn^{3+} ions in insulating $LaMnO_3$ is

$$\mathcal{H}^{\rm e}_{\rm Mn} \;=\; \sum_{\langle ij\rangle}\left\{-J_1\left(\vec{S}_i\cdot\vec{S}_j+6\right)\mathcal{P}^{\zeta\xi}_{\langle ij\rangle}+J_2\left(\vec{S}_i\cdot\vec{S}_j-4\right)\mathcal{P}^{\zeta\xi}_{\langle ij\rangle}\right.$$

$$\left.+J_3\left(\vec{S}_i\cdot\vec{S}_j-4\right)\mathcal{P}^{\zeta\zeta}_{\langle ij\rangle}\right\}-\frac{1}{2}E_z\sum_i(P_{ix}-P_{iz})\;, \qquad (11)$$

where the interactions J_i depend on the $d_i^4 d_j^4 \rightleftharpoons d_i^5 d_j^3$ excitation energies, and may be derived from the multiplet structure of Mn^{2+} (d^5) ions. Both above models ($\mathcal{H}_{\rm Cu}$ and $\mathcal{H}^{\rm e}_{\rm Mn}$) contain superexchange couplings between spin and orbital degrees of freedom. The orbital sector carries a discrete Potts-like symmetry, and is *identical* in both cases, while the magnetic interactions follow from the actual filling of the 3d states and are described by *different representations of the SU(2) symmetry group* which apply to the cuprates (S = 1/2) and to the manganites (S = 2). The interactions between e_g holes in $\mathcal{H}_{\rm Cu}$ and between spins S = 2 in $\mathcal{H}^{\rm e}_{\rm Mn}$ are either AF with an exchange constant $J = t^2/U$ (if the orbitals are identical, $\sim \mathcal{P}^{\zeta\zeta}_{\langle ij\rangle}$), or ferromagnetic (FM) due to the multiplet splittings between the high- and low-spin excitations (then the orbitals are alternating, $\sim \mathcal{P}^{\zeta\xi}_{\langle ij\rangle}$). In the limit of $J_H \to 0$ the magnetic interactions are highly frustrated, with several classical states having the same energy at orbital degeneracy $E_z = 0$. If the spin order is AF, the orbitals may be chosen in an arbitrary way, while particular orbital alternations are found for states with FM planes that couple antiferromagnetically to each other (A-AF).

The phase diagrams of the spin-orbital models, $\mathcal{H}_{\rm Cu}$ and $\mathcal{H}^{\rm e}_{\rm Mn}$ are similar (Figs. 42 a and 42 b): Away from orbital degeneracy and for small J_H two AF phases are found with either $|x\rangle$ (AFxx) or $|z\rangle$ (AFzz) orbitals occupied by an e_g hole (Fig. 42 a) or electron (Fig. 42 b), while at large J_H one finds mixed orbitals (MO), $|i\mu\rangle = \cos\theta_i |ix\rangle + \sin\theta_i |iz\rangle$, and the magnetic order is FM in two cubic directions, and AF in the third (the order is AF along the c(a)-axis in the MOFFA(MOAFF) phase).

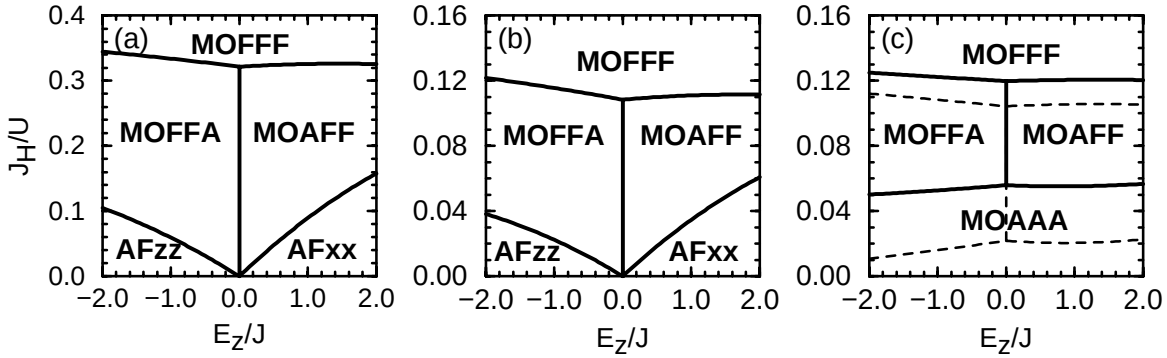

Figure 42: *Classical (E_z/J,J_H/U) phase diagram of the spin-orbital models at T=0: (a) cuprate model $\mathcal{H}_{\rm Cu}$; (b) e_g-superexchange in the manganite model ($\mathcal{H}^{e}_{\rm Mn}$); (c) manganite model $\mathcal{H}_{\rm Mn}$ with Jahn-Teller interactions κ=0.5J, for J_t=0 (dashed lines) and J_t=0.092J (solid lines).*

For Cu^{2+} ions in $KCuF_3$ the accepted value of $J_H/U \simeq 0.15$ indeed leads to the MOFFA phase. Due to larger multiplet splittings of Mn^{2+} (d^5) ions, the FM phase with MO (MOFFF) stabilizes at much lower value of J_H/U in the manganite model. This proximity of the MOFFA and MOFFF phases might be of importance for the theoretical understanding of magnetic phase transitions arising with doping. Indeed the FM phase stabilizes at intermediate doping, as observed in the exact diagonalization treatment of the Kondo lattice model (Horsch, Jaklič and Mack, 1997).

Transverse excitations investigated using an extension of the linear spin-wave theory in the cuprate case consist of the usual spin-waves and new spin-and-orbital-waves. These modes are well separated for large $|E_z/J|$, while the spin-and-orbital-wave becomes soft when the transition lines in the classical phase diagram are approached. This results in large quantum corrections δS^z to the magnetic order parameter $\langle S^z\rangle$, and the long-range-order collapses in a finite region between the AF and MO phases, where $|\delta S^z| > \langle S^z\rangle$ (Fig. 43), providing a new mechanism for a quantum *spin liquid* due to orbital degeneracy (Feiner, Oleś and Zaanen, 1997).

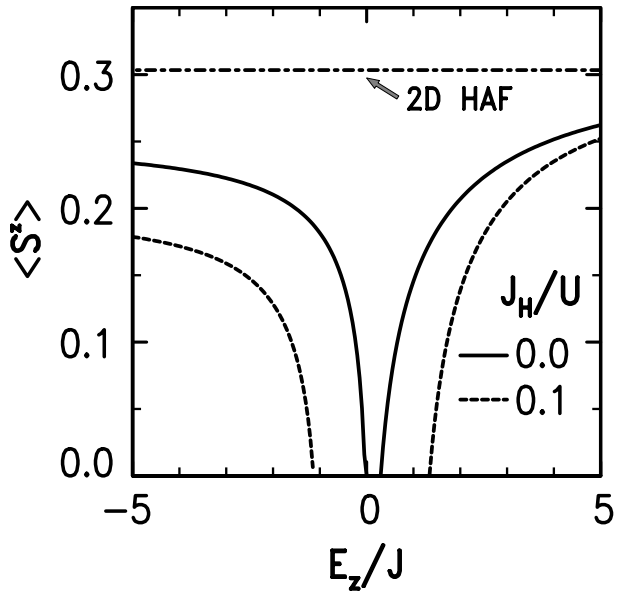

Figure 43: *Renormalization of AF order parameter $\langle S_i^z\rangle$ in AFzz (left) and AFxx (right) phases as functions of E_z/J. The value for the 2D Heisenberg model is shown by dashed-dotted line.*

The full microscopic model for insulating $LaMnO_3$,

$$\mathcal{H}_{\rm Mn} \;=\; \mathcal{H}^{\rm e}_{\rm Mn} + \mathcal{H}^{\rm t}_{\rm Mn} + \mathcal{H}_{\rm JT}\;, \tag{12}$$

includes not only the e_g superexchange $\mathcal{H}^{\rm e}_{\rm Mn}$ (Eq. (11)) but also the superexchange promoted by the hopping of t_{2g} electrons ($\mathcal{H}^{\rm t}_{\rm Mn}$), and the orbital interactions induced by the Jahn–Teller (JT) effect ($\mathcal{H}_{\rm JT}$),

$$\mathcal{H}^{\rm t}_{\rm Mn} \;=\; \frac{1}{4}{\rm J_t}\sum_{\langle {\rm ij}\rangle}\left(\vec{\rm S}_{\rm i}\cdot\vec{\rm S}_{\rm j}-4\right), \qquad \mathcal{H}_{\rm JT} = \kappa\sum_{\langle {\rm ij}\rangle}\left(\mathcal{P}^{\zeta\zeta}_{\langle {\rm ij}\rangle} - 2\mathcal{P}^{\zeta\xi}_{\langle {\rm ij}\rangle} + \mathcal{P}^{\xi\xi}_{\langle {\rm ij}\rangle}\right), \tag{13}$$

where $\mathcal{P}^{\xi\xi}_{\langle {\rm ij}\rangle} = 2{\rm P_{i\xi}P_{j\xi}}$. From spectroscopy, one obtains ${\rm J_H/U} = 0.095$, ${\rm J}\simeq 23\,{\rm meV}$, and ${\rm J_t}\simeq 0.092\,{\rm J}$. Thus, the e_g-superexchange is the dominating magnetic interaction and provides a generic explanation of the observed A–AF order (MOFFA/MOAFF phase) by an electronic mechanism. The superexchange parameters agree well with a small t_{2g}-superexchange in $CaMnO_3$, $\hat{\rm J}_{\rm t}\simeq 2.04\,{\rm meV}$, deduced from the magnetic transition at 110 K.

A quantitative explanation of the magnetic phase transition and the magnetic interactions requires to include the Jahn–Teller effect and the t_{2g}-superexchange. The orbital interaction, $\kappa\simeq 0.5\,{\rm J}$, estimated from the temperature ${\rm T_s}\approx 750\,{\rm K}$ of the structural phase transition, leads to alternation of the orbitals and to the MOAAA phase for small $\rm J_H$, while

the MOFFA/MOAFF phase remains stable at $J_H/U = 0.095$ and $E_z = 0$ (Fig. 42 c). The magnetic phase transition is found at $T_c = 148$ K (Fig. 44 a) using mean-field theory for the coupled spin and orbital order ($T_c^{exp} = 136$ K). The exchange constants calculated using the averages of the orbital operators $\langle \mathcal{P}^{\alpha\beta}_{\langle ij \rangle} \rangle$ are: $J_{(a,b)} = -1.15$ and $J_c = 0.88$ meV (Fig. 44 b), and agree well with the experimental values –0.83 and 0.58 meV for insulating $LaMnO_3$.

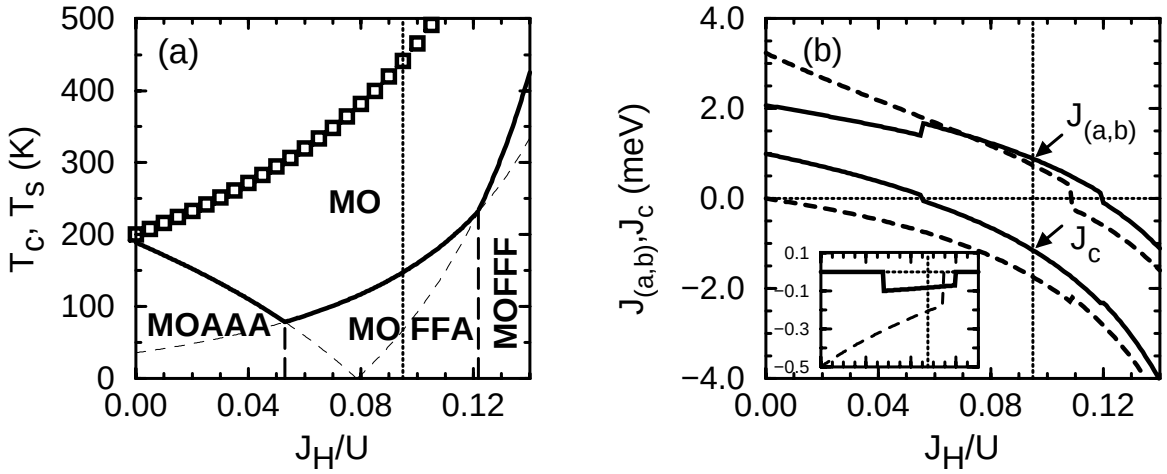

Figure 44: *Transition temperatures (a) and exchange constants (b) as obtained in the manganite model $\mathcal{H}_{\rm Mn}$ with experimental parameters: J_t=0.092J, κ=0.5J and J=23meV. The magnetic transition temperatures T_c correspond to the phases found in Fig. 42 c at T=0; the temperature of the structural transition T_s (squares) does not include the JT part (κ=0). The exchange constants $J_{(a,b)}$ and J_c (b) are given for the experimental parameters (full lines) and for J_t=κ=0 (dashed lines); the inset shows the orbital angle $\cos 2\theta$. The dotted lines indicate realistic J_H/U=0.095.*

In summary, the spin-orbital model $\mathcal{H}_{\rm Mn}$ for insulating $LaMnO_3$ derived here yields a quantitative understanding of the observed magnetic and orbital order. It is expected that an intended generalization of the t-J model for doped manganites that also includes the orbital dynamics, would provide a more satisfactory description of magnetic and transport properties of the 'colossal magnetoresistance' compounds than obtained at present by the double exchange model (Millis *et al.*, 1995; Ohimoto *et al.*, 1997).

(A.M. Oleś and L.F. Feiner (Philips, Eindhoven))

Magneto-chiral anisotropy

The discovery of natural optical activity by Arago (1811) in chiral crystals and of magnetically induced optical activity by Faraday (1846) in glass have contributed much to our understanding of the wave nature of light and of its interaction with matter. Guided by the phenomenologic similarity between the two effects, Pasteur was the first to search – in vain – for a link between them. Only in recent years, predictions have appeared of a cross-effect between natural and magnetic optical activity, which can discriminate between the two enantiomers (mirror images) of a chiral system, which was the mainspring behind Pasteur's search. Here we will present the first experimental evidence for the existence of such a magneto-chiral optical effect and its enantioselectivity.

There is indeed a strong phenomenological resemblance between natural and magnetic optical activity. Both represent a difference in absorption and refraction between left and right circularly polarized light, the former in chiral media, the latter in all media subject to a magnetic field $\overrightarrow{B}$ parallel to the wave vector of the light $\overrightarrow{k}$. The two effects however have completely different physical origins. Natural optical activity (NOA) is a result of a non-local optical response in media that lack mirror symmetry, whereas magnetic optical activity (MOA) results from the breaking of time-reversal symmetry by the magnetic field. It should therefore not be surprising that under conditions where both symmetries are broken simultaneously, a physical situation exists that allows for an additional optical effect to manifest itself. The existence of such an effect, which can also be considered to be a cross-effect between natural and magnetic optical activity, was first seriously implied in the '60s in calculations of magneto-optical rotation by chiral molecules. On the basis of symmetry arguments, one can infer the existence of an additional contribution to the dielectric constant of a chiral medium subject to a magnetic field of the form $\mathbf{k}\cdot\mathbf{B}$, independent of polarization, and of opposite sign for the two enantiomers d and l of the medium;

$$\varepsilon_{\pm}(\omega,\mathbf{k},\mathbf{B}) = \varepsilon_0(\omega) \pm \alpha_{\mathrm{d/l}}(\omega)\cdot \mathrm{k} \pm \beta(\omega)\cdot \mathrm{B} + \gamma_{\mathrm{d/l}}(\omega)\cdot\mathbf{k}\cdot\mathbf{B}\ , \qquad (14)$$

where $x_d = -x_l$, $+/-$ refers to right- and left circularly polarized light, α describes NOA and β describes MOA. Detailed molecular calculations confirmed the existence of such an effect, and in analogy with natural and magnetic optical activity, it was baptized magneto-chiral dichroism in absorption/emission and magneto-chiral birefringence in refraction. The existence of such a magneto-chiral anisotropy, already important from the point of view of fundamental light-matter interaction and molecular spectroscopy, may have even far-reaching implications, as it has been put forward as a possible explanation for the homochirality of life.

Although there seems to be theoretical unanimity on the existence of magneto-chiral anisotropy, it has never been observed experimentally. This is no doubt due to the expected weakness of the effect, as both MOA and NOA are in most materials only small perturbations of the optical properties and their cross-effect is therefore likely to be very small. However, this need not allways be the case. The most strongly chiral transitions reported in literature are the $^5D_0 \rightarrow {}^7F_{1,2}$ luminescent transitions in the chiral

tris(3-trifluoroacetyl-±-camphorato) europium(III) complexes (Eu((±)tfc)$_3$), which show almost completely circularly polarized emission after unpolarized excitation. These transitions have also been shown to have a reasonably large magnetic circular dichroism and these complexes are therefore likely candidates to show a significant magneto-chiral effect at these transitions. As the luminescence probability is described by the imaginary part of the dielectric constant, magneto-chiral anisotropy should be visible in the luminescence intensity.

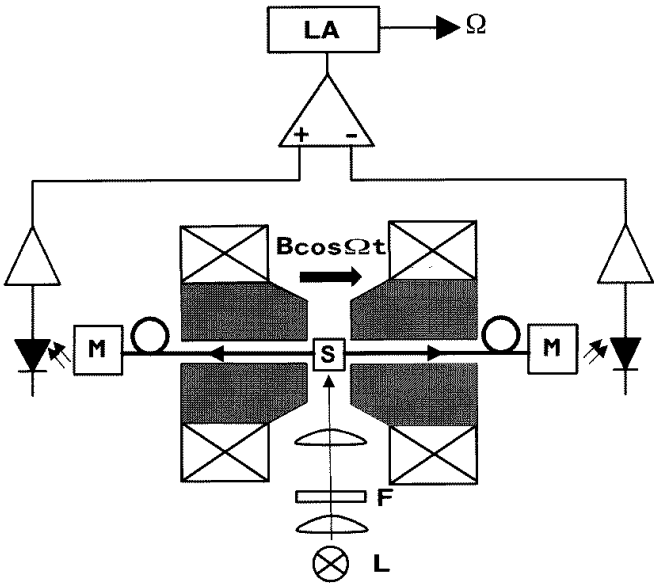

Figure 45: *Schematic set-up to detect magneto-chiral luminescence anisotropy. Sample (S) is excited around 350nm with filtered (F), unpolarized light from a mercury-discharge lamp (L). Luminescence is collected in the directions parallel and anti-parallel to the magnetic field by optical fibers (NA=0.47), specific emission wavelengths are selected by a monochromator (M), and detected by photo-diodes. The intensity difference between the two directions is phase-sensitively detected by a lock-in amplifier (LA) at the frequency Ω=0.9Hz at which the magnetic field is alternated.*

The experiment performed by us to observe such an anisotropy is illustrated in Fig. 45. It measures the difference in luminescence intensity in the directions parallel and anti-parallel to the externally applied magnetic field B. In order to increase the sensitivity, the magnetic field is alternated and the intensity difference is phase-sensitively detected. Factors related to excitation intensity, complex concentration and sample geometry are eliminated by dividing the lock-in output by the total, static luminescence signal. The resulting quantity is the magneto-chiral anisotropic luminescence factor g, given by:

$$g = \frac{\frac{\partial}{\partial B}\left(I_{\hat{B}\uparrow\uparrow\hat{k}} - I_{\hat{B}\uparrow\downarrow\hat{k}}\right)B}{I_{\hat{B}\uparrow\uparrow\hat{k}} + I_{\hat{B}\uparrow\downarrow\hat{k}}} \tag{15}$$

Figure 46 shows the experimental results for g for the two enantiomers of the Eu((±)tfc)$_3$ complex, showing significant magneto-chiral anisotropy at both transitions. An essential characteristic of the effect is that at all wavelengths, g should be of opposite sign for the two enantiomers. This feature is observed within the experimental accuracy. The inset shows the expected linear magnetic field dependence of g.

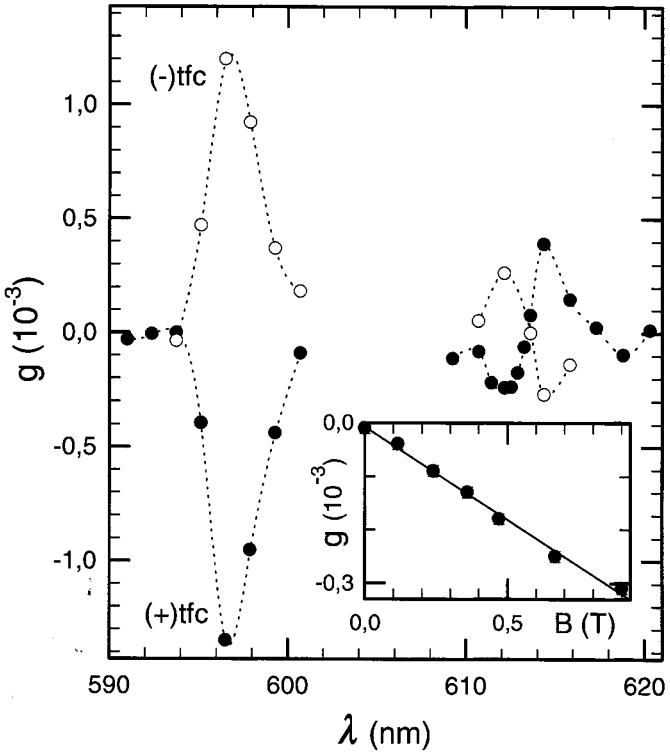

Figure 46: *Magneto-chiral luminescence anisotropy of Eu((±)tfc)$_3$ complexes as a function of luminescence wavelength, with excitation around 350nm. The (alternating) magnetic field strength was 0.9T. Filled symbols represent the Eu((+)tfc)$_3$ complex, open symbols its enantiomer, the Eu((–)tfc)$_3$ complex. Dashed lines are only meant to guide the eye. The inset shows the magneto-chiral anisotropy of the Eu((–)tfc)$_3$ complex as a function of magnetic field strength, excitation around 350nm, luminescence detected at 615.8nm. Solid line is a linear fit.*

Therefore, Fig. 46 constitutes the irrefutable proof for the existence of magneto-chiral anisotropic luminescence and its enantioselectivity. In a simple approximation one can estimate as order of magnitude for the magneto-chiral anisotropy the product of the magneto-circular and the natural-circular dissymmetry factors. For the $^5D_0 \rightarrow ^7F_1$ transition this would amount to $g \approx 5.10^{-3}$, in fair agreement with what we observe. A quantitative comparison of our experimental results with the existing molecular theory requires detailed knowledge of all the electric dipole-, magnetic dipole- and electric quadrupole transition moments involved and their interplay.

Now that magneto-chiral anisotropy has been shown to exist in emission, i.e. in the imaginary part of the dielectric constant, we can be sure through the Einstein relations between the radiative transition probabilities that it will also exist in absorption (magneto-chiral dichroism). The Kramers–Kronig relations imply that it will also exist in the real part of the dielectric constant, i.e. in refraction (magneto-chiral birefringence).

(G.L.J.A. Rikken and E. Raupach)

New structures and compounds

Alkali metal compounds with the Zintl-anions $[Si_9]^{4-}$, $[Ge_9]^{4-}$ and $[Sn_9]^{4-}$

It was assumed up to now that the formation of the cluster anions $[E_9]^{n-}$ only starts with the reaction of precursors ME_n in appropriate solvents (M = alkaline metals, E = E14 elements, and $2 < n < 3$). Important arguments for this opinion are taken, e.g. from the binary phase diagrams M / Ge obtained by thermal analyses. Furthermore, intermediate phases were never identified in the course of thermal decomposition reactions of M_4E_4 phases, forming the clathrates. Only the intermediate stannides MSn_2 and M_2Sn_3 are known (Table 4), but not yet characterized structurally.

Table 4. *Phases with cluster anions* E_4^{4-} *and* E_9^{4-} *(E = Ge and Sn).*

System	Phase diagram		Vibrational spectra		X-ray powder data		Structure from single crystal data	
	12:17	4:9	12:17	4:9	12:17	4:9	12:17	4:9
Na / Ge	-	-	+		+		+	
K / Ge	-	-	+	+	+	+	+	+
Rb / Ge	-	-	+	+	+	+		
Cs / Ge	-	-	+	+				
Na / Sn	-	$NaSn_2$						
K / Sn	K_2Sn_3	KSn_2	+	+				
Rb / Sn	Rb_2Sn_3	$RbSn_2$	+		+			
Cs / Sn	Cs_2Sn_3	$CsSn_2$	+	+	+			

Now after numerous futile efforts, we were able to establish the existence of the phases $M_{12}E_{17}$ and M_4E_9 in most of the binary systems. The characterization was done by chemical analysis, X-ray powder diffraction, single crystal structure analysis and vibrational spectra (Table 4).

The germanides are formed by thermal decomposition of the tetrahedranides $M_4Ge_4 = MGe$ in dynamic vacuum. The thermal decomposition of K_4Ge_4 (Fig. 47) gives strong evidence for the existence of several other compounds, namely $K_{16}Ge_{31}$ ($[Ge_4]^{4-} + 3[Ge_9]^{4-}$), $K_{12}Ge_{22}$, K_6Ge_{25}, K_xGe_{136} in addition to $K_{12}Ge_{17}$, K_4Ge_9, $K_8Ge_{44}\square_2$. The direct synthesis from the elements under related conditions is also successful if loss of the alkaline metal is avoided.

The compounds are extremely sensitive (air, moisture). The $M_{12}Ge_{17}$ phases and all the stannides are black. On the other side, K_4Ge_9, Rb_4Ge_9 and Cs_4Ge_9 are black, dark red and phosphorous-red, respectively, and they become dark red, phosphorous-red and orange after grinding. With EN and $NH_3(l)$, the binary phases form yellow-brown (Ge) and red (Sn) solutions, which become dark red with increasing concentration. The solutions of K_4Ge_9 in EN are diamagnetic (ESR).

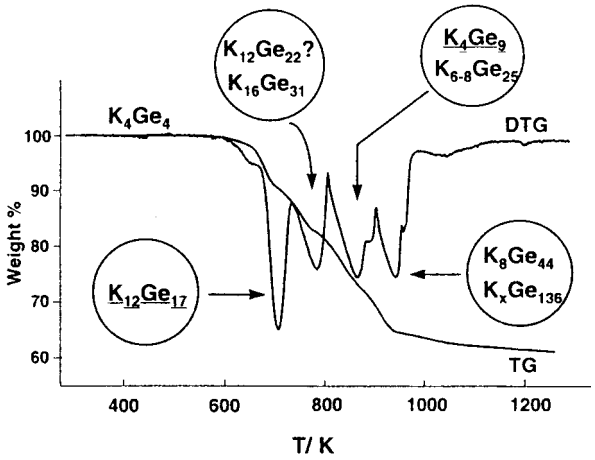

Figure 47: *Thermal decomposition of K_4Ge_4 in dynamic vacuum (TG; DTG). The mass spectra show that only potassium evaporates.*

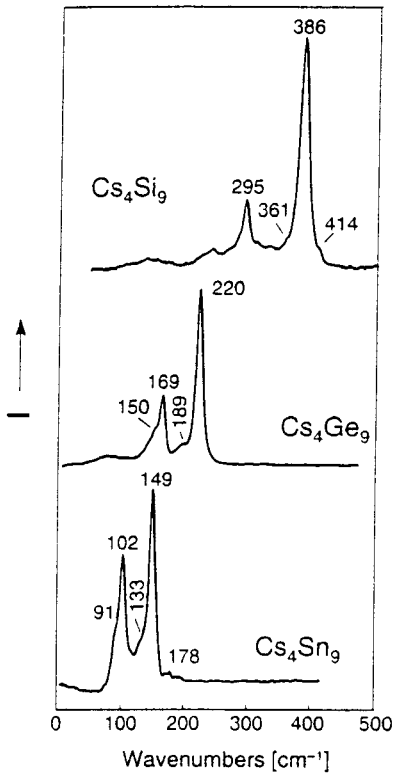

Figure 48: *Raman spectra of the binary compounds with the Zintl-anions $[E_9]^{4-}$.*

The characteristic patterns of the vibrational spectra (Fig. 48) and their assignment to the cluster anions $[E_4]^{4-}$ and $[E_9]^{4-}$ were decisive for the identification of the crystalline phases, as well as their solutions and extraction products. The spectra of tetrahedranide anions were analyzed earlier. One expects for a $[E_9]^{4-}$ cluster with the symmetry 4*mm* ($C_{4\nu}$) the following 21 fundamentals: $\Gamma_{vib} = 4A_1(R, IR) + A_2(B, B) + 3B_1(R) + 3B_2 + 5E(R, IR)$, with A_2 being inactive and forbidden. The remaining 21 modes are Raman active, A_1 and E are also infrared active. The measured Raman spectra exhibit four (Sn) and five (Ge) broad bands. Frequencies and intensities are in excellent agreement with the calculated Raman spectrum for a discrete $[E_9]^{4-}$ anion with 4*mm* ($C_{4\nu}$) symmetry. The small number of observed Raman active bands is attributed to accidental coincidences and low intensities. The simple vibrational patterns with the characteristic Raman frequencies of about 220 cm^{-1} ($[Ge_9]$) and 152 cm^{-1} ($[Sn_9]$), as well as 274 cm^{-1} ($[Ge_4]$) and 185 cm^{-1} ($[Sn_4]$), respectively, can be used as identification sondes. Characteristic is also the wave number ratio κ of the breathing modes $\kappa = \nu([E_9])/\nu([E_4]) = 0.81$ (Ge) and 0.82 (Sn), respectively. The splitting of the $F_2(\nu_2)$ vibration in solid K_4Ge_4 (185 cm^{-1} and 200 cm^{-1}, originating by the site symmetry vanishes, and only one medium strong band at 199 cm^{-1} occurs in the $K_{12}Ge_{17}$ spectrum.

The crystal structures of $Na_{12}Ge_{17}$, $K_{12}Ge_{17}$, and K_4Ge_9 were determined by X-ray single-crystal methods (Fig. 49). The X-rays powder patterns show very characteristic reflection sequences, useful for identifying the phases. These characteristics arise (as in the case of KGe and $K_8Ge_{44}\square_2$) from the hierarchical analogy of the structures to the Cr_3Si type (*cP*8) as well as to the $MgZn_2$ type (*hP*12): Me = $[(M_4E_4)_3\ (M_4E_4)_1]$, $M_4E_9 = [(M_4E_9)_3\ (M_4E_9)_1]$, $M_8E44\square_2 = [(M@E_{22.67/4}\square_{1.33/4})_3(M@E_{20/4})_1]$ and $M_{12}E_{17} = [(M_4E_9)_1\ (M_4E_4)_2]$, respectively. The first three typical reflections or reflection groups of M_4E_4 and M_4E_9 structures correspond to the cubic indices (200), (210) and (211) of the Cr_3Si structure. The three strongest reflection groups of the $M_{12}E_{17}$ structure correspond to the (11.0), (01.3) and (11.2) reflections of the hexagonal $MgZn_2$ structure.

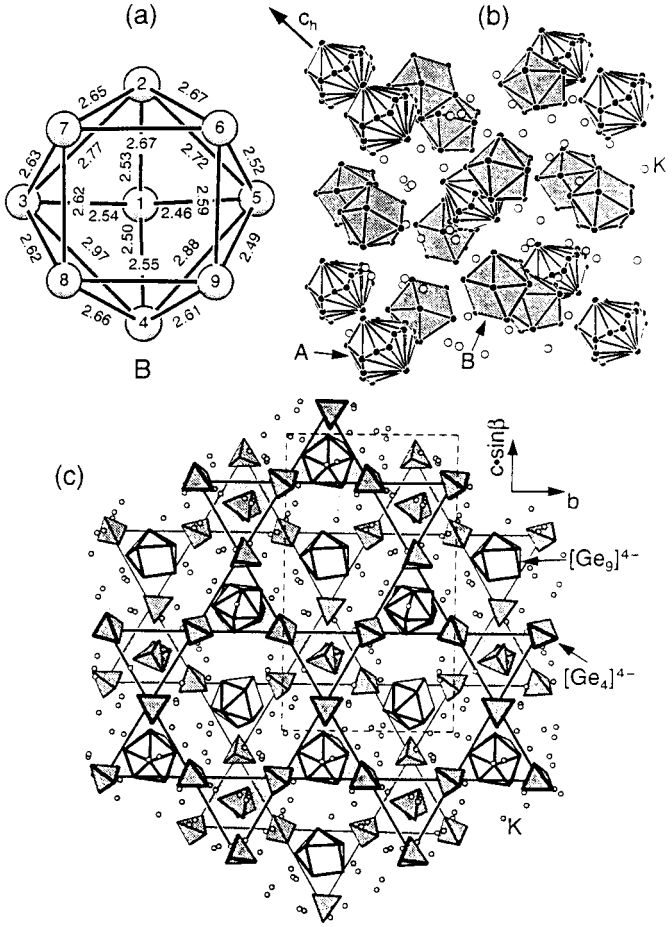

Figure 49: *(a) The $[Ge_9]^{4-}$ cluster (22e nido-E_{10} Wade-cluster) of B-type in K_4Ge_9 with distances (C) and atom labels. (b) Quasi-cubic setting of the rhombohedral K_4Ge_9 structure (hierarchical variant of the Cr_3Si structure) with orientational disordered (A-type) and ordered (B-type) $[Ge_9]^{4-}$ clusters. (c) Quasi-hexagonal [100] projection of the monoclinic structure of $K_{12}Ge_{17}=K_{12}[Ge_9]_1[Ge_4]_2$, a hierarchical variant of the hexagonal Laves phase $MgZn_2$.*

The rhombohedral K_4Ge_9 structure contains two crystallographically different $[Ge_9]^{4-}$ clusters, A and B, with the ratio $B_a = 3.1$. In the quasi-cubic setting ($a = 14.82$ Å, $\alpha = 90.78°$), the distribution of the cluster centres can easily be seen as the Cr_3Si structure motif (Fig. 49). The ordered cluster (B-type) is a mono-capped tetragonal antiprism

with only small deviations from 4*mm* ($C_{4\nu}$) symmetry (Fig. 49). The A-type cluster approximately represents three-fold orientational disordered 4*mm* ($C_{4\nu}$) cluster around the three-fold axis. In $K_{12}Ge_{17}$ ($Na_{12}Ge_{17}$), the $[Ge_4]$ clusters occupy the nodes of a 3.6.3.6 Kagome net (Fig. 49). These nets are stacked in a $MgZn_2$-type arrangement with the $[Ge_9]$ clusters at the Mg positons.

Very recently, we were able to identify for the first time the $[Si_9]^{4-}$ cluster anion. Careful thermal decomposition of Cs_4Si_4 shows that phases line '$M_{12}Si_{17}$' and 'M_4Si_9' exist also in the binary systems M / Si. The identification was done by the Raman spectra exhibiting the characteristic vibrational patterns of the $[E_9]^{4-}$ anions (E = Ge, Sn) with $\kappa = \nu([E_9])/\nu([E_4]) = 0.81$ also for Cs_4Si_9 and Cs_4Si_4 (Fig. 48). The constand κ value for the whole $[E_9]/[E_4]$ series clearly indicates that the bond strength in the corresponding clusters are comparable.

(H.G. von Schnering, M. Baitinger, U. Bolle, W. Carrillo-Cabrera, J. Curda, Y. Grin, F. Heinemann, J. Llanos, K. Peters and M. Somer)

The carbon-centered *triprismo*-hexatungsten chlorides $C@W_6Cl_{16}$ and $C@W_6Cl_{18}$

The two cluster types $(M_6X_8^i)$ and $M_6X_{12}^i$ with octahedral M_6 cores are characteristic for a large number of transition metal compounds in lower oxidation states. Numerous $(M_6X_{12}^i)$ cluster compounds with interstitial heteroelements were identified, but Simon's $(HNb_6I_8^i)I_3^{a-a}$ is one of the very rare examples with the $(M_6X_8^i)$ cluster. Very recently the first sulfur-centered *triprismo*-hexaniobium halides have been reported which are derivatives of the WC structure type. Now we identified the first carbon-centered *triprismo*-hexatungsten halides.

At first we found serendipitously mixtures of CW_6Cl_{16} and CW_6Cl_{18} formed at the high temperature zone by heating purchased WCl_4 (Aldrich) in evacuated silica tubes at the temperature gradient 925 K/915 K. The reaction is reproducible. This purchased 'WCl_4' was then confirmed to be a horrible mixture containing WCl_5, $WOCl_4$ and organic compounds. *It is worthy to note here that nowadays progress in chemical synthesis results frequently from the use of such chemicals, whereas in former times the old fashion chemists were proud of using own products as starting materials*. It was then shown by a series of syntheses that the new compounds contain carbon and does not contain oxygen. CW_6Cl_{16} is best synthesized by heating tungsten, WCl_6 and graphite (ratio 3.44 : 2.67 : 1) at the temperature gradient 1030 K/870 K for one week, and the product deposits at the low temperature zone. CW_6Cl_{18} is synthesized from tungsten, WCl_6 and graphite (ratio 1 : 1.11 : 1.50) at the temperature gradient 975 K/965 K for one week, and the product is found at the high temperature zone but was contaminated by unreacted elementary tungsten and graphite. The excess of graphite was separated by floating in water.

The polymeric CW_6Cl_{16} and the molecular CW_6Cl_{18} are black crystalline compounds (dark greenish-gray after grinding). They are not sensitive to air and water. The molecular CW_6Cl_{18} is soluble in dimethylsulfoxide (DMSO) at 360 K forming green solutions with characteristic absorptions at 2900 cm^{-1}, 16500 cm^{-1} and 24400 cm^{-1}. CW_6Cl_{16} is diamagnetic with $\chi_{mol} = -835 \times 10^{-6}$ $cm^3\,mol^{-1}$. Under dynamic vacuum, the thermal decomposition starts at 870 K (weight loss 71.5% up to 1060 K). The residue is a mixture of W and W_2C. The far IR spectrum shows numerous peaks. The ^{13}C NMR spectrum of CW_6Cl_{18} was measured in deuterated DMSO solution and shows a sharp singlet with a chemical shift $\delta(^{13}C) = +279.7$ ppm (300 K) with tetramethylsilane as standard. The ^{13}C chemical shift corresponds to the 297 ppm signal of the carbonyl cluster compound $[C@Rh_6(CO)_{15}]$. The ^{13}C NMR of solid CW_6Cl_{16} is also characterized by a unique singlet at 264.3 ppm.

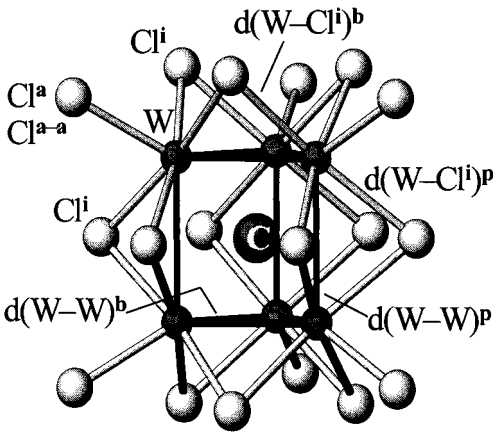

Figure 50:

d [Å]	CW_6Cl_{16}	CW_6Cl_{18}
$\bar{d}_{(W-W)^b}$	2.660 [2.640–2.670]	2.743 [2.743 6×]
$\bar{d}_{(W-W)^p}$	3.020 [3.007–3.045	2.929 [2.929 3×]
$\bar{d}_{(W-Cl^i)^b}$	2.390 [2.381–2.396]	2.362 [2.357–2.366]
$\bar{d}_{(W-Cl^i)^p}$	2.456 [2.448–2.478]	2.435 [2.433–2.436]
$\bar{d}_{(W-Cl^a)}$	2.388 [2.386–2.390]	2.378 [2.378 6×]
$\bar{d}_{(W-Cl^{a-a})}$	2.548 [2.539–2.556]	
$\bar{d}_{(W-C)}$	2.15 [2.08–2.26]	2.157 [2.157 6×]

Table 5

The crystal structure of CW_6Cl_{18} is a *hcp* type arrangement of isolated $(C@W_6^{TPR}Cl_{12}^i)Cl_6^a$ cluster molecules (Fig. 50). Six of the inner Cl^i ligands bridge the edges of the two triangular faces of the W_6^{TPR} trigonal prism whereas the remaining three edges are bridged pairwise by the other six Cl^i ligands. The W atoms are bonded to four Cl^i and one outer Cl^a ligand, and they are involved in two stronger (triangle) and one weaker W-W bond (Fig. 50, Table 5). The distance to the central C atom is remarkable in that the lost of four electrons (formation of C^{4-}) transfer the *octahedro*-$(W_6Cl_{12}^i)Cl_6^a$ into the *triprismo*-$(CW_6Cl_{12}^i)Cl_6^a$ ($18e/W_6 \longrightarrow 14e/W_6$). The crystal structure of CW_6Cl_{16} contains puckered 2D layers of interconnected clusters $^2_\infty[C@(W_6^{TPR}Cl_{12}^i)Cl_2^aCl_{4/2}^{a-a}]$. The W_6^{TPR} core $(16e/W_6)$ is slightly distorted and differs in the W-W bond lengths from the other unit (Table 5). The C atom is asymmetrically shifted from the W_6 center.

(Y.-Q. Zheng, Yu. Grin, G. Heckmann, G. Engelhardt and H.G. von Schnering)

$[PtIn_6]$ octahedra in low valent indiumfluorides and indiumoxides – a new class of highly ionic compounds containing main group element clusters

The search for new compounds containing low valent metal atoms seems especially worthwhile since unusual chemical and physical properties are mostly connected to the *non-closed* shell configurations of individual elements. This applies especially to fluorides or oxides, as the highly ionic character of these compounds in combination with the kind of chemical bonding of the excess valence electrons (delocalized, lone pairs, metal clusters ...) leads to interesting properties. However, low valent oxides and fluorides are often difficult to obtain because of their tendency to disproportionate. The chemistry of In serves as a good example. Any efforts to prepare InO or In_2O have failed so far. With the exception of $InBF_4$, which has been synthesized at low temperature in liquid HF, fluorides containing In in an oxidation state less then +3 are also up to now unknown, in spite of some efforts for its syntheses which date back into the thirties.

The two new mixed valent fluorides $PtIn_7F_{13} = [PtIn_6]^{10+}In^{3+}F_7^-$ and $Pt_3In_{22}F_{40} = ([PtIn_6]^{10+})_3In_3^{3+}In^+F_{40}^-$ have been obtained by the reduction of InF_3 by In in the presence of Pt. Characteristic building units in both structures are $[PtIn_6]^{10+}$ octahedra, which are surrounded by 24 F to form a $[PtIn_6]F_{24}$ cluster, see Fig. 51 a. The Pt-In distances are very short ($d_{Pt-In} = 254$–256 pm) compared to the corresponding distances in intermetallic phases like Pt_3In_7, in which Pt is square antiprismatically coordinated by 8 In ($d_{Pt-In} = 273$–277 pm). The $[PtIn_6]F_{24}$ clusters are connected through $[InF_6]^{3-}$ octahedra to a three-dimensional network. Besides $[PtIn_6]^{10+}$ and $[InF_6]^{3-}$ octahedra $Pt_3In_{22}F_{40}$ contains additional In^+ embedded into a cage of 15 F with In-F distances of 280–360 pm, see Fig. 51 b. Such a high coordination number is normally only found in intermetallic phases and has never been observed in an ionic compound. Obviously In^+ is an extremely large ion because of the extension of the lone pair of electrons. According to extended Hückel calculations this lone pair has nearly pure 4 s character and exhibits no stereochemical activity despite the rather asymmetric surrounding.

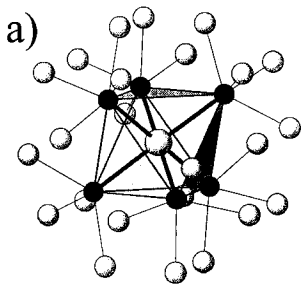

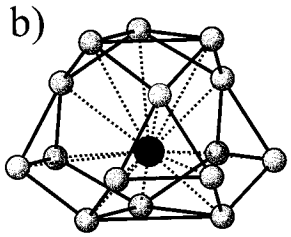

Figure 51: *a) $[PtIn_6]^{10+}$ octahedron together with the 24 surrounding F, and b) $[InF_{15}]^{14-}$ polyhedron in $Pt_3In_{22}F_{40}$.*

There are three possibilities for the charge distribution within the $[PtIn_6]^{10+}$ octahedra resulting in integer oxidation states for the In and Pt atoms, which are all in agreement with an octahedral surrounding for Pt with respect to the approach of the ligand field theory. In all three cases Pt achieves a stable 18 electron configuration assuming that In^+ is a 2-electron σ-donor and In^{2+} is a 1-electron σ-donor, respectively.

$$[Pt^{4+}In_6^{+}]^{10+} \quad \longleftrightarrow \quad [Pt^{2-}In_6^{2+}]^{10+} \quad \longleftrightarrow \quad [Pt^{8-}In_6^{3+}]^{10+}$$

According to bond order summations, calculations of the Madelung part of lattice energy and also Mulliken population analysis the most reasonable oxidation states seem to be +2 for the In atoms and –2 for the Pt atoms, which are then isoelectronic to the well-known Au^-, as it is found in CsAu. However, semi-empirical quantum mechanical calculations show, that considerations in terms of an ionic limit are too simplified and that within the $PtIn_6$ octahedra both Pt-In interactions and In-In interactions are present, see Fig 52.

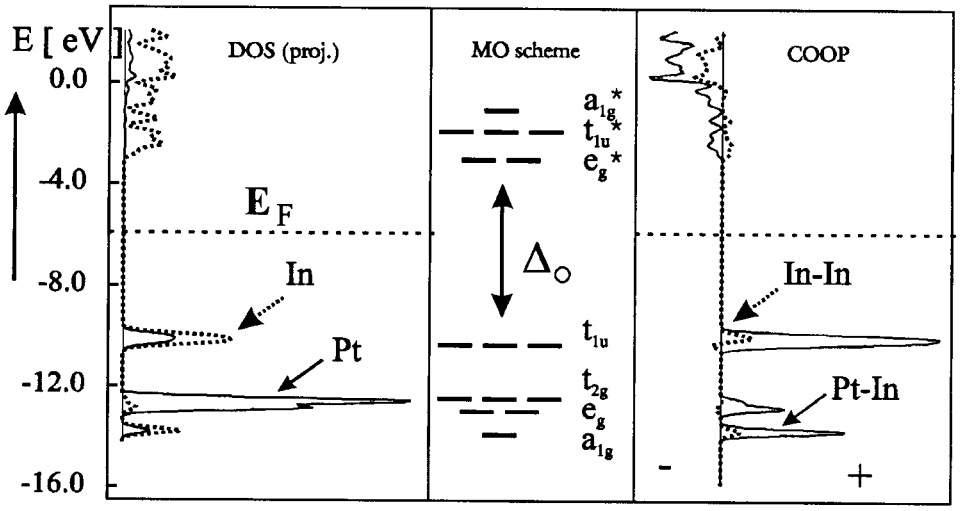

Figure 52: *Projected density of states (DOS, left), energy level diagram (middle) and crystal orbital overlap population (COOP, right) for the metal centered orbitals of a $[PtIn_6]F_{24}$-cluster.*

In contrast to the well-known complexes $[Pt(NH_3)_6]^{4+}$, $W(CO)_6$ or $[PtCl_6]^{2-}$, the HOMO of a $[PtIn_6]^{10+}$ cluster is a t_{1u} state and the calculated band gap Δ_0 is determined by the difference in energy between this state and e_g^* (LUMO). This band gap Δ_0 is, as expected, slightly larger than the optical gap determined by UV absorption spectroscopy of approximately 3.3 eV, which corresponds to the pale yellow color of the crystals of $PtIn_7F_{13}$ and $Pt_3In_{22}F_{40}$.

Besides Nb_6F_{15} which is known for a long time $PtIn_7F_{13}$ and $Pt_3In_{22}F_{40}$ are the first fluorides containing clusters with metal-metal bonds. The structure solutions of other compounds in the system Pt-In-F is difficult because of the bad quality of the obtained crystals. The replacement of In by Ga and F by O has recently led to the discovery of the new mixed valent compounds $Pt_2In_{14}Ga_3O_8F_{15}$ and $PtIn_6(GaO_4)_2$, which also contain $PtIn_6$ octahedra. Both, the oxidfluoride and the oxid, are stable in air, against water and *non*-oxidizing acids. $PtIn_6(GaO_4)_2$ is isotypic to Co_9S_8 (or the mineral Pentlandit $(Fe,Ni)_9S_8$) which according to $[CoS_6](SCo_4)_2$ consists of CoS_6 octahedra and SCo_4 tetrahedra, see Fig. 53.

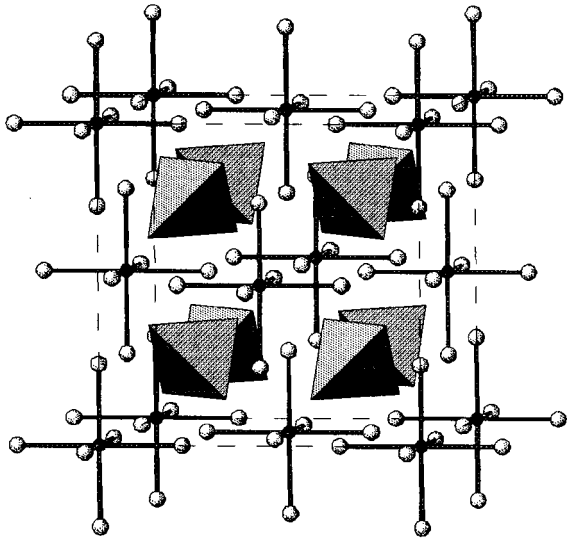

Figure 53: *Projection of the crystal structure of $PtIn_6(GaO_4)_2$. Dashed lines represent the cubic unit cell. $PtIn_6$ octahedra and GaO_4 tetrahedra are graphically emphasized.*

The remarkably simple cubic structure derives from the CaF_2 type structure by replacing Ca by $PtIn_6$ octahedra and F by GaO_4 tetrahedra. The Pt-In distances (d_{Pt-In} = 254 pm) are comparable to the corresponding distances in the fluorides discussed above. Powder samples of $PtIn_6(GaO_4)_2$ are black, indicating a semiconducting or metallic conductivity, which might result from short *inter*-cluster and short *intra*-cluster distances leading to an extended three-dimensional network of $PtIn_6$ and empty $\square In_6$ octahedra. This arrangement of octahedra corresponds to the three-dimensionally net of corner-sharing Nb_6 octahedra in NbO. It seems promising to look for further representatives of this new class of highly ionic compounds with main group element clusters centered by a transition metal atom and their chemical bonding and properties.

(J. Köhler, J.-H. Chang and H. Friedrich)

The lanthanum and cerium antimonide oxides $La_9Sb_5O_5$ and $Ce_9Sb_5O_5$

Trying to prepare 'La_4Sb_2O', the compound $La_9Sb_5O_5$ was obtained as the main product of the reaction of La and Sb with Sb_2O_3 ($\approx$ 1g, ratio 12 : 4 : 1) in sealed niobium ampoules at 1530 K. Microcrystalline one-phase samples of $La_9Sb_5O_5$ were synthesized from stoichiometric mixtures of La, Sb and Sb_2O_3 (ratio 27 : 5 : 5):

$$27La + 5Sb_2O_3 + 5Sb \xrightarrow{1770K} 3La_9Sb_5O_5 \qquad (16)$$

The isotypic $Ce_9Sb_5O_5$ was synthesized from Ce, Sb_2O_3 and Sb (the sample contains small amounts of an additional phase). Both compounds form grey crystals with metallic lustre. They are sensitive to air and moisture. The residuals are black powders which have not been identified yet.

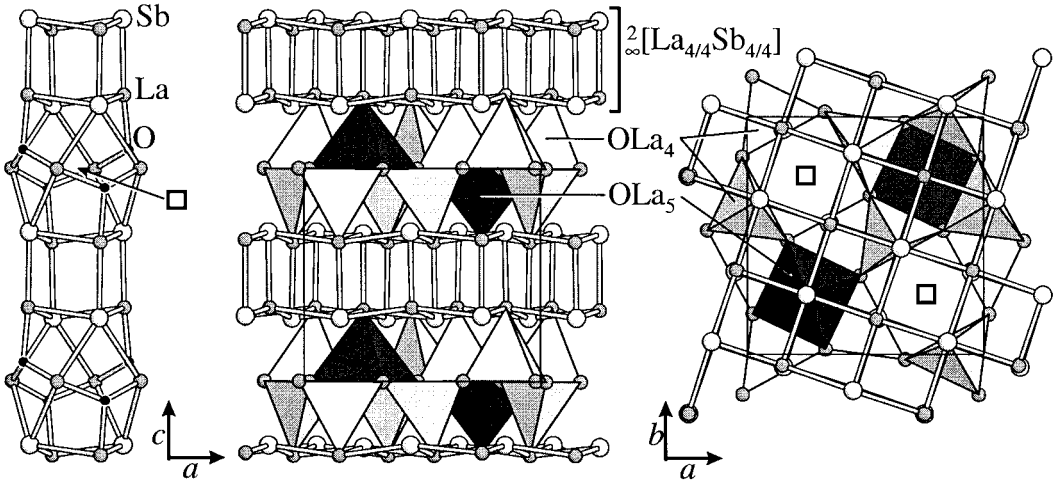

Figure 54: *Perspective view of the $La_9Sb_5O_5$ structure.*

$La_9Sb_5O_5$ (Fig. 54) and $Ce_9Sb_5O_5$ crystallize in a new *tP38* structure type: Space group *P*4/n (no. 85); Z = 2; a = 1041.5(1) pm; c = 934.0(1) pm; c/a = 0.897 ($La_9Sb_5O_5$); a = 1029.7(1) pm; c = 922.8(1) pm; c/a = 0.896 ($Ce_9Sb_5O_5$). The $La_9Sb_5O_5$ structure is characterized by a two-dimensional network $^{2}_{\infty}[La_{4/4}Sb_{4/4}]$ of distorted face sharing La_4Sb_4 cubes ($\bar{d}$(La-Sb) = 333 pm) which are also found in the compounds La_2Sb or Eu_4Sb_2O. This network can be also considered as build up from face shared pyramids $LaSb_5$: $^{2}_{\infty}[LaSb_{5/5}]$. The NaCl type fragments are separated by tetrahedra OLa_4 ($\bar{d}$(O-La)=238 pm) and tetragonal pyramids OLa_5 ($\bar{d}$(O-La) = 258 pm) condensed via common edges $^{2}_{\infty}[(OLa_{1/1}La_{3/4})_4(OLa_{1/1}La_{4/4})]$, alternately oriented up and down along [001]. A remarkable detail of the structure is the vacancy □ in the centre of a crown formed by four oxygen atoms (d(□-O) = 278.5 pm) and four lanthanum atoms (d(□-La) = 295.4 pm): $La_9\square Sb_5O_5$.

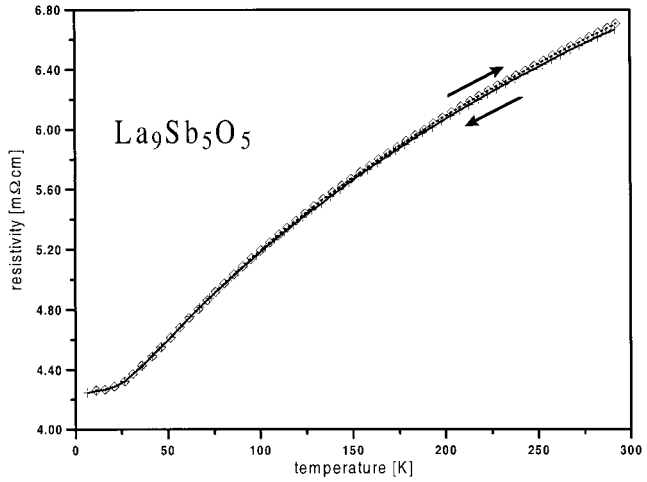

Figure 55: *Temperature dependent resistivity of pressed powder pellets.*

Classical electron counting leads to $(La^{3+})_9(Sb^{3-})_5(O^{2-})_5(2e^-)$. X-ray analysis and electrostatic lattice energy calculations (MAPLE) show, that the vacancy □ is not occupied by, e.g. O^{2-}. However, the larger distances $\bar{d}$(O1-La) compared with $\bar{d}$(O2-La) together with two more electrons available for anion formation, suggested an alternative formula with carbon. The composition $La_9Sb_5O_4C$ would have fulfilled the classical valence rule. But no carbon could be detected by chemical analysis. This obscurity was solved by the measurement of the conductivity. The suboxide $La_9Sb_5O_5$ shows metallic behavior (Fig. 55). A hypothetical $La_9Sb_5O_4C$ should be a semiconductor.

(J. Nuss, W. Hönle, Yu. Grin and H.G. von Schnering)

Electronic structure and chemical bonding in alkaline earth metal subnitrides

Alkaline earth metal subnitrides are structurally and chemically closely related to alkali metal suboxides. The basic units in the crystal structures of the subnitrides are nitrogen-centered M_6 octahedra which may be condensed via common faces into discrete clusters (e.g. $Ba_{14}SrN_6$ clusters in $Na_{22}Ba_{14}SrN_6$) or into Ba_3N chains (in Ba_3N and the quasi-intermetallic phases $NaBa_3N$ and Na_5Ba_3N). Layers built up from edge-sharing M_6N units are encountered in the crystal structures of the M_2N series of compounds where M = Ca, Sr, Ba. As an example, the structure of $NaBa_3N$ is shown in Fig. 56. In view of previous photoemission studies of alkali metal suboxides it was anticipated that the electronic structure of the alkaline earth metal subnitrides is determined by largely ionic bonding between N^{3-} ions and the surrounding partly oxidized alkaline earth metal atoms and a conduction band formed from the various metal orbitals.

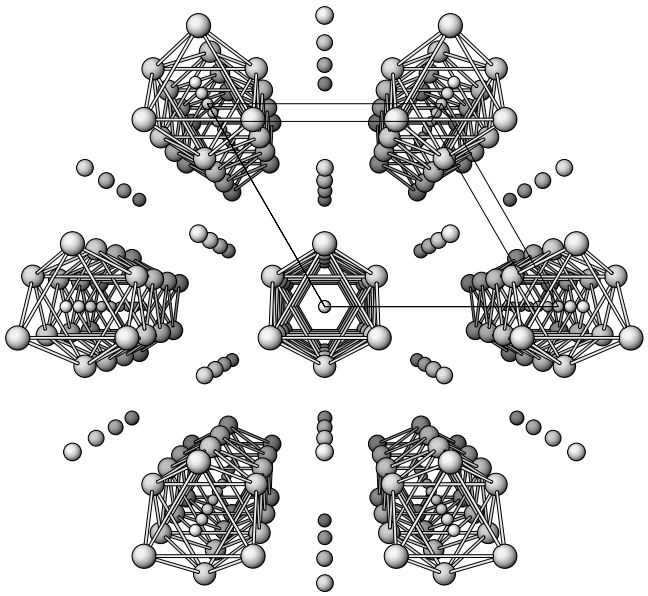

Figure 56: *Projection of the structure of $NaBa_3N$ showing parallel Ba_3N chains with Na atoms inbetween.*

We have studied the electronic structure of the alkaline earth metal subnitrides $Na_{22}Ba_{14}SrN_6$, Na_nBa_3N (n = 0, 1, 5), and M_2N (M = Ca, Sr, Ba) by X-ray and UV photoelectron spectroscopy and LMTO band structure calculations. The HeI valence band spectra of the former two classes of compounds (Fig. 57) reveal quite narrow N-2p bands below the conduction band at small binding energies. The shapes of the N-2p regions in the spectra are in qualitative agreement with the theoretical DOS curves (Fig. 58) where the main fraction of the N-2p states occurs within an energy range of less than 0.2 eV. These results confirm the simple bonding model described above. However, the N-2p regions in the HeI spectra and in the DOS curves of the layered subnitrides M_2N extend over a much broader energy range. Again there is a reasonable agreement between the shapes of the spectra and the DOS curves. In particular, the differences in the shapes of the N-2p regions of Ca_2N, Sr_2N, and Ba_2N are qualitatively reproduced. It is concluded that the broadening of the N-2p bands is due to a more pronounced dispersion in case of the M_2N compounds compared to the Na_nBa_3N series.

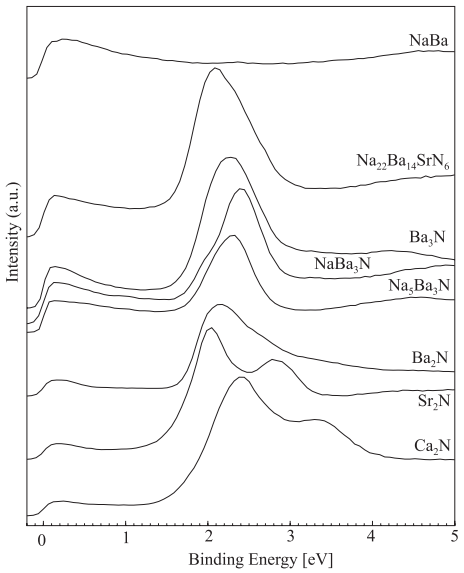

Figure 57: *HeI valence band spectra of various alkaline earth metal subnitrides and, for comparison, of the intermetallic phase NaBa.*

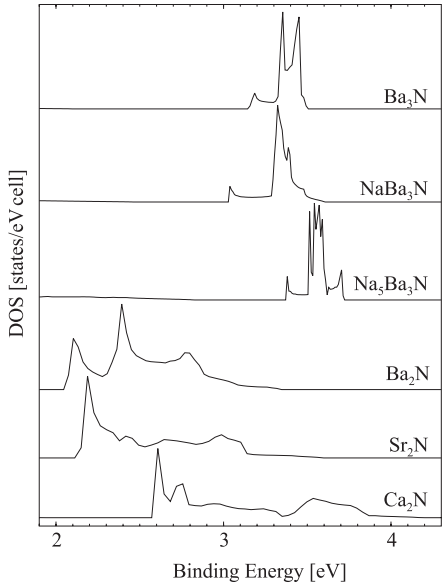

Figure 58: *Density of states (DOS) curves for various alkaline earth metal subnitrides obtained from LMTO band structure calculations.*

A further peculiarity in the valence band spectra of the M_2N series is the observation of bands arising from intra-atomic MXVV and inter-atomic MXV(N)V(N) Auger transitions. In the MXVV Auger process the core hole state X created by photoemission from the shallow M np core level (n = 3, 4, 5 for M = Ca, Sr, Ba, respectively) is refilled by an electron from the conduction band, and a further electron from the conduction band is emitted, whereas in the MXV(N)V(N) process both electrons stem from the N-2p levels.

The Auger bands could be identified in spite of severe overlap with photoelectron bands by comparing spectra measured at different excitation energies and by making use of the shift in shallow core level energies within the series. The two decay channels compete with each other. Interatomic Auger transitions so far have not been observed for the related alkali metal suboxides.

(U. Steinbrenner, P. Adler, W. Hölle and A. Simon)

Pressure-induced structural changes in ternary oxides

In recent years a major advance has been made in the experimental study of crystal structures under high pressure using polycrystalline samples. This is due to the availability of intense, monochromatic, and low-divergence X-ray beams produced at synchrotrons and the introduction of image plate detection systems. Using diamond anvil high pressure cells, powder diffraction patterns from samples of typically 30 μm diameter are obtained in a few minutes. More important, the quality of the patterns often is such that lattice parameters *and* atomic positions can be refined successfully using full profile procedures. We present here two recent examples of high-pressure structural studies of ternary oxides, namely $CuGeO_3$ and $FePO_4$, performed at the ESRF Grenoble.

Interest in the structural properties of $CuGeO_3$ under pressure arises from the recent discovery of a spin-Peierls (SP) transition in this compound and the fact, that the SP transition temperature increases sharply with increasing pressure. SP systems are characterized by a strong correlation of structural and magnetic properties. A general trend under pressure is a suppression of SP transitions due to the increased cost in elastic energy involved in the related structural distortions. Thus, $CuGeO_3$ is an exception. This points to the possibility that the transition is primarily driven by an inherent lattice instability and not by magnetic interactions. For this reason, precise determinations of crystal structure changes at moderate pressures are of great interest.

At ambient conditions, orthorhombic $CuGeO_3$ consists of ribbons of edge-sharing planar CuO_4 units and chains of corner-linked GeO_4 tetrahedra, both oriented parallel to the c-axis. Condensation of the one-dimensional units along the b-axis results in the formation of puckered layers (Fig. 59). These layers are stacked along the a-axis so that the copper coordination remains essentially fourfold, with additional long contacts d_1(Cu–O1) connecting adjacent sheets.

The pressure dependence of lattice parameters reveals that the compressibility of $CuGeO_3$ is highly anisotropic. The softest direction is along the b-axis which is shortened by 8% at a pressure of 6 GPa. The corresponding changes for the a and c axis are only 0.5% and 1.2%, respectively. Within the one-dimensional units, the interatomic distances (Fig. 60 a) and the intrachain bond angle O2–Cu–O2 remain constant within experimental error.

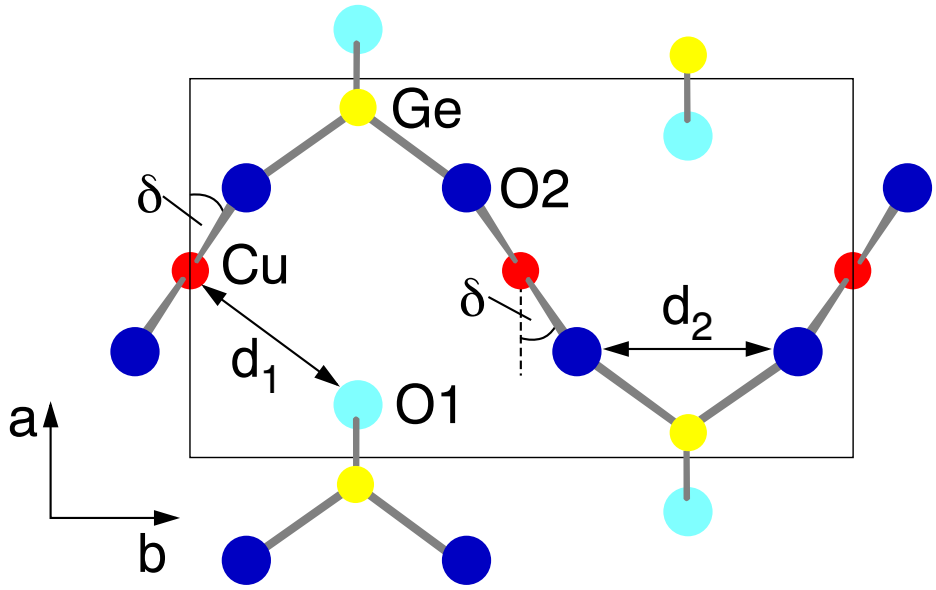

Figure 59: *Projection of the crystal structure of $CuGeO_3$ along the c-axis. Chains of corner-linked GeO_4 tetrahedra and edge-sharing planar CuO_4 units are oriented parallel to the c-axis. Condensation of these units results in puckered layers oriented perpendicular to the a-axis. Labeling of the crystallographic axes corresponds to the non-standard setting Pbmm of space group $Pmma$.*

The major structural effect related to the shortening of the b axis concerns the tilting of the CuO_4 planes towards the c-axis (Fig. 60 b). Associated with the tilting is a significant shortening (–9% at 6 GPa) of the interlayer (Fig. 60 a distances d_1(Cu–O1), but, from point of view of chemical bonding, this effect is not sufficient to change the coordination of Cu ions to a distorted octahedral one.

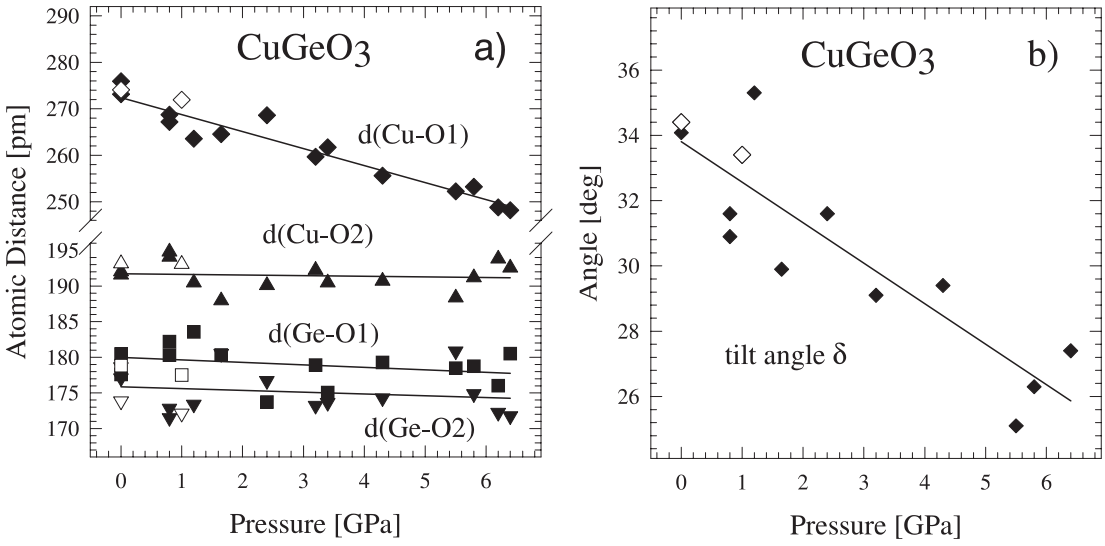

Figure 60: *a) Selected interatomic distances and b) tilt angle of the CuO_4 units towards the c-axis in $CuGeO_3$ as a function of hydrostatic pressure.*

This structural study clearly identifies the orientation of the CuO_4 ribbons as the parameter which is very susceptible to external pressure. Further increase of pressure above 6.5 GPa induces discontinuous structural changes of $CuGeO_3$. With three phases being identified by optical methods, the diffraction patterns are complex mixtures which so far has prevented crystal structure determinations of the high pressure modifications. At pressures above 20 GPa we find indications for a non-reversible amorphization of $CuGeO_3$, a phenomenon observed in several polyhedral structures. In fact, the pressure-driven non-reversible amorphization of α-quartz-type SiO_2 near 20 GPa by Hemley *et al.* in 1988 has stimulated a large number of experimental and theoretical high-pressure studies of ternary oxides with corner-linked tetrahedral framework structures. For instance, berlinite-type $AlPO_4$ was shown to also undergo a pressure-induced amorphization at 15 ± 3 GPa. Unlike silica, the crystalline phase is retrieved upon pressure release, a phenomenon called structural memory.

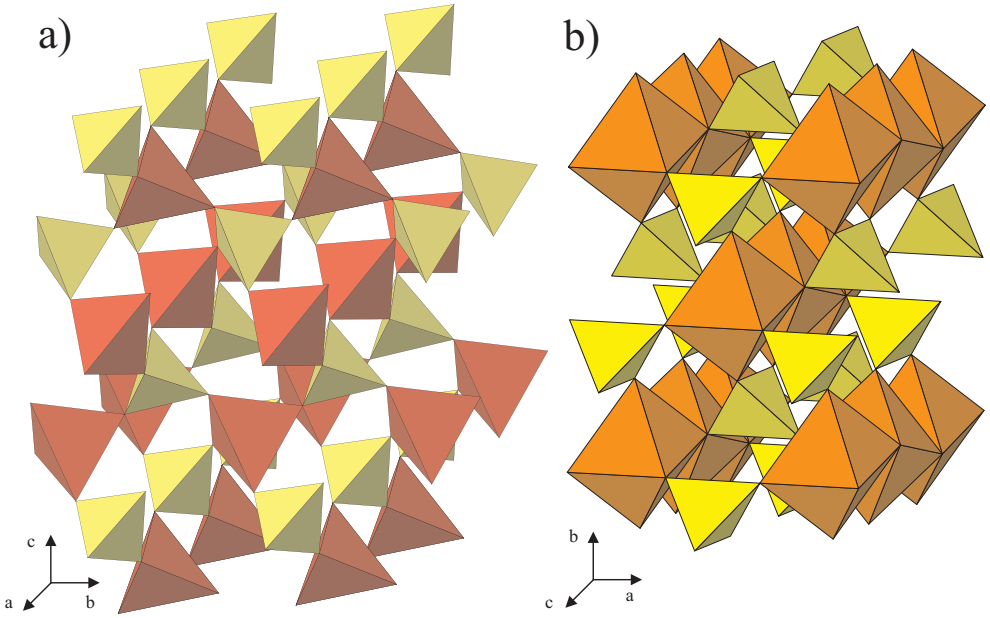

Figure 61: *Crystal structures of $FePO_4$: a) trigonal berlinite-type low-pressure modification and b) orthorhombic $CrVO_4$-type high-pressure phase. Red or orange polyhedra are centered by iron, yellow tetrahedra contain phosphorus.*

The compound $FePO_4$ is isotypic to $AlPO_4$ at ambient conditions, with both Fe^{III} and P^V in fourfold coordination (Fig. 61 a). As a new phenomenon we have observed for $FePO_4$ the *concurrent* transformation to a new crystalline and an amorphous phase with about equal abundance of the two components. The transition pressure is as low as 2.5 GPa, where the conditions are fully hydrostatic. This means that the amorphous component is generated under fully hydrostatic conditions, ruling out external shear stress as the possible origin for partial amorphization. The amorphous modification was further characterized by Raman scattering experiments and, in cooperation with the group of M. Pasternak at Tel Aviv University, by Mössbauer spectroscopy. Here, we focus on the crystalline high-pressure modification of $FePO_4$.

The X-ray diffraction patterns can be indexed in the orthorhombic crystal system. Based on calculated diffraction patterns, the crystal structure is assigned as $CrVO_4$-type (space group Cmcm). The specific volume of this orthorhombic phase is 21.0(5)% smaller than that of the berlinite-type modification. In the high-pressure phase (Fig. 61 b), iron atoms occupy centers of edge-sharing octahedra which form chains oriented parallel to the c-axis. These chains are interconnected by PO_4 tetrahedra, thus forming a 3D framework structure. The pressure-induced structural phase transition causes a selective increase of the iron coordination number from four to six whereas phosphorus aquires a fourfold coordination in both phases. The observation of a $CrVO_4$-type high-pressure phase of a berlinite-type compound suggests to search for mixed-coordination high-pressure phases of other berlinite-type compounds and to explore the possible role of a hidden polymorphic transition in the structural memory effect of amorphous modifications.

(U. Schwarz, T. Zhou, M. Hanfland, S. Bräuninger and K. Syassen)

Measurement of free exciton dephasing rate in GaN on sapphire by degenerate four-wave-mixing

Recent progress in material growth and device fabrication have brought much interest in the research of the basic properties of GaN. The coupling strength of an elementary excitation to external reservoirs can be characterized by its energy decay time T_1, and its dephasing time T_2. Degenerate four-wave mixing (DFWM) is a powerful technique that allows the direct measurement of T_2 of a transition. For a homogeneous (inhomogeneous) transition, the decay time of the DFWM signal T_d, is directly related to the dephasing time by $T_d = T_2/2$ ($T_d = T_2/4$). We report here direct measurement of exciton dephasing time T_2, of two samples of GaN on sapphire grown by two independent research groups by the MOCVD method for different excitation density and temperature. The FWHM photoluminescence linewidths of the A exciton are 2.5 meV and 4.1 meV for sample 1 and 2, suggesting that the transitions are inhomogeneously broadened.

Figure 62 a shows the typical DFWM trace of sample 1 for different excitation wavelengths and an excitation density of $4 \times 10^{16}\,\mathrm{cm}^{-3}$. The corresponding spectrum of the DFWM signal measured using lock-in techniques are given in Fig. 62 b. As the laser is tuned from below the A exciton line at 3.4942 eV to the B exciton line at 3.5022 eV, we observe a transition from monoexponential decay to quantum beating between the A and B excitons. The beating period of 500 fs (8.2 meV) is exactly the energy difference between the A and B excitons. By tuning the laser 5 meV below the A exciton line at 3.4892 eV, we excite predominately the A exciton and the decay rate of the DFWM signal gives directly the dephasing time of the A exciton. The homogeneous linewidth of the free exciton to first order can be described by the relation

$$\Gamma(N,T) = \Gamma(0,0) + \beta_{ph} T + \beta_{xx} a_B^3 E_B N \ , \qquad (17)$$

where N is the density, T is the temperature, $a_B = 3.6$ nm is the A exciton Bohr radius and $E_B = 20$ meV is the A exciton binding energy. The coefficient β_{xx} is a dimensionless parameter which measures the strength of the exciton-exciton scattering, whereas the coefficient β_{ph} is a parameter which measures the exciton-acoustic-phonon interaction. For a fixed temperature, a least square fit to Eq. (17) is done for data taken at different densities, providing the value $\Gamma(0,T)$ at each temperature.

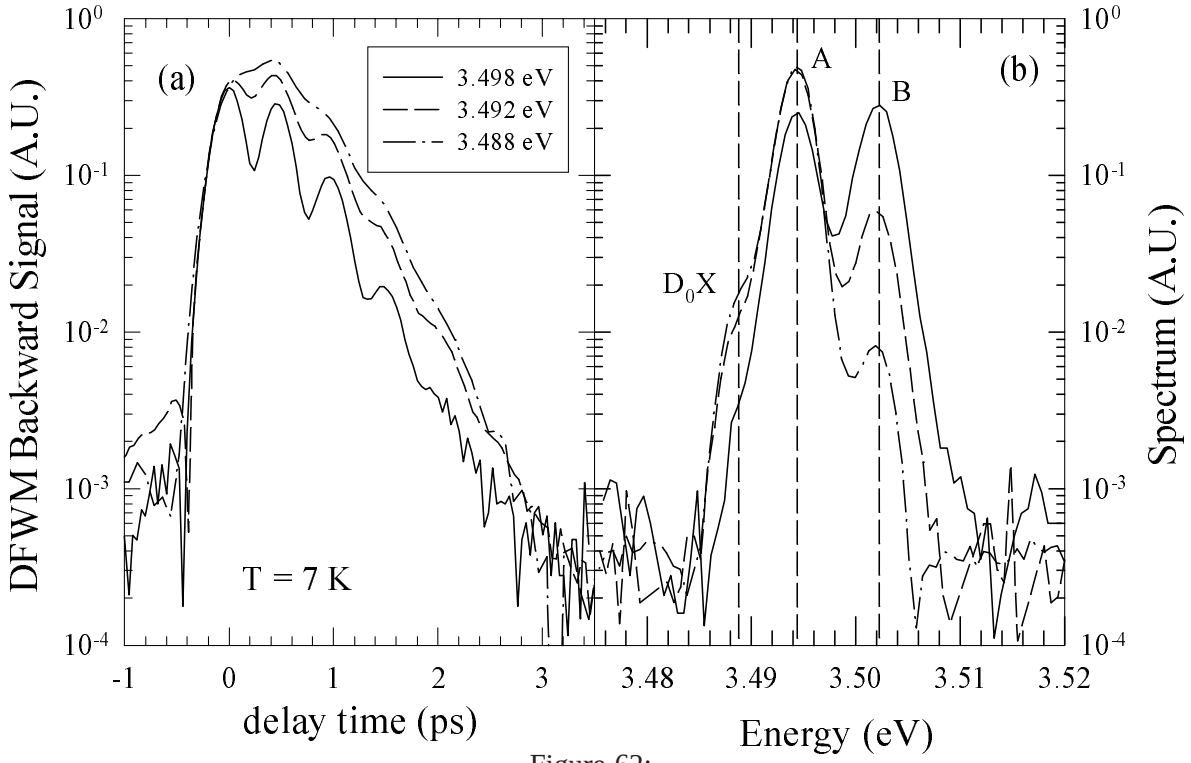

Figure 62:

The resulting zero density linewidths, $\Gamma(0,T)$, are plotted in Fig. 63, allowing us to determine the value of β_{ph}. The linewidth as a function of excitation density at 10 K is also shown in Fig. 63. The results for the two samples are tabulated in Table 6. Experimental values of bulk GaAs are shown for comparison. Note that the linewidth is related to the dephasing by $\Gamma_h = h/\pi T_2$. The theoretical value of β_{ph} is slightly smaller than our observed value and the deviation is attributed to the lack of accurate knowledge of the GaN deformation potentials and to additional scattering by free carriers at high temperatures. The free carrier density is expected to increase with increasing temperature. Remarkably, the exciton-phonon scattering rate is about the same for the two samples. A comparison of the linewidth between the two samples shows that the measured β-parameters are sample independent and we believe our results give an accurate value of the intrinsic exciton dephasing time in GaN. The residual linewidth of the exciton, $\Gamma(0,0) \sim 4$ ps, is caused predominately by exciton-impurity scattering.

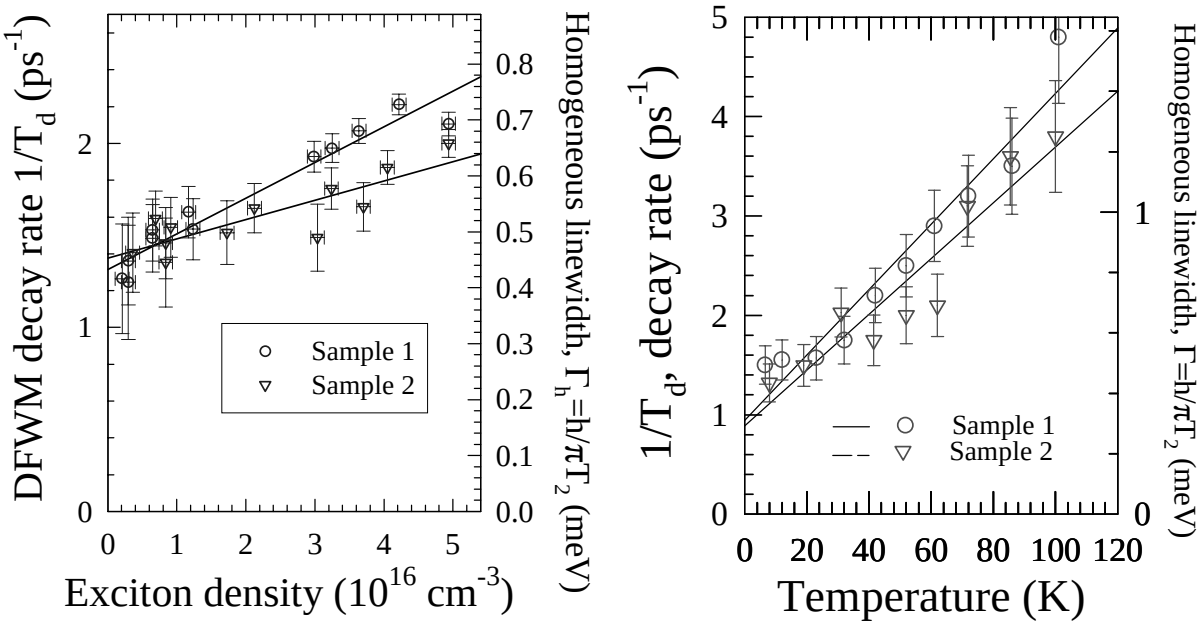

Figure 63:

The material parameters of GaAs are also listed in Table 6 and are similar to that of GaN, provided that the exciton-exciton scattering coefficients is normalized with respect to the exciton binding energy and Bohr-radius as shown in Eq. (17).

Table 5. *Results of scattering coefficients and linewidth of DFWM.*

	$\Gamma(0,0)$ in meV (T_2)	β_{ph} (μeV/K)	$\Gamma(0, T = 10\text{ K})$ in meV (T_2)	β_{xx}
GaN, Sample 1	0.29 (4.5 ps)	9	0.43 (3.1 ps)	6.8
GaN, Sample 2	0.31 (4.2 ps)	11	0.52 (2.5 ps)	5.1
theory (wurtzite)	—	7	—	—
GaAs	0.18 (7.3 ps)	17	—	10

For our samples of interest, the ratio of inhomogeneous to homogeneous linewidth at low density is ≈ 10, and experimentally the observed DFWM is essentially mono-exponential. Based on these results, we relate the experimental DFWM decay time to the dephasing time by $T_d = T_2/4$ in our experimental analysis, although one would expect that the homogeneous linewidth will become comparable to the inhomogeneous linewidth at high excitation density due to collision broadening of the exciton line. When the inhomogeneous linewidth is comparable to the homogeneous linewidth of the transition, the DFWM decay can be described by a biexponential with an initial decay time of $T_2/2$ and a subsequent decay time of $T_2/4$. The homogeneous linewidth for the highest excitation density ($\approx 5 \times 10^{16}$ cm^{-3}) in our experiment is about 0.8 meV which is several times smaller than the inhomogeneous linewidth. Hence, we expect that $T_d = T_2/4$ is a good approximation in our experiment.

(S. Pau, J. Kuhl, F. Scholz, V. Haerle, M.A. Khan and C.J. Sun)

Extraordinarily high proton conductivity in water-containing barium yttrium stannate ($Ba_2YSnO_{5.5}$)

Many acceptor doped oxides incorporate more or less water by dissociative absorption, which leads to the formation of protonic defects (formation of internal OH-groups) and hence to proton conductivity. However, the development of proton conducting oxides appropriate for electrochemical applications such as fuel cells is complicated by the conflict between high proton conductivity with high proton transference number and chemical and electrochemical stability. So far, acceptor doped $BaCeO_3$ is the benchmark material with respect to proton conductivity, but below $\approx 700^\circ$ it is not stable in air with respect to carbonate formation. Acceptor doped $CaZrO_3$, on the other hand, is very stable, but the low proton conductivity of this material allows only for its use in low drain applications such as potentiometric hydrogen sensors. It is therefore a challenge to find oxides, which combine high water solubility and high mobility of protonic defects on one side and high chemical and electrochemical stability on the other.

One possible strategy that can be followed to achieve these features is to simultaneously optimize the required materials properties. Such a strategy is promising especially when the mutual dependencies of the relevant properties can be expressed in terms of the same structural, chemical and dynamical parameters. Along this line, a recent analysis of available data on oxides with perovskite related structures provided the following guidelines for the composition of perovskites (ABO_3) with high proton conductivity and good stability: (i) The occupation of the A-site does not require much of a compromise. Except for the stability with acidic gases, which is almost independent of the choice of the A-cation, all relevant properties are superior for an A-site occupation by barium compared to other alkaline earth ions. (ii) The choice of the B-cation, however, does require some compromising. It should be of medium size with an amphoteric nature and should form no significant directional (covalent) bonding with its oxygen ligands. Small B-cations reduce water solubility, whereas large B-cations reduce thermodynamic stability. The occupation of the B-site with different ions of different acid/base properties is expected to further increase the thermodynamic stability.

All these features are met by $Ba_2SnYO_{5.5}$, a phase which was first reported as an impurity phase in the yttrium barium copper tin oxide system. It is reported to stabilize in a perovskite-type structure with a doubled unit cell ($a = 844$ pm) due to an ordering of the Y and Sn on the B-site. Despite the high concentration of oxygen ion vacancies (25 mol%), the cubic symmetry of the perovskite structure is retained. Both features are anticipated to be additional prerequisites for the formation of a high concentration of protonic defects in water containing atmospheres. Indeed, an extraordinarily high water solubility is observed in the water absorption isobar shown in Fig. 64 together with that of 20% Y-doped $BaCeO_3$.

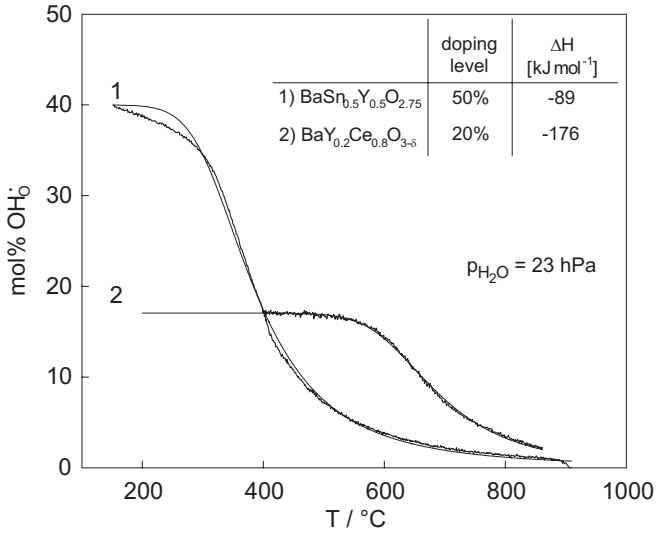

Figure 64: *Water absorption isobars (p_{H_2O}=23 hPa) for $Ba_2SnYO_{5.5}$ and 20% Y-doped $BaCeO_3$.*

According to the lower basicity of the stannate compared to the cerate, the hydration enthalpy is less negative corresponding to a lower hydration temperature, but the solubility limit of 40 mol% is the highest observed for any oxide. The high water solubility (composition ranges from $Ba_2YSnO_{5.5}$ to $Ba_2YSnO_{5.1}(OH)_{0.8}$) and the high mobility of protonic defects result in a proton conductivity, which is below about 500°, even higher than that of $BaCeO_3$-based oxides (Fig. 65).

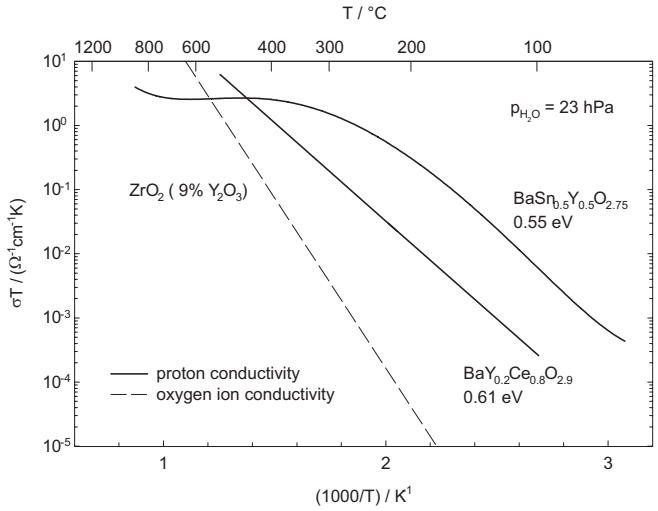

Figure 65: *Proton conductivity of $Ba_2SnYO_{5.5}$ and 20% Y-doped $BaCeO_3$ in wet nitrogen. The oxide ion conductivity of yttria stabilized zirconia (YSZ) is shown for comparison.*

Since proton conductivity is frequently higher than oxide ion conductivity in this temperature range (Fig. 65), proton conducting oxides have frequently been suggested as a substitute for Y-stabilized zirconia (YSZ) as separator material in medium temperature fuel cells. Although the presented stannate has proved to exhibit the required high proton conductivity and thermodynamic stability in air, the transformation of the perovskite to the brownmillerite structure under strongly reducing conditions prevents this oxide from being used in fuel cells. It, however, appears to be very promising for electrochemical applications such as electrochemical sensors operating under oxidizing conditions.

(T. He, K.D. Kreuer, J. Maier and P. Murugaraj; T. Schober (KFA Jülich))

The influence of the microstructure on the impedance of ceramics studied by finite element calculations

Polycrystalline solids do not only exhibit a structure on the atomistic scale but also a kind of super-structure on a much larger scale determined by the grain boundary network. In polycrystalline solid electrolytes as employed in solid oxide fuel cells, sensors or electrochemical filters, these grain boundaries can influence and even determine the electrical properties of such devices. In many ionic polycrystalline semiconductors as utilized, e.g. in varistors, capacitors or sensors this is similarly valid. Thus, an analysis of the electrical properties of grain boundaries is often required. In the case of highly resistive grain boundaries impedance spectroscopy offers a possibility for a deconvolution of grain interior and grain boundary contributions: The different relaxation times of grain boundary and bulk migration processes frequently yield two well separated semicircles in the complex impedance plane. The analysis of such impedance spectra requires a model to parameterize and interpret the raw data. Owing to the high symmetry and the simplicity of the grain shape the brick layer model (Fig. 66 a) is usually used for such an investigation.

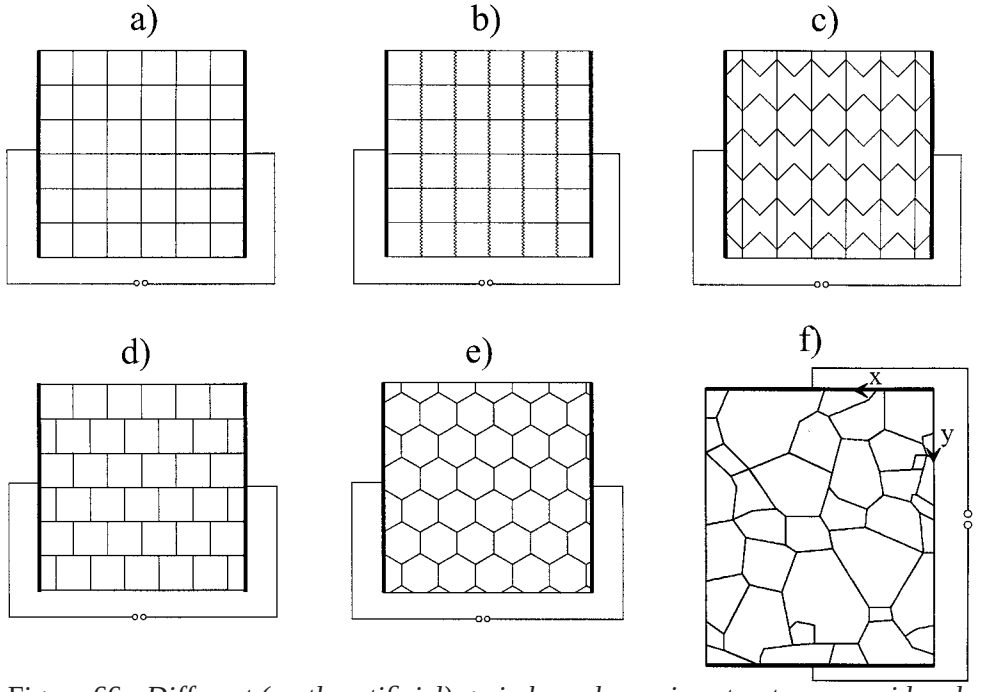

Figure 66: *Different (partly artificial) grain boundary microstructures considered.*

Analytical results can be given for it, including both blocking and short-circuiting pathways, and we could show that and how space charge effects can be taken into account in the overall analysis.

However, in real systems i) the grains are neither cubic and of constant size nor is the microstructure of a simple symmetry, in addition ii) the geometrical and electrical properties of the grain boundaries may vary substantially even within the same sample. Furthermore faceted grain boundaries are frequently met in contrast to the straight grain contacts

assumed in the brick layer model. Thus the latter appears to be a relatively crude simplification of the real situation and one may ask in how far the values calculated using this model are reliable. In this study we restrict to low and homogeneously conducting boundaries.

The validity and some limits of the brick layer model with low conducting grain boundaries are tested by systematically modifying the microstructure (Fig. 66) and computing the spectra using two-dimensional finite element calculations: Laplace's equation is solved numerically and the impedance is calculated via integration over the current density. The thin grain boundaries which usually would require a very dense mesh in finite element calculations are taken into account by so-called interfacial line elements. This allows a significant reduction of the node density in sample regions close to the grain boundaries. Symmetry considerations are used to reduce the size of the 'generating element' of the microstructure. Conductivity and thickness of the grain boundaries are assumed to be constant. Besides the fact that we obtain quantitative numerical results two major 'rules of thumbs' are extracted characterizing the deviations from the brick layer impedance:

i) If it is 'unavoidable' to pass a grain boundary, the current spreads over a large grain boundary length thus lowering the overall resistance. This leads to the consequence that in some patterns – and in this is a contrast to the brick layer model – an increased insulating grain boundary length and volume fraction can facilitate the overall transport, which may be counter-intuitive at a first glance. In such cases – as realized in ceramics with faceted grain boundaries – the brick layer model would overestimate the grain boundary conductivity.

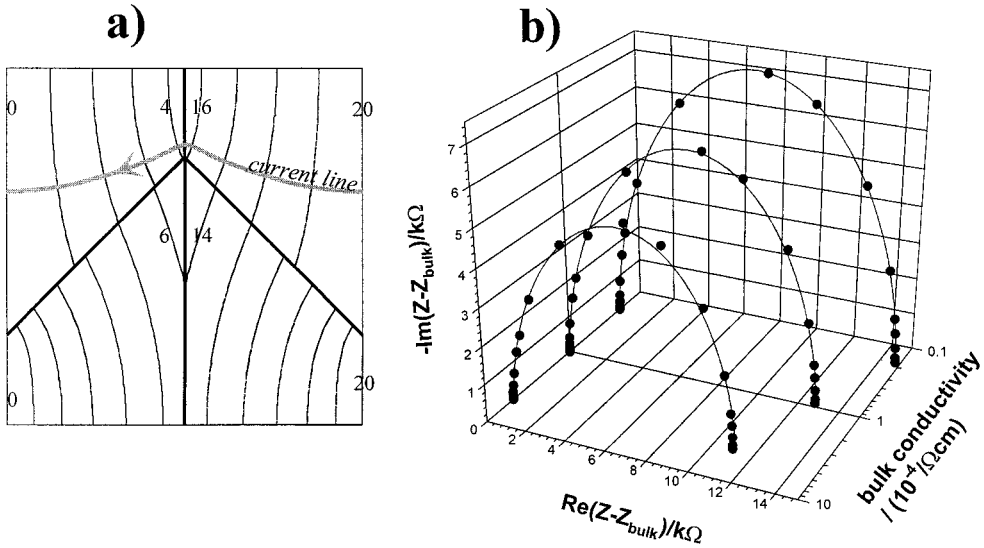

Figure 67: *a) DC-potential distribution and one current line in a basic element of the microstructure of Fig. 66 c). The numbers at the equipotential lines indicate the potential in mV. b) Impedance spectra for different bulk conductivities highlight their influence on the 'grain boundary semicircle'. The bulk impedance (first semicircle) was subtracted in all cases.*

ii) If grain boundaries can be avoided, the current lines make detours around the hindrance. In Fig. 67 a this is shown for the basic element of a bent grain boundary pattern (Fig. 66 c). This leads to another important feature of the microstructures considered: The detours are obviously made more and more difficult if the bulk conductivity is lowered. Hence, the low-frequency semicircle of the impedance spectrum, which is usually exclusively interpreted in terms of grain boundary properties, is influenced by properties of the grain interior (Fig. 67 b). The finite element calculations led to a quantification of these interrelations. 'Detour-effects' can play an important role in real ceramics, especially if broad grain size distributions exist or if the grain size distribution is spatially inhomogeneous. Another important feature of such conductivity-dependent current lines are non-ideal, i.e. depressed second semicircles in the complex impedance plane (grain boundary semicircle).

Displacing the rows of square grains (Fig. 66 d) represents a kind of an intermediate of the two cases considered: Parts of the current make detours to achieve a larger grain boundary length again leading to an inhomogeneous potential distribution and a decrease of the resistance compared to the brick layer model. Nonetheless, in various cases the brick layer model turns out to allow at least satisfying estimates of the grain boundary properties. This is exemplarily demonstrated for the pattern in Fig. 66 f which is deduced from the SEM-image of a real microstructure. The 'true' impedance as calculated from the potential distribution (Fig. 68) was analyzed using the brick layer model. This analysis leads to conductivities and permittivities which differ less than 10% from the 'true' parameters used in the finite element calculation, showing that different effects which enhance or lower the impedance, partially compensate.

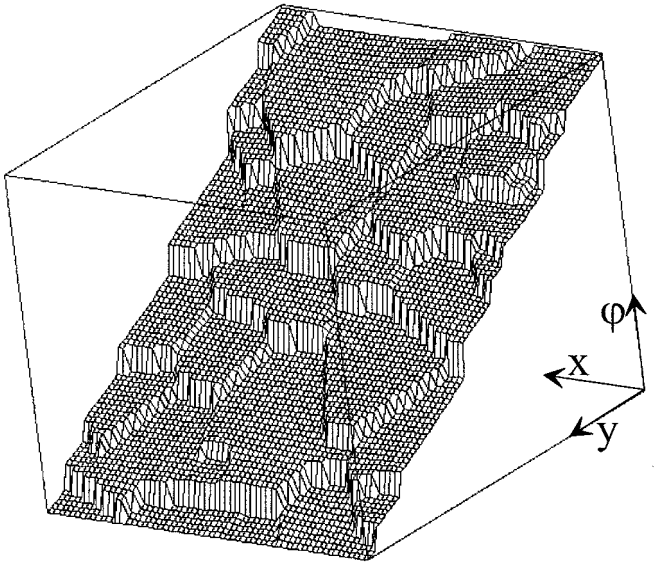

Figure 68: *DC-potential distribution in the 'realistic' grain boundary pattern of Fig. 66 f).*

Other calculations for patterns with regular polygons (hexagons, squares and triangles) revealed only slight differences as well. The hexagonal pattern (Fig. 66 e) turns out to be the regular polygon pattern with the lowest resistance. However, a difference of less than 10% between the grain boundary resistance of the brick layer model and of the hexagonal equilibrium pattern again demonstrates that the brick layer model can be regarded as a reasonable model in many cases. Our finite element calculations also allows us to predict the cases in which it fails significantly and how to handle such situations.

(J. Fleig and J. Maier)

The significance of a cube root law for charge carrier interactions evidenced by MD and MC simulations on β-AgI

The thermodynamics of ionic charge carriers in crystals is fairly well established if the defects are dilute. At higher concentrations defect interactions and site restriction effects occur that are much more difficult to handle. The latter can be partly taken into account by replacing Maxwell-Boltzmann statistics (MB) by the more accurate Fermi-Dirac type of statistics. Short-range order effects can sometimes be described by introducing associates that are in thermodynamic equilibrium with the free defects. In that case the introduction of activity coefficients can be avoided. They are, however, indispensable for long-range order.

A typical situation in which long-range order effects must become pronounced is found in the silver halides at higher temperatures. There an anomalous increase of the ionic conductivity is observed, usually preceding a phase transition to a partially or totally molten state. The concentration can be as high as a few percent. The well-known Debye-Hückel screening effects (leading to excess chemical potentials μ_{ex} (logarithm of activity coefficient), being essentially proportional to the square root of the defect concentration, are no longer sufficient to explain the behavior. Hainovsky and Maier (1995) could quantitatively describe the anomalous conductivity increase, and partly also the phase transition behavior for a variety of ionic conductors (exhibiting melting transitions, first order and higher order sublattice melting) by introducing a cube root law

$$\mu_{ex} = -Jc^{1/3} \tag{18}$$

into a chemical potential $\mu = \mu_{MB} + \mu_{ex}$ which can be interpreted in terms of a topological ordering leading to a quasi-Madelung energy of the effective superlattice formed by the defects. Since the mean distances of the defect and perfect lattices scale with $c^{1/3}$, J was assessed to be

$$J \sim 2/3\frac{U_m}{\epsilon} \, . \tag{19}$$

(U_m: Madelung energy of the perfect lattice, ϵ: dielectric constant). For the ionic conductors of interest the Frenkel enthalpy is empirically given by 1.3 U_m/ϵ leading to a J-value which is about half the Frenkel enthalpy. In this paper we tackle the problem by MD simulations concentrating on β-AgI as the example, for which we use the well-working empirical potential published by Parrinello, Rahman and Vashishta (1989). We classify the Ag-ions as regular ions and defects and compute the concentration of defects as a function of temperature starting from the low temperature β-phase. In the β-phase defective Ag-ions can occupy either tetrahedral positions, which are empty in the ground state structure, or octahedral positions. Therefore we have to take account of two defect equilibria and a slightly more complicated electro-neutrality equation which is, however, not of fundamental interest in this context.

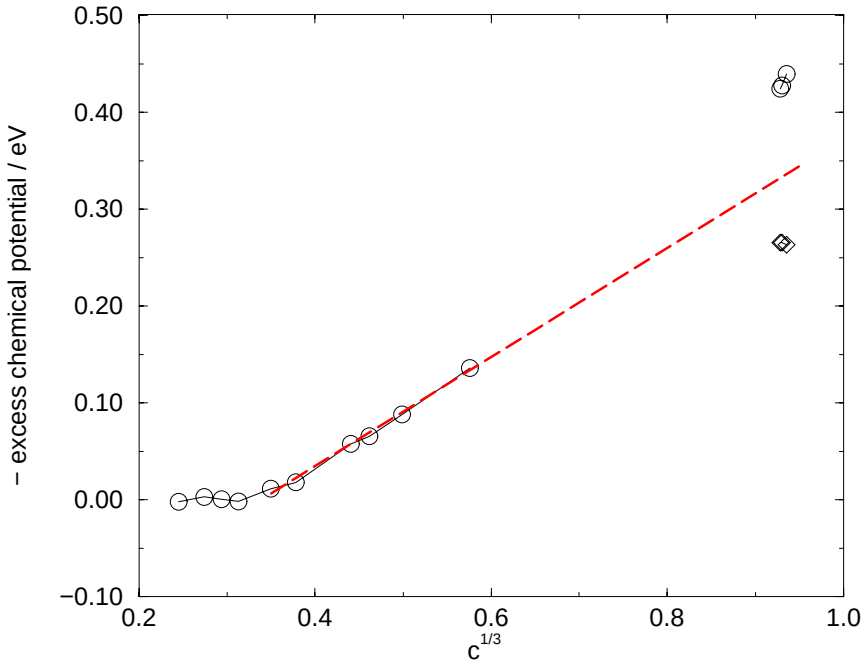

Figure 69: *Excess part of the chemical potential of the defects as a function of the molar fraction $c^{1/3}$. For the value referring to extremely high concentrations the difference between Maxwell-Boltzmann (diamonds) and Fermi-Dirac type (circles) statistics derived from the concentration distribution is of great importance. Since we excluded specific interactions the latter overestimates site restriction effects while the former ignores them.*

In Fig. 69 we plot the excess of the total concentration of defects over the Boltzmann values. It is obvious that a cube root law is indeed a good description for high concentrations. The slope is in agreement with the J-value (≈ 0.5 eV) derived from experiments and the one assessed from U_m and ϵ. For the purpose of a better check of the cube root model and its underlying basis we calculate energy contributions of the defects, including their interaction energies with the use of classical MC simulations. Plotting the excess energy as a function of $c^{1/3}$ (Fig. 70) we again find a cube root-like behavior, again with a J-value close to 0.5 eV.

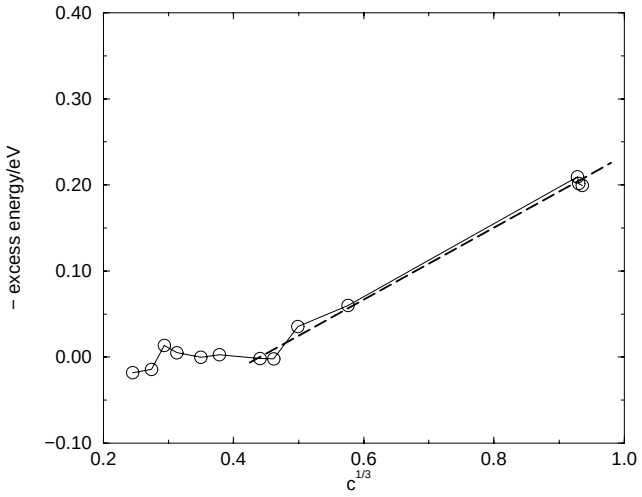

Figure 70: *Excess energy of the defects as a function of* $c^{1/3}$.

From the MD simulation data we can conclude that for all temperatures the defective Ag-ions which occupy the octahedral positions of the iodine sublattice are the ones which are responsible for the diffusion. Therefore we can rule out that the premelting phenomenon stems from the significants of two defect types, one dominating at low and the other dominating at high temperatures. In conclusion, the results of the static as well as of the dynamic simulations of β-AgI support the cube root model.

(F. Zimmer, J. Maier, P. Ballone and M. Parrinello)

Specific heat of 3d transition metal boracites

The large boracite family $T_3B_7O_{13}X$ (where T stands for a bivalent transition metal ion or Mg and X for F, Cl, Br, I, OH or NO_3) derives from the crystal structure of the mineral boracite $Mg_3B_7O_{13}Cl$. Many members of this family are of particular interest due to the occurence of simultaneously ferroelectric/ferroelastic, weakly ferromagnetic phases (multiferroic phases). All boracites share the same high temperature cubic structure with point group $\bar{4}$3m1'. Depending on the metal T and on X various sequences of symmetry lowering phase transitions occur with decreasing temperature. These subtle structural changes lead to orthorhombic or rhombohedral ferroelectric/ferroelastic phases in which the magnetic ordering of 3d ions takes place.

Here we have studied the magnetic ordering of a large number of boracites (T = Cr, Mn, Fe, Co, Ni, Cu, Zn; X = Cl, Br, I) by specific heat measurements between 2 K and 100 K (some up to 320 K). These data complement magnetic susceptibility, dielectric permittivity, electrical polarization, magnetic birefringence, magnetoelectric effect, and recent neutron diffraction investigations.

Below 200 K all investigated boracites are fully ferroelectric/fully ferroelastic (except Cu-Br and Cr-I). Most T-X boracites order partially or fully ferromagnetic at low temperatures. This leads to a further reduction of the symmetry to point groups in the orthorhombic or monoclinic system. The investigation of the magnetic ordered state on single crystals is complicated due to the presence of ferroelectric, ferroelastic and ferromagnetic domains.

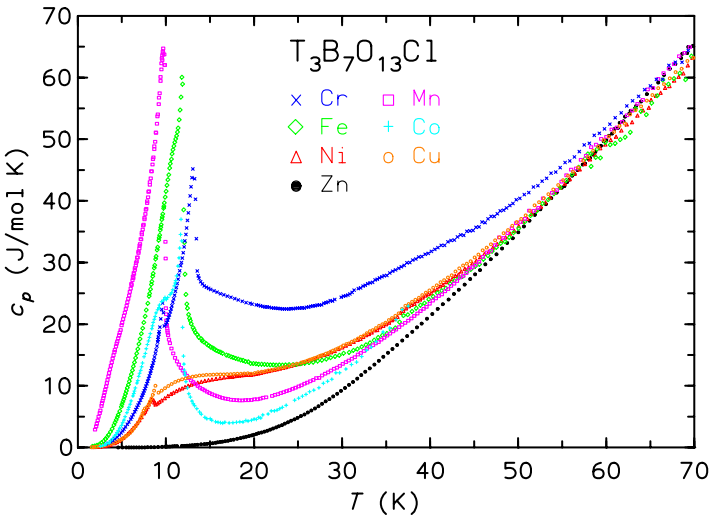

Figure 71: *Specific heat $c_p(T)$ of several 3d transition metal chlorine boracites.*

A part of our results, the specific heats of 3d metal chlorine boracites, are presented in Fig. 71. The non magnetic Zn-Cl boracite serves as a reference material for the phononic contributions to the specific heat. Due to the low mass of the constituting atoms the Debye temperatures of the boracites are high (equivalent Θ_D of Zn-Cl boracite between 30 K and 100 K ranges from 510 K to 700 K) and the lattice contributions are thus small below 100 K.

Judging from the shape of the transition peaks different types of magnetic ordering are found in this series. While the orthorhombic Mn-Cl displays a lambda transition typical for 3D ordering, the rhombohedral Fe-Cl and Co-Cl compounds show shoulders at the flank of the transition. In the Co-Br and Co-I boracites clear additional phase transitions are observed as broad peaks in the specific heat at $\approx 0.5\,T_C$. This behavior hints for a continuous spin reorientation. For Co-Br the spin structure was determined by neutron diffraction. The weakly ferromagnetic order transforms at lowering the temperature to a 3D canted structure. In Cr-Cl two magnetic transitions are observed. The upper one corresponds to antiferromagnetic ordering, the lower one to the transition to a partial ferromagnetic phase.

The magnetic entropies, obtained after subtraction of the Zn-Cl reference, give information on the magnetic ground state of the 3d ions. In the T-Cl boracites we find the usual ground states for Cr^{2+} and Fe^{2+} ($S = 2$) and Mn^{2+} ($S = 5/2$). Due to large spin-orbit coupling the magnetic ground state in Co-Cl is a doublet and the ion is an effective spin $1/2$ system for temperatures near T_C. In Ni-Cl the ground state is also a doublet as in the 'real' spin $1/2$ system Cu-Cl.

The orthorhombic Ni-Cl and Cu-Cl have only small transition peaks in the specific heat at T_C. The magnetic specific heats of the latter are dominated by broad anomalies similar to spin 1/2 Schottky anomalies with energy splittings of 39 K for Ni-Cl and 33 K for Cu-Cl. These anomalies may originate from low-dimensional Ising ordering, dimeric short range order, or from crystal field effects. For both compounds the entropy at T_C is only $\approx 15\%$ of $R \ln 2$; a very low percentage giving credence to the first interpretation.

Pronounced magnetic short range order correlations extend to sizeable temperatures ($\approx 65\,\mathrm{K} = 5\,T_C$) also in Cr-Cl. The experimental situation is similar to the one found in Cr-Br boracite and in most iodine boracites T-I. A general trend for increasing ordering temperatures in going from the T-Cl via the T-Br to the T-I series compounds is observed.

In the Co-X, Fe-Cl and Fe-Br boracites additional phase transitions below T_C are observed. While in Co-Br and Co-I pronounced broad peaks appear at $\approx 0.5\,T_C$, shoulders at the lower temperature flanks of the peaks of Co-Cl, and of Fe-Br and Fe-Cl (much weaker) are found. In the paraelectric cubic Cr-Br and Cr-I boracites new transitions (presumably magnetic ordering of Cr^{2+}) were found by specific heat to occur at 14.5 K and 52.0 K, respectively. Both transitions are only weakly influenced by magnetic fields of 14 T, however, a well defined T^3-dependence of the excess specific heat below the phase transition in Cr-Br boracite hints for the presence of spin-waves, i.e. anti-ferromagnetic correlations.

(W. Schnelle and E. Gmelin; O. Crottaz and H. Schmid (University of Geneva))

Heat resistance of solid-to-solid interfaces at sub-ambient temperatures

Solid surfaces are composed of microscopic peaks and valleys of varying size and shape that form a three-dimensional bizarre landscape. The uneveness of any real surface is the basic cause of the thermal contact-resistance R_{Th}. The heat Q, transferred between two mechanically jointed surfaces with the geometrical area A_G, is constricted to a limited number of discrete points which constitute only 0.1–0.01% of A_G. Consequently, a drop of temperature ΔT resulting in a thermal boundary resistance R_{Th} per unit area (or heat conductance $\kappa_{Th} = R_{Th}^{-1}$, respectively) appears across the interface:

$$R_{Th} = \frac{1}{\kappa_{Th}} = \frac{\Delta T}{(Q/A_G)} \qquad [\mathrm{Km^2W^{-1}}]$$

The reduction and optimization of R_{Th} between similar and dissimilar materials, however, is of fundamental importance for many technical applications and scientific experiments, e.g. car engines, nuclear power stations, cooking plates, low temperature equipment, thermal insulation, etc.. The heat contact-resistance may vary by a factor of 10^6 or more when the thermophysical properties of the contact materials are modified, the topography

of the surfaces is changed and/or an appropriate interlayered material (so-called interposer) is applied, e.g. oil, grease, soft metals, which in general considerably improve the heat conductance.

The process of heat transfer across interfaces is a very complex problem for which no comprehensive theory exists. Reliable data for applications are nearly exclusively established experimentally. Most of the data known from literature display a large scatter (10–100%) and poor reproducibility due to the numerous parameters involved in such experiments. These parameters influence and affect the results in a sensitive and complex manner by:

- Contact material used and its purity, temperature, pressure, shape, microstructure (grain-size, defect concentration, etc.) of the contact,
  surface roughness, flatness, strain, preparation (e.g. polishing, sandblasting, corrosive layers),
  external conditions as air, absorbed gases, humidity or vacuum;
- rate of total heat flux, heat flux direction, temperature gradient, and
- experimental difficulties as the temperature determination of the surfaces, radiative heat loss, heat pulse experiments.

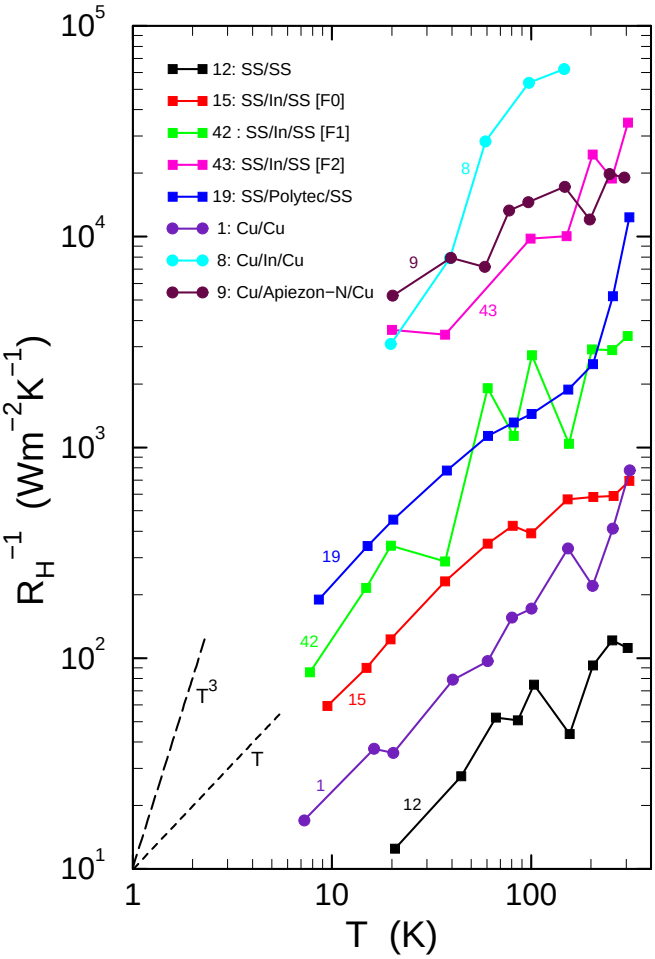

Figure 72: *Heat conductance as a function of temperature for various types of mechanically made contacts as labelled in the figure.*

Few systematic studies have been reported and the majority of results refer to room temperature experiments or measurements below 4 K. Very few data cover the wide temperature range from 10 K to 300 K (see Fig. 72). It was the purpose of this study to fill, at least partially, the gap of lacking data by measuring various combinations (labelled as material1/interposer/material2; SS = stainless steel): SS/SS, Cu/Cu, SS/In/SS, Cu/In/Cu, Cu/Apiezon-N/Cu, etc.. This study can be regarded as the most comprehensive one and enables to estimate much better any unknown heat resistance, in particular in the intermediate temperature range from 10 K to 300 K.

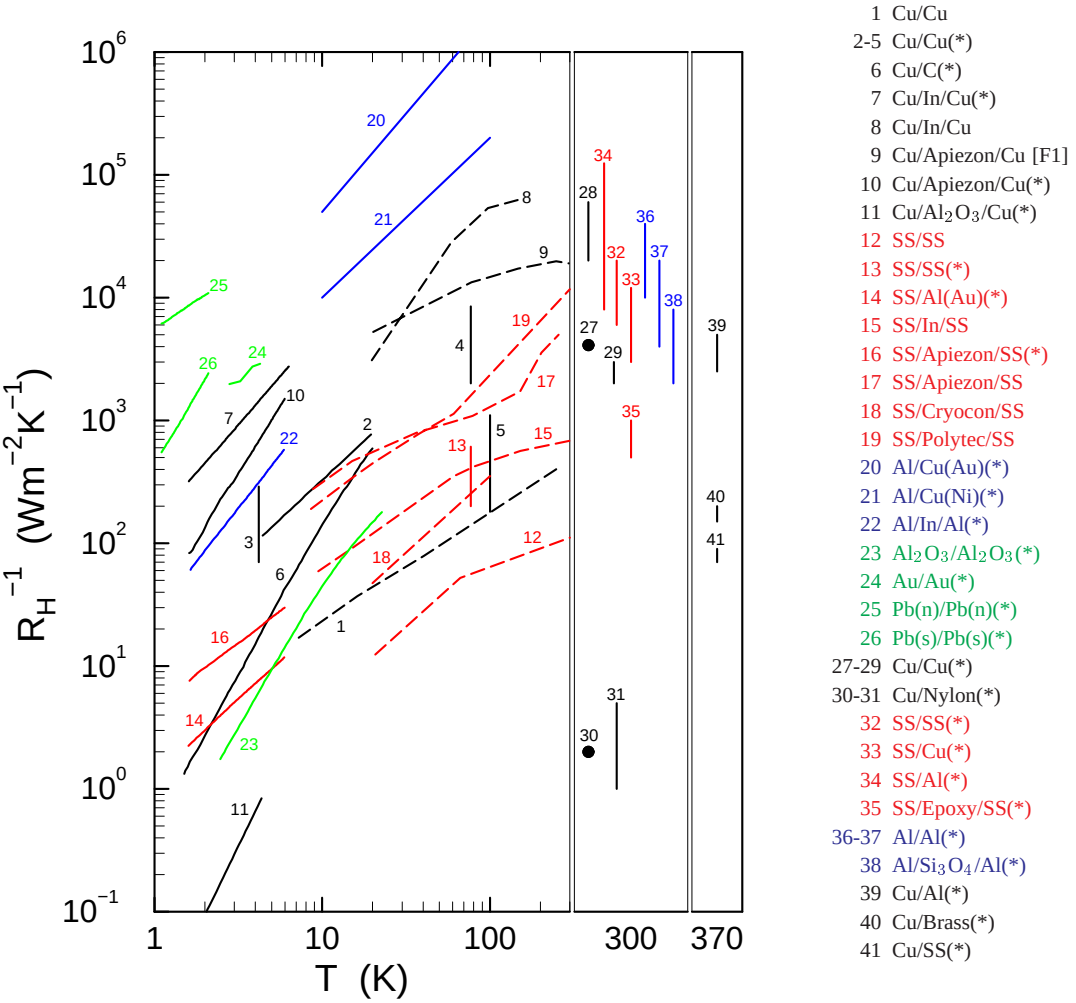

Figure 73: *Comparison of the heat conductance as a function of temperature between some contact combinations shown in Fig. 72 (dashed lines) and selected data taken from the literature, marked with (*), (s: superconducting, n: normal conducting).*

Figure 72 displays only a part of our results but indicates the essential trends:

- Dry contacts of stainless steel (12) or copper (1) show the lowest heat conductance, being 10 W/m^{2}K near 20 K and 100 W/m^{2}K at room temperature for SS, whereby Cu contacts show heat conductance values which are roughly a factor of 5 better than SS contacts.

- Increasing the force pressurized on the contact (from 20–50 N to several hundred N), the heat conductance is enhanced by a factor of 10 or more.
- Application of interposers equally improves the contact thermal conductance by one to two orders of magnitude. In particular, Apiezon-N grease and In-foil have proven *as best interface layers* for Cu and SS; other interposers, e.g. GE7031 varnish, Cryocon-grease, Polytec silver-paint and InGa also favorably influence the contact performance but the enhancement is less than for In or Apiezon-N.

In Fig. 73, a comparison is made between selected data taken from the literature and values of this studies. Our data for Cu/Cu and SS/SS contacts, dry or with different interposers fits very well into the diagram built up by the high (300 K) and low ($<$4 K) temperature data taken from the literature. The present results, together with those from the literature, yield the following general rules:

- The thermal conductance for Cu and SS contacts increases approximately linear from 10 K to 200 K and then tends to a constant value.
- The contact-resistance decreases linearly with loading pressure up to a force of nearly 1000 N.
- The thermal contact-resistance is generally not influenced by the surface roughness.
- The resistance is reduced by 1–2 orders of magnitude by applying appropriate interface layers, in particular Apiezon-N and In-foil, or GE7031 varnish, Cryocon-grease, silver-paint, InGa, etc. .

The importance of a careful selection of the type of mechanically made contacts is again emphasized in view of Fig. 72. The heat conductance between dry SS contacts and pressurized In-interlayered Cu contacts amounts to a factor of 300 over the entire temperature range. In conclusion, our numerous new data together with those taken from the literature provide an useful collection of experimental values and conditions which enable to estimate the thermal conductance of various types of contacts (including interposers) also in the intermediate temperature range from 10 K to room temperature. This wide temperature range was scarcely investigated before.

(E. Gmelin, M. Reuther and M. Asen-Palmer; R. Villar (Universidad Autonoma de Madrid))